Strong light-matter interaction in confined geometries

Dissertation

Zur Erlangung des Grades
Doktor der Naturwissenschaften (Dr. rer. nat.)
am Fachbereich Physik, Mathematik und Informatik
der Johannes Gutenberg-Universität Mainz

von:
Mohammad Noaman
geboren in Gaya, India
Mainz, 2020

JOHANNES GUTENBERG
UNIVERSITÄT MAINZ

Declaration

I confirm that no part of the material presented here has previously been submitted by myself for a degree in this or any other university. The work of others has been duly indicated, wherever applicable.

Mainz
25-04-2020

Mohammad Noaman
QUANTUM
Institut für Physik
Staudingerweg 7
Johannes Gutenberg-Universität D-55099 Mainz
monoaman@uni-mainz.de

Abstract

With the advent of technologies, such as ultra-stable laser systems, high-speed electronics, etc. a vast range of applications of quantum technology has been explored with a list of promising outcomes. For instance, to understand the properties of a many-body system, a quantum simulator has become an ideal candidate [13]. Such systems, otherwise, are highly complex to solve with the current computational power. Internet security is one of the key challenges in the present time as the existing communication channel is prone to eavesdropping. The laws of quantum physics suggest a mechanism where an entangled photons-pair, for example, can be an ideal candidate for a secure information exchange [23]. The probabilistic nature of wavefunction collapse makes these photons impossible to clone which lies in the hearts of quantum cryptography [100, 10]. The use of the wave nature of the atoms surpasses the limitations of the optical intereferometry measurements as the associated wavelength can be prepared to extremely small lengthscales [73]. Additionally, atoms prepared in a Rydberg state serve strong sensitivity towards external fields [77]. These quantum sensing aspects open up a whole new dimension to metrology [58].
To make use of a quantum system, atoms can be prepared to represent a pure quantum state which is the basis of quantum bits or qubits [82]. Photons, when tuned properly, can address a pair of such quantum states hence they serve as a mediator for exchange of quantum information in a configuration known as flying qubits. Thus, strong atom-light interaction at single photonic level becomes an important requirement. In this thesis, an atom-optics approach is made towards creating a strongly interacting quantum system. To start with, ^{87}Rb atoms are cooled down using laser cooling techniques [76, 72, 18, 71] which provides an easy manipulation of the atomic states. To enhance the light-atom interaction strength, the ongoing probe beam is spatially overlapped with the atomic ensemble. In a free space setting, such overlap is limited to the Rayleigh range [54] of the probe beam as well as the trapping potential which relies on the far red-detuned laser beam. To overcome these limitations, in this project a hollow-core fiber is used which serves the purpose of first, keeping the trapping laser beam confined and second, simultaneous overlap of the probe beam throughout the length of the atomic ensemble. This project demonstrates an optical lattice configuration, by overlapping two trapping laser beams, to trap and a controllable guiding of cold atoms. This geometrical confinement ensures the extended overlap of the probe light with the atoms which increases the interaction probability. As a figure of merit, an optical depth of 200 has been detected which is two orders of magnitude higher than for the same number of atoms in free space configuration. Further manipulation of the probe photons can be achieved in a three level atomic configuration using a process known as electromagnetically induced transparency (EIT) [29].

For several interesting applications in the quantum domain, strong nonlinearity at single photonic level becomes a key necessity which requires strong photon-photon interactions [51, 43]. With the EIT process, the photonic states can be mapped on to the atomic states [27, 9, 90, 62, 36]. Thus, a strong photonic interaction can be mediated via atomic interaction. To reach exactly this goal the EIT configuration is involved with Rydberg states – atoms excited to states with large principal quantum number. Among a range of attractive features, the atom-atom interaction scales with n^{11}, where n is the principal quantum number of the atomic state [33].
Rydberg excitation near dielectric surfaces has been a challenging task [57] due to the presence of stray electric fields. This work has demonstrated, for the first time, Rydberg EIT with cold atoms inside a hollow core fiber [60]. Furthermore, such fibers filled with Rb atoms at room temperature show significantly lower electric fields. This possibly is due to the homogeneous charge distribution which results in cancellation of the field in the core of the fiber. These results open a novel approach to perform quantum optics experiments with neutral atoms. The fiber-atom interface presented in this project further requires a detailed understanding of the propagation of the probe beam through the extended cloud. Here, the atomic ensemble can not only impose attenuation due to the absorption but the dispersive effects can modify the actual beam path through the extended atomic cloud. The transmission lineshape gets altered due to the combined dispersion and absorption of the propagating light. To understand the mechanism, a microlensing model is presented which describes the lineshapes for both, the simple two level system and the EIT configuration [69].

Zusamenfassung

Mit dem Aufkommen von Technologien wie ultrastabilen Lasersystemen, Hochgeschwindigkeitselektronik usw. wurde eine Vielzahl von Anwendungen der Quantentechnologie mit eine Reihe vielversprechender Ergebnisse untersucht. Um die Eigenschaften eines komplexen Vielteilchensystems zu verstehen, ist ein Quantensimulator ein idealer Kandidat [13] geworden, dessen Lösung mit der gegenwärtigen Rechenleistung ansonsten sehr komplex ist. Die Internetsicherheit ist in der heutigen Zeit eine der wichtigsten Herausforderungen, da der vorhandene Kommunikationskanal anfällig ist abgehört zu werden. Die Gesetze der Quantenphysik legen einen Mechanismus nahe, bei dem beispielsweise ein verschränktes Photonenpaar ein idealer Kandidat für einen sicheren Informationsaustausch [23] sein kann. Die probabilistische Natur des Kollapses der Wellenfunktion macht es unmöglich, diese Photonen zu klonen, die damit das Kernelement der Quantenkryptographie bilden [100, 10]. Die Verwendung der Wellennatur der Atome übersteigt die Grenzen der optischen Interferometrie, da die zugehörige Wellenlänge auf extrem kleine Längenskalen [73] eingestellt werden kann. Darüber hinaus weisen Atome in einem Rydberg-Zustand eine starke Empfindlichkeit gegenüber äußeren Feldern [77] auf. Diese Aspekte des Quantensensors eröffnen der Metrologie eine völlig neue Dimension [58]. Um ein Quantensystem zu nutzen, können Atome so präpariert werden, dass sie einen reinen Quantenzustand repräsentieren, der die Grundlage für Quantenbits oder Qubits bildet [82]. Photonen können, wenn sie richtig eingestellt sind, ein Paar solcher Quantenzustände adressieren. Daher dienen sie als Vermittler für den Austausch von Quanteninformationen in einer Konfiguration, die als fliegende Qubits bekannt ist. Damit wird eine starke Atom-Licht-Wechselwirkung auf der Ebene einzelner Photonen zu einer wichtigen Anforderung. In dieser Arbeit wird ein atomoptischer Ansatz zur Erzeugung eines stark wechselwirkenden Quantensystems entwickelt. Zunächst werden ^{87}Rb-Atome mithilfe von Techniken der Laserkühlung abgekühlt [76, 72, 18, 71], die eine einfache Manipulation der Atomzustände ermöglichen. Um die Wechselwirkungsstärke zwischen Licht und Atom zu erhöhen, wird der Probenstrahl räumlich mit dem Atomensemble überlappt. In einer Freistrahl-Konfiguration ist eine solche Überlappung auf den Rayleigh-Bereich des Probenstrahls sowie auf das Einfangpotential beschränkt, das auf dem weit rot verstimmten Laserstrahl beruht [54]. Um diese Einschränkungen zu überwinden wird in diesem Projekt eine Hohlkernfaser verwendet, die zum einen dazu dient, den einfangenden Laserstrahl zusammen zu halten und zum anderen gleichzeitig den Probenstrahl über die gesamte Länge des Atomensembles zu überlappen. Dieses Projekt demonstriert eine optische Gitterkonfiguration durch Überlagerung zweier einfangender Laserstrahlen, um kalte Atome einzufangen und kontrolliert zu führen.

Diese geometrische Begrenzung stellt die ausgedehnte Überlappung des Sondenlichts mit den Atomen sicher, und erhöht damit die Wechselwirkungswahrscheinlichkeit. Als Gütefaktor wurde eine optische Tiefe von 200 gemessen, die bei gleicher Anzahl von Atomen in Freistrahl-Konfiguration zwei Größenordnungen höher ist. Eine weitere Manipulation der Sondenphotonen kann in einer Atomkonfiguration mit drei Niveaus unter Verwendung eines Prozesses erreicht werden, der als elektromagnetisch induzierte Transparenz (EIT) [29] bekannt ist. Für einige interessante Anwendungen im Quantenbereich wird eine starke Nichtlinearität auf der Ebene einzelner Photonen zu einer Schlüsselbedingung, die starke Photon-Photon-Wechselwirkungen erfordert [51, 43]. Mit dem EIT-Verfahren können die photonischen Zustände auf die Atomzustände [27, 9, 90, 62, 36] abgebildet werden. Somit kann eine starke photonische Wechselwirkung über atomare Wechselwirkung vermittelt werden. Um genau dieses Ziel zu erreichen, wird die EIT-Konfiguration mit Rydberg-Zuständen verbunden – Atomen, die zu Zuständen mit großer Hauptquantenzahl angeregt werden. Als eine von vielen interessanten Eigenschaften skaliert die Atom-Atom-Wechselwirkung mit n^{11}, wobei n die Hauptquantenzahl des Atomzustands [33] ist.
Die Rydberg-Anregung in der Nähe von dielektrischen Oberflächen war aufgrund von elektrischen Streufeldern [57] eine herausfordernde Aufgabe. Diese Arbeit hat zum ersten Mal Rydberg-EIT mit kalten Atomen in einer Hohlkernfaser demonstriert [60]. Darüber hinaus zeigen solche mit Rb-Atomen gefüllten Fasern bei Raumtemperatur signifikant geringere elektrische Felder. Dies ist möglicherweise auf die homogene Ladungsverteilung zurückzuführen, die zur Aufhebung des Feldes im Kern der Faser führt. Diese Ergebnisse eröffnen einen neuen Ansatz für die Durchführung quantenoptischer Experimente mit neutralen Atomen. Die in diesem Projekt vorgestellte Faser-Atom-Schnittstelle erfordert ferner ein detailliertes Verständnis der Ausbreitung des Probenstrahls durch die erweiterte Atomwolke. Hier kann das Atomensemble nicht nur zu Dämpfung durch Absorption führen, sondern die dispersiven Effekte können auch den tatsächlichen Strahlengang durch die ausgedehnte Atomwolke modifizieren. Die transmittierte Spektrallinie ändert sich aufgrund der kombinierten Streuung und Absorption des sich ausbreitenden Lichts. Um den Mechanismus zu verstehen wird ein Mikrolinsenmodell vorgestellt, das die Linienformen sowohl für ein einfaches Zwei-Niveau-System als auch für die EIT-Konfiguration [69] beschreibt.

Contents

1. Introduction

Physical processes governed by classical mechanics have been reasonably successful in describing the dynamics of macroscopic systems. However, the same laws do not qualify, in general e.g. at smaller length scales, such as those of atoms or molecules. A fundamentally distinct approach is made to understand the nature of physics where, for example, an atom is conceived to have both, a wave and a particle nature. In this interpretation, furthermore, the nature of light carries particle properties together with the commonly accepted electromagnetic wave characteristics. Such counter-intuitive wave-particle duality provides a better model of light-atom interactions which lies in the roots of a separate division of physics known as atomic, molecular and optical physics (AMOP). Beyond providing a deeper understanding of the laws of nature, the results of AMOP have shown promising boost in both fundamental research as well as technological advancements. However, due to the fragile nature of a quantum system, the practical implementation also comes with a natural cost of precision control and measurement.

With the advancement in the experimental techniques, the gap between the theoretical model and the experimental realization is consistently narrowing down. To this end, one of the most remarkable breakthroughs achieved is the preparation of Bose-Einstein condensate (BEC) [3, 19] which has not only confirmed the theoretical understanding but also opened a plethora of scientific research along with precision applications. As a quantum simulator, many-body systems [13, 17, 32, 81, 87, 86, 56, 88] have been studied in a wide range of parameter space which otherwise poses extreme experimental requirements. Interesting phase transitions have been explored such as superfluid to Mott insulator [39] and Fermionization of bosons in a Tonks-Girardeu system [42]. Atom interferomentry [50] has opened up as a new branch of metrology which utilizes the benefits from the short wavelength associated with the ultra-cold atoms. The high precision is promising for measurements of the local gravitational fields to explore the Einstein's relativity principle [22, 99]. Furthermore, the experiments with cold-atoms lie in the heart of extremely accurate atomic clocks [66]. The claimed relative uncertainty below 1×10^{-18} has a promising application for measurement of geodesy below the centimeter level. Another remarkable progress is ongoing for ultra-secure communication using the features of quantum behaviour. The concept of no-cloning of a quantum state allows for a communication channel which is insensitive to eavesdropping [100]. Quantum computation is a highly spoken topic today as it promises a powerful computation which can surpass the existing classical systems in certain ways [41, 84]. With a handful of promising applications, however, the practical implementation comes with a precious cost of highly controlled experimental demands. The stringent needs are imposed due to the high sensitivity of a quantum system towards

the interaction with the environment which induces decoherence – a process known for projecting a quantum system into a classical one. This results in a suppressed contrast and short interrogation time for a given measurement.
The long term perspective of the work performed for this thesis is developing an experimental platform for utilizing the strengths of quantum mechanics for high precision sensing, quantum information and processing. To achieve this goal, the approach is taken using an atom-optics realization. In that the quantum information stored in the form of atomic states or quantum bits also popularly called as qbits can be manipulated via photonic interactions. In particular, the Rb atoms are prepared in a special geometrical setting to enhance light-matter coupling. The exchange of photonic information is mediated via the atomic ensemble and thus establishing a novel light-matter interface. For the experiment in the laboratory, laser cooled ^{87}Rb atoms are chosen for this project. The atoms trapped in an ultra-high vacuum (UHV) chamber retain all the properties of an individual atom as the density is too low to have any significant influence between a pair of atoms. This allows for manipulation of multiple atoms simultaneously neglecting the inter-particle interactions. At this stage, the weak nature of atom-photon interaction can partly be compensated by preparing a large number of atoms which eventually results in a better signal to noise ratio (SNR). Parallel to that, several approaches are made to enhance atom-photon coupling on individual levels such as atoms trapped in a cavity where coupling strength is enhanced by a factor associated with the finesse of the cavity [49, 44]. Here, a single photon traverses multiple times across the atom which effectively increases the chance of interaction with the atom. In another approach, surface plasmonic coupling is utilized where an atom is coupled to an enhanced near field. The evanescent field is enhanced at a region of interest which eventually enhances the coupling strength with the atoms in a matching dipole radiation pattern.
In this project, an alternative approach is taken where a cold atomic medium is trapped in an extended confinement. Following the Beer-Lambert law, as a figure of merit optical depth, (OD) scales with the length of such atomic medium. This way by using geometrical control the extension length of the cloud can be manipulated and consequently the coupling strength. However, the preparation of such an elongated atomic sample along with the interacting light field itself is challenging. In typical experiments atoms are trapped in a focused far red detuned (also blue detuned) laser beam [40]. Tight confinements become a natural need in order to obtain high OD. In free-space this is achieved by focusing the beam very tightly using lenses of high numerical aperture. As it is understood from Gaussian optics, a tightly focused beam suffers from extreme divergence. This results in a very shallow region where the atoms are trapped leaving a short interaction zone. To keep the beam confined and yet capable of accommodating cold atoms, a hollow-core (HC) fiber is introduced where a light field can be kept confined throughout the length of the fiber. Utilizing this property and making use of dipole trapping, atoms can simultaneously be held in such a confinement. In the recent times, an accelerating research interest can be observed in this field for its promising strengths. Such confinement allows for an extended overlap of a weak laser beam with the atoms which has shown enhancement in light matter

coupling as characterized by the optical depth. In such fiber based systems an OD of 1000 has been observed [12]. Strong nonlinearities have been demonstrated for low light levels in such fiber based [103] systems opening up a relatively new research window. A compact and ultra-precise frequency referencing using atoms or molecules filled inside an HC fiber [85, 93] aims to develop a robust solution. These HC fibers filled with cold atoms have been demonstrated for the atom-interferometry experiments [102]. Yet another advancement of such atom-fiber interface is demonstrated in where atoms are confined in the Lamb-Dicke regime which have shown phenomenal results in the scope of studying atom-atom interactions [70].

Now, to induce photon-photon interaction, non-linear processes become natural choice. In that, the usual addition of two electric field components does hold true, instead, higher order terms, in particular, product of two fields can be observed. This, in turn can lead to interesting results such as sum or difference of two frequencies in the optical spectrum [30]. Moreover, these non-linear processes can be utilized to generate non-classical photon states [38, 52] which will have its applications in quantum information processing other than performing many-body system with photons. In typical optical materials, such non-linear processes are visible only at higher laser intensities due to weak higher order terms. Whereas, for quantum computation and information processing where such non-linearity is required at very low photon number, typically at single photon level [51]. To enhance the effects, among the various other competitive approaches, the features of atoms excited to very high principle quantum number states have been explored with promising results. These atoms fall in a class known as Rydberg atoms [33] in the honor of Johannes Rydberg. An illustration is shown in Figure 1.1. In such atoms, the outer shell electron is weakly bound to the nucleus, as a result these atoms are very sensitive towards external fields making them an ideal tool for sensor. A number of experimental achievements are made utilizing the features such as high sensitivity [31] towards electric fields. Furthermore, the weak overlap of the dipole transition from the Rydberg states to the ground states results in inhibited transitions which in effect extends the lifetime of the atoms once prepared in Rydberg state [34]. This long lifetime allows for treatment of the system in an alternate "ground" state and has benefits in experiments, for instance, long coherence time scale. Another interesting regime is explored by the enhanced atom-atom interaction [5]. Due to the presence of one excited atom in a volume of certain radius, all the remaining atoms encounter an energy shift hence no further excitations are possible. This phenomenon is known as Rydberg blockade [62]. Saturation at single photon levels have been demonstrated [92] in order to create extreme nonlinearity. Moreover, each of the atoms within the blockade volume has certain interaction probability with the ongoing light field. As an aggregate, the ensemble can be treated as an effective two level system with much higher interaction strength. Such giant form of ensemble of atoms is called superatom. The Rydberg blockade effects can further be utilized for exchange of photonic information mediated via atomic ensemble as the spatial correlations are mapped onto the photons [91]. The tuneable and long-range interaction have added features which have been utilized in creating many-body photonic states where photons are made to interact with each other in the same way as

present in solid state crystals [37].

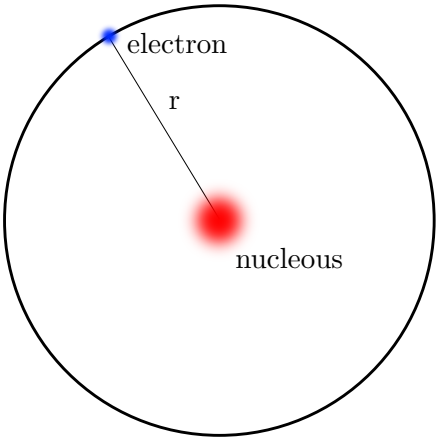

Figure 1.1.: A classical picture of a Rydberg atom. High electronic excitation can be visualized as an outer shell electron residing far away from the positively charged core.

This project aims to combine the two research topics discussed in the previous paragraphs to create a novel system where the benefits of the two individuals are multiplied. For example, one idea is to use the extended cloud to create a chain of Rydberg atoms forming an arrangement of interacting photons. Generation of non-classical photons in this setting can have its advantage due to the extended length as depicted in the Figure 1.2. Here, a coherent light pulse enters into the fiber filled with atoms. By controlled excitation, such as via electro-magnetically induced transparency (EIT), the photonic states can be mixed with the atomic states in a generalized system known as polariton. By choosing appropriate Rydberg states, the contribution arising from the atomic interactions can lead to the transfer of the photonic information. The tuneable nature of the atomic interaction provides a knob to manipulate the photon-photon interaction. As the fiber being quasi-one dimensional system, interesting states of photons such as observation of Luttinger liquids [63], Tonks-Girardeu [65] regimes would be of great importance.
With the promising long term goals, the thesis describes the experimental achievements that are prerequisite to establishing strong tuneable photon-atom and consequently photon-photon interactions as depicted in Figure 1.3. To this end, cold atoms of ^{87}Rb are prepared inside a UHV. These atoms are then transferred to an optical dipole trap which passes through the HC fiber place inside the UHV chamber. This way the atoms are trapped and guided into the fiber. However, in this technique the longitudinal position control over the atoms is limited. To gain more control, another optical dipole trap beam from the counter direction is overlapped into the HC fiber. This way the light fields realize an optical lattice configuration which can be set into motion by altering the relative detuning between the two dipole lasers. The next step is to establish a detection scheme through the fiber as the atoms inside the fiber lose

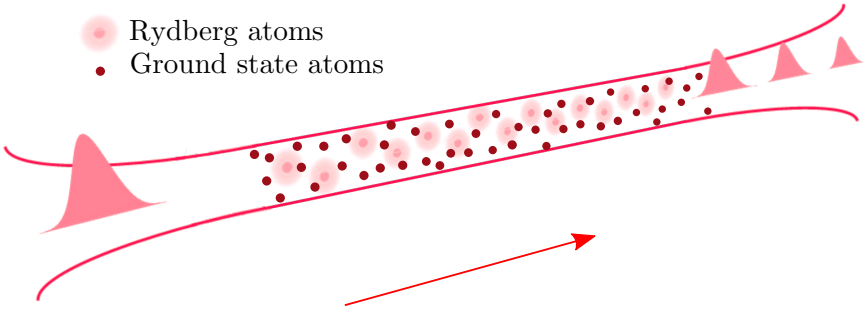

Figure 1.2.: Information stored in the form of atomic states and manipulated with photons. The confinement enhances the interaction probability and provides a quasi-one dimensional configuration.

its optical access from other directions. A weak laser beam tuned to the D2 transition line of the ^{87}Rb is overlapped along with the dipole beams. This naturally confirms the overlap of the atoms with the probe beam. Although this scheme is seemingly simple, the detection requires special attention as the beam encounters a cloud with radially varying density which results in lensing like effects. This work explores the light propagation through the atomic cloud. Consequently, the spectral features are studied which show significant importance in the underlying physical processes for such quasi-one dimensional geometries. Furthermore, the detection of the Rydberg EIT signals inside the fibers brings the project a step further towards the main goal. In particular, this step had been debated due to the presence of a silica surface nearby which are known for introducing stray electric fields. A variety of fibers with different inner coating are tested which have produced satisfactory results. Now, understanding the spectral lineshapes of the Rydberg EIT, the similar lensing model was introduced since the added control beam further manipulates the optical response through the two photon process. These studies are of significant importance since the various types of lineshapes are observed for the different interaction space.

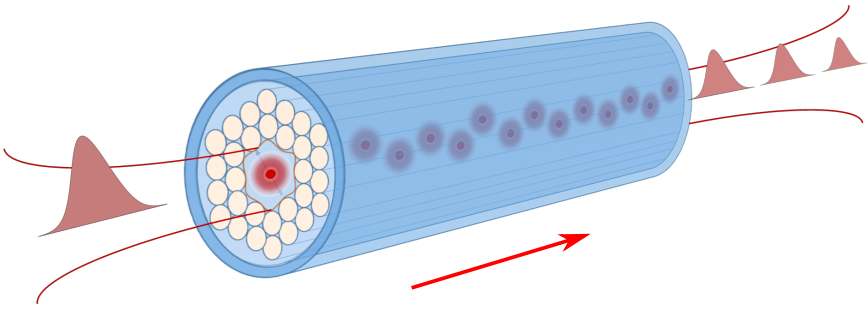

Figure 1.3.: Experimental realization using an HC fiber where both, light and matter stay overlapped and confined.

The Chapter 2 of this thesis overviews a three level system with the main emphasis

on EIT involving Rydberg states. In particular, the EIT features for cold and room temperature atoms are presented in details. The confinement and the guiding of light and atoms are presented in Chapter 3. The main parts are the experimental setup that consists of HC fiber inside the UHV chamber, the optical conveyor belt installed through the fiber that is used for the transport of the atoms and the detection scheme. This chapter further discusses one of the major experimental challenges is to overlap multi-colour laser beams which is the main prerequisite for this project. In Chapter 4, the details of the experimental control system is introduced where an FPGA based solution is implemented and integrated with the existing experimental control. For the measurements, a user-friendly, generation of high speed and precise pulse patterns become a must in order to record the dynamics at faster time scales. Furthermore, the pulses need to be stored with accurate timings in order to explore the zone of interest. Chapter 5 discusses the experimental results and the analysis of the Rydberg excitation with the cold atoms inside the hollow core fiber [60]. These results are the first signals with the cold atoms inside an HC fiber. In a distinct setup a variety of fibers with coating and core structures are installed for characterization of the fiber-atom interactions. Here the Rydberg EIT signals are studied to explore a suitable fiber for the main experiment. The limitations and the features of the experiments with the hollow core fibers are discussed in details. In Chapter 6 a detailed study of a beam propagation model inside a quasi-one dimensional cloud is made. The model is essential to understand the measurements which provides a range of valuable information about the light-matter interaction in a confined geometry. Moreover, it also explains the lineshape distortions [69] appearing in the measurement results which could otherwise occur for a variety of reasons.

2. Three level system – Rydberg EIT

In AMOP, atoms can conveniently be prepared to represent a quantum system such as cold atoms trapped in a potential created by various types of fields [25]. To address the atomic states, and furthermore, to transport the associated quantum information, photons come as a natural choice [51]. Thus, controlled manipulation of light becomes one of the key requirements in the fields of quantum optics. A potential candidate to achieve this goal is by coupling the light field to an atomic transition [64]. For near-resonant condition, the interaction cross-section is found to have a dramatic increment [46]. Such light-atom setting has been useful for a variety of applications such as quantum information processing, quantum sensing, precision measurements, etc [74, 26, 29].

An atom generally possesses many quantum states labeled by their quantum numbers which are obtained from the solutions of the Schrödinger equation associated with the atom. For convenience, a two level system consists of a pair of quantum states with allowed dipole transition which can be addressed by an electromagnetic field such as a laser beam, or a radio frequency (RF) source. For quantum optics applications a preferred pair of states is chosen with a large dipole transition matrix element which is a measure of the coupling strength of the field with the atom. One of the key features of such atom-optics system is that the properties of an atom always remain the same irrespective of space and time hence the transition frequency is universally constant as long as the physical conditions such as electric or magnetic fields are kept the same. In addition, certain transitions in some atoms exhibit extremely narrow linewidth [53, 24] which is utilized for an ultra-stable frequency reference. These features lie in the heart of an atomic clock where an oscillating signal is referenced and stabilized to the narrow atomic transition [66]. A two level system with long coherence time – a time scale over which the dynamics is governed by the quantum physics – serves as an ideal candidate for quantum information processing. In this regard, although a handful of applications are explored with just a simple two level system, control at single to few photons level still is a challenging task. This is mainly because the light-atom interaction strength is insignificant at individual photon level. Keeping the simplicity of the system, to better control the photons interacting with the two level system, an additional laser field is introduced that couples to a third state. This way a three level atomic system is realized which interacts with two light fields which shows a significantly modified response. Allowed by the transition rules, general schemes for such three level system with two coupled light fields are shown in the Figure 2.1. Here, three atomic states are indicated by the *ket* notation $|1\rangle$, $|2\rangle$ and $|3\rangle$. The two light fields with the associated Rabi frequencies are indicated by Ω_p and Ω_c. The three configurations recognized as Λ type, Ladder type and V

type conventionally have state $|2\rangle$ as commonly addressed by the two laser fields. To simplify the processes, in a case where $\Omega_c = 0$, the system reduces to a two level type, where the remaining laser field labeled as probe beam is only coupled to $|1\rangle \leftrightarrow |2\rangle$ transition. In a case where the probe field intensity is far below the saturation intensity of the transition, strong absorption is observed as the laser frequency matches with the atomic transition line. Now, by increasing the value of Ω_c, i.e. increasing the associated laser field intensity, the spectral features are dramatically modified. Hence the light field associated with $|2\rangle \leftrightarrow |3\rangle$ transition is called a control beam. Such type of control preserves a completely coherent feature and hence it has been used a tool for manipulation of light. In an adiabatic process, the ongoing probe photons can be mixed with the atomic states and the general term is called as polariton [28]. In this framework, probe photons can not only be stored in the atomic ensemble but they can be retrieved in a controllable manner. Thus, this technique can be utilized to exchange the quantum information between the photons and the atoms. While the 3-level system helps in creating and controlling light-atom coupling, the interaction between two photons is still limited. However, the mapping of photonic states onto to the atomic states as explained by the polariton picture, the problem now translates to creating strong atom-atom interaction.

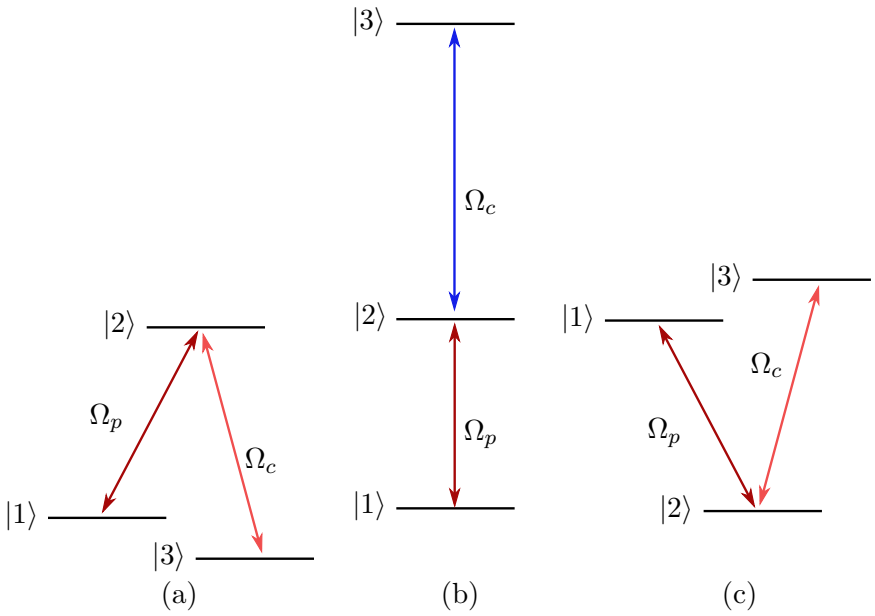

Figure 2.1.: Three-level schemes – (a) Λ type, (b) Ladder type and (c) V type.

Typically, an atomic ensemble prepared in experiments with quantum systems is kept isolated to reduce the environmental influences. Techniques such as laser cooling and trapping have provided a way to confine the ensemble in an isolated space. There the density of the atoms is significantly small as compared to that found at atmospheric pressure and temperature. System prepared at such low temperatures and density assures that the atom-atom interactions do not destroy the precise transition

features of an individual atom. Such configurations are favoured for maintaining a long coherence time which is extremely important for storing quantum information in the form of atomic states. A key requirement for a distributed quantum information processing is an efficient exchange of the stored quantum information. In this case, to achieve the goal strong interaction between the photons is desired. As hinted earlier, one way to create such interaction is by enhancing the atom-atom interaction which is highly insignificant for the given inter-atomic distances. This is generally true for atoms lying in low principal quantum number, n, however when excited to a large n, the influence of one atom to the neighbouring atoms becomes significantly large. These highly excited atoms, also known as Rydberg atoms, posses very long-range interaction, where atoms influence each other over distances on the order of several micrometers [33].
This chapter lays out a foundation for understanding light-matter interaction in different regimes. Interesting results are explored where the two lasers address three states as in the three-level system. While a general solution is rather complicated, certain special cases have shown promising results in the applications of manipulating light for quantum information and sensing aspects. In the early sections, such three level system is explored with different configurations. Furthermore, a section is dedicated to explore the features of Rydberg atoms and with the combined understanding of the Rydberg EIT. Various technical details are also presented related to the experimental limitations.

2.1. Electro-magnetically Induced Transparency (EIT)

The way to go about solving the three-level system is to obtain the interaction between the atomic ensemble and the light fields for the given configuration as shown in the Figure 2.1. In the form of total Hamiltonian it is represented as

$$H = H_a + H_i, \tag{2.1}$$

where H_a and H_i are the unperturbed atomic and the interaction Hamiltonians. As the light fields are introduced, one of the most important interests is to obtain the final atomic states. These results will provide the nature of interaction which can be utilized to manipulate the atomic states. Moreover, the propagating light fields can also be controlled based on how they couple to the atomic states.
To construct the interaction Hamiltonian, H_i a semi-classical approach is made where the light field is considered as a wave with oscillating electric field, $\mathcal{E}$. Upon the introduction to an atom, the charges separate in a manner to create an induced dipole moment which then interacts with the field itself. The associated Hamiltonian, H_i is described by

$$H_i = -\mu \cdot \mathcal{E}, \tag{2.2}$$

where μ is the induced dipole moment. This dipole approximation is commonly applied and remains valid as long as the wavelength of the interacting light field is larger than

the atomic expansion for the reason that an atom should not experience the spatial field modulation.
In the context of an atom being a quantum mechanical system, the light matter coupling strength is obtained by the associated transition dipole moment involving the transition between the two states, $|i\rangle$ and $|j\rangle$ addressed by a laser field. The transition moment elements, μ_{ij} are given by

$$\mu_{ij} = e\mathbf{r}_{ij}, \tag{2.3}$$

where $\mathbf{r}$ is the displacement operator with $\mathbf{r}_{ij} = \langle i|\mathbf{r}|j\rangle$ and e is the electronic charge. With the light field, $\mathcal{E}(t) = \mathcal{E}_0 cos(\omega t)$ a convenient way of expressing the light-matter coupling strength is

$$\hbar\Omega_{ij} = -e\mathcal{E}_0\langle i|\mathbf{r}|j\rangle, \tag{2.4}$$

where $\mathcal{E}_0$ is electric field amplitude and Ω_{ij} is Rabi frequency associated with the transition between the two states, $|i\rangle$ and $|j\rangle$.
Now with the general state expressed in the atomic level basis as

$$|\psi_i\rangle = a_i|1\rangle + b_i|2\rangle + c_i|3\rangle, \tag{2.5}$$

the goal is to obtain the three coefficients, a_i, b_i and c_i. By solving the time dependent Schrödinger equation,

$$i\hbar\frac{\partial}{\partial t}\psi = H\psi, \tag{2.6}$$

the coefficients can be obtained, however it lacks the ability to obtain results for a general case. For instance, situations where mixed states are present or decoherence processes are involved a mixed state can not be represented just by a *ket* vector, $|\psi_i\rangle$. To deal with the problem, the density matrix formalism is implemented where a general quantum system is considered as a statistical mixture of pure states,

$$\rho = \sum_i p_i|\psi_i\rangle\langle\psi_i|, \tag{2.7}$$

where p_i is the probability of the system being in a given pure state ψ_i. In other words, the matrix form of the density state appears as follows,

$$\rho = \begin{bmatrix} \rho_{11} & \rho_{12} & \rho_{13} \\ \rho_{21} & \rho_{22} & \rho_{23} \\ \rho_{31} & \rho_{32} & \rho_{33} \end{bmatrix}. \tag{2.8}$$

Here, the diagonal elements, i.e. ρ_{ii} represent the population in a given pure state, $|i\rangle$ and the off-diagonal elements represent the coherences between the two states, $|i\rangle$ and $|j\rangle$. The significance of the diagonal elements is that the non-zero value of ρ_{ij} distinguish the system from a classical one, i.e. in a classical system all the off-diagonal terms are zero.
The equivalent Schrödinger equation, known as Liouville equation is derived as

$$\frac{d}{dt}\rho = \frac{-i}{\hbar}\big[H, \rho\big], \tag{2.9}$$

where, $[\cdot]$ is the commutator operator. For the given Hamiltonian the above equation governs the dynamics of the density state. One of the biggest advantages in representing a system in the matrix formalism is that the incoherent processes such as spontaneous decay from different levels can easily be implemented into the equation as

$$\frac{d}{dt}\rho = \frac{-i}{\hbar}[H, \rho] - \mathcal{L}(\rho), \tag{2.10}$$

where, $\mathcal{L}$ is a general form of the Lindblad operator with the components responsible for the decay and the dephasing rates as shown below

$$\mathcal{L} = \frac{\Gamma}{2}\Big(\alpha^\dagger\alpha\rho + \rho\alpha^\dagger\alpha - 2\alpha\rho\alpha^\dagger, \Big). \tag{2.11}$$

Here, $\alpha = |i\rangle\langle j|$ is the atomic projection operator and Γ comprises of the decay and the dephasing terms from the different states.

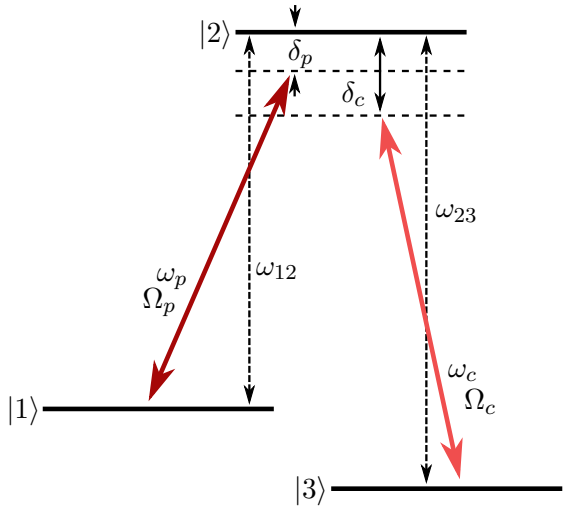

Figure 2.2.: Λ type EIT scheme.

To construct the mathematical model, for simplicity the Λ scheme is considered with the various parameters as shown in the Figure 2.2. The total Hamiltonian is obtained by the Equations 2.1 and 2.4. Normalizing the ground state, $|1\rangle$ to zero energy the unperturbed atomic Hamiltonian and the interaction Hamiltonian are given by

$$H_0 = \hbar\omega_{12}|2\rangle\langle 2| + \hbar\omega_{23}|3\rangle\langle 3|, \tag{2.12}$$

$$H_i = \frac{\hbar}{2}\Big(\Omega_{12}e^{i\omega_p t}|2\rangle\langle 1| + \Omega_{23}e^{i\omega_c t}|2\rangle\langle 3| + h.c.\Big), \tag{2.13}$$

where, ω_{ij} are the resonance frequencies for the atomic transitions $|i\rangle$ to $|j\rangle$ and $\omega_{p/c}$ are the probe/ control laser frequencies. For the given three-level configuration the

Lindblad operator is expressed as

$$\begin{aligned}\mathcal{L} =& \frac{\Gamma_{21}}{2}\left[2\alpha_{12}\rho\alpha_{21} - \alpha_{22}\rho - \rho\alpha_{22}\right] \\ &+ \frac{\Gamma_{23}}{2}\left[2\alpha_{32}\rho\alpha_{23} - \alpha_{22}\rho - \rho\alpha_{22}\right] \\ &+ \frac{\gamma_2}{2}\left[2\alpha_{22}\rho\alpha_{22} - \alpha_{22}\rho - \rho\alpha_{22}\right] \\ &+ \frac{\gamma_3}{2}\left[2\alpha_{33}\rho\alpha_{33} - \alpha_{33}\rho - \rho\alpha_{33}\right],\end{aligned} \tag{2.14}$$

where, Γ_{ij} are the spontaneous decay rates from the state $|i\rangle$ to $|j\rangle$ and γ_i are the dephasing rates for the states $|i\rangle$.

2.1.1. Optical-Bloch equations

Theoretical understanding of the evolution of a multi-level system like presented here is obtained by solving Optical-Bloch equations. The solutions of the Equation 2.10 are multi-fold – the values ρ_{ii} represent the population in the given state $|i\rangle$ and the coherences between two levels are obtained by the ρ_{ij}. The physical significance of the off-diagonal terms is to obtain the influence of the atomic ensemble on the light field in the form of absorption/ dispersion as will be discussed in the later sections. These parameters are some of the crucial physical components which are measured experimentally in a lab. In particular, the main interest lies here on the estimation of ρ_{12} as this quantity influences the probe light which is detected on a sensor in the from of absorption and phase shift. To obtain the results from the Equation 2.10 the density matrix elements need to be transformed conveniently as

$$\begin{aligned}\sigma_{ii} &= \rho_{ii}, & \forall i = 1,2,3 \\ \sigma_{12} &= \rho_{12}e^{-i\omega_p t}, & \sigma_{21} = \sigma_{12}^*, \\ \sigma_{13} &= \rho_{13}e^{-i(\omega_p-\omega_c)t}, & \sigma_{31} = \sigma_{13}^*, \\ \sigma_{23} &= \rho_{23}e^{-i\omega_c t}, & \sigma_{23} = \sigma_{23}^*,\end{aligned} \tag{2.15}$$

where, the asterisk (*) denotes the complex conjugate with the normalization condition attained by $\sum_i \sigma_{ii} = 1$. In the transformed basis with the consideration of rotating wave approximation the total Hamiltonian simplifies to

$$H = -\frac{\hbar}{2}\begin{bmatrix} 0 & \Omega_p & 0 \\ \Omega_p & -2\delta_p & \Omega_c \\ 0 & \Omega_c & -2(\delta_p - \delta_c) \end{bmatrix}. \tag{2.16}$$

The Lindblad master equation 2.10 is solved with the transformed matrix elements to

obtain the dynamics in the form of differential equations.

$$\dot{\sigma}_{21} = -(\gamma_{21} - i\delta_p)\sigma_{21} + \frac{i\Omega_c}{2}(\sigma_{22} - \sigma_{11}) + \frac{i\Omega_p}{2}\sigma_{31}, \tag{2.17}$$

$$\dot{\sigma}_{31} = -(\gamma_{31} - i(\delta_p + \delta_c))\sigma_{31} + \frac{i\Omega_c}{2}\sigma_{21} + \frac{i\Omega_p}{2}\sigma_{32}, \tag{2.18}$$

$$\dot{\sigma}_{32} = -(\gamma_{32} - i\delta_c)\sigma_{32} + \frac{i\Omega_c}{2}(\sigma_{33} - \sigma_{22}) - \frac{i\Omega_p}{2}\sigma_{31},, \tag{2.19}$$

$$\dot{\sigma}_{22} = \Gamma_{21}(1 - \sigma_{22} - \sigma_{33}) + \frac{i}{2}(\Omega_p\sigma_{12} - c.c.),, \tag{2.20}$$

$$\dot{\sigma}_{33} = \Gamma_{23}(1 - \sigma_{22} - \sigma_{33}) + \frac{i}{2}(\Omega_c\sigma_{32} - c.c.),, \tag{2.21}$$

where, the probe detuning, $\delta_p = \omega_p - \omega_{12}$, the control detuning, $\delta_c = \omega_c - \omega_{23}$, and the coherent decay rates defined as, $\gamma_{21} = \Gamma_{21} + \Gamma_{23} + \gamma_2$, $\gamma_{23} = \Gamma_{21} + \Gamma_{23} + \gamma_3$ and $\gamma_{31} = \gamma_3$. As discussed earlier, the main focus here is to obtain the expression for σ_{21} as it is responsible for the propagation of the probe beam through the atomic medium. One of the interesting regimes is to explore the steady state solution where the coherences reach an equilibrium situation, i.e. $\dot{\sigma}_{ij} = 0, \forall i, j$. In the case of weak probe beam, i.e. $\Omega_{12} << \Omega_{23}$ the Equation 2.18 reduces to

$$\sigma_{31} = -\frac{i\Omega_c}{2(\gamma_{31} - i(\delta_p + \delta_c))}\sigma_{21} + \frac{i\Omega_p}{2(\gamma_{31} - i(\delta_p - \delta_c))}\sigma_{32}. \tag{2.22}$$

Starting with the initial population prepared in the state $|1\rangle$, for a weak probe beam, the populations in the states $|2\rangle$ and $|3\rangle$ will be a significantly small fraction of the total population. Therefore the value of the coherence, σ_{23} is negligible as compared to σ_{12}. Combining these assumptions, the contribution from the second term in the Equation 2.22 is approximated to zero.
Utilizing the Equation 2.17, the expression for σ_{21} is written as

$$\sigma_{21} = \frac{\Omega_p/2}{\gamma_{21} - i\delta_p + \frac{\Omega_c^2}{4(\gamma_{31} - i(\delta_c - \delta_p))}} \tag{2.23}$$

The optical response is obtained by comparing the analogous macroscopic optical property of a material. From the electrodynamics the optical response of a dielectric material can be expressed as

$$\mathcal{P} = \epsilon_0\chi(\omega_p)\mathcal{E}, \tag{2.24}$$

$$= \epsilon_0\mathcal{E}_0\big[\chi(\omega_p)e^{i\omega_p t} + \chi(\omega_p)e^{-i\omega_p t}\big], \tag{2.25}$$

where, $\mathcal{P}$ is the polarization vector and χ is the susceptibility which is defined as $\chi = \frac{\epsilon}{\epsilon_0} - 1$. Whereas, for an atomic ensemble with the density, N the polarization is expressed as

$$\mathcal{P} = N\langle\mu\rangle, \tag{2.26}$$

where, $\langle\cdot\rangle$ is mean value of the dipole operator, μ. In the matrix formalism, the expectation value of an observable is obtained by taking trace of the product of density operator, ρ with the observable. In this case

$$\langle\mu\rangle = Tr(\rho\mu), \tag{2.27}$$

where Tr is trace of the matrix. This simplifies the Equation 2.26 to

$$\mathcal{P} = N\mu_{12}\big[\sigma_{21}e^{i\omega_p t} + \sigma_{12}e^{-i\omega_p t}\big]. \tag{2.28}$$

Comparison with the Equation 2.24 leads to an expression for susceptibility as follows

$$\chi = -\frac{2N|\mu_{12}|^2\sigma_{21}}{\hbar\epsilon_0\Omega_p} \tag{2.29}$$

The above expression for χ is expanded for the experimental settings which are measured in a lab which is expressed in a more practical form

$$\chi = \frac{\sigma_0\rho(x,y)}{k_0}\frac{i\gamma/2}{\gamma/2 - i\delta_p + \frac{\Omega_c^2(x,y)}{\Gamma/2 - i(\delta_p+\delta_c)}}, \tag{2.30}$$

where, σ_0 is the on-resonance cross section which is defined as

$$\sigma_0 = \frac{\hbar\omega\Gamma}{2I_{sat}}, \tag{2.31}$$

where, Γ is the decay rate, I_{sat} is the saturation intensity.
In the absence of the control beam, i.e. $\Omega_c = 0$ the expression for χ reduces to that for a two level system

$$\chi = -\frac{\sigma_0 N(x,y)}{k_0}\frac{2\delta_p/\gamma - i}{1 + 4(\delta_p/\gamma)^2}. \tag{2.32}$$

The real and the imaginary parts are related to the macroscopic complex refractive index by the following equations

$$n_r = 1 + \frac{1}{2}Re[\chi], \tag{2.33}$$

$$n_i = \frac{1}{2}Im[\chi]. \tag{2.34}$$

The imaginary part is associated with the absorption due to on-resonant scattering of the light, while the real part is responsible for the phase shift encountered by the beam as the laser beam propagates through the medium. The lineshapes obtained from the imaginary part of the susceptibility are shown in the Figure 2.3 where the probe beam is scanned near the resonance while the control beam is set to the resonance. As the control power is applied, which results in a non-zero Ω_c, a transmission window opens up at the resonant probe detuning which was completely opaque. This process of creating artificial transmission using light is commonly known as electro-magnetically

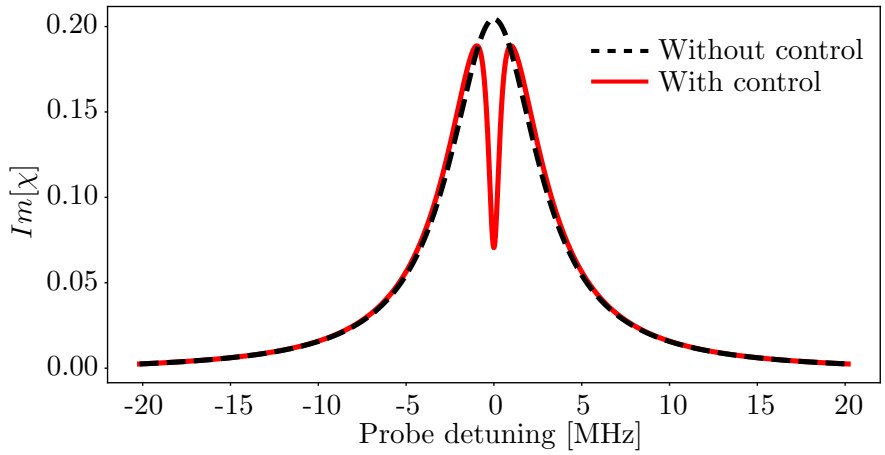

Figure 2.3.: Imaginary part of the susceptibility for the probe scan. In the presence and absence of the control laser.

induced transparency or EIT. In a two-level system, the typical lineshape appears as shown by the black (dashed) line. In the presence of the control beam, the transmission peaks appears as shown by the red (solid) line.
The Real part of the susceptibility which is responsible for the phase shift of the propagating beam which is shown in the Figure 2.4. The medium becomes extremely dispersive as the refractive index, n_r changes significantly with the laser detuning, ω_p. The value of $\frac{dn}{d\omega}$ is a measure of dispersion.

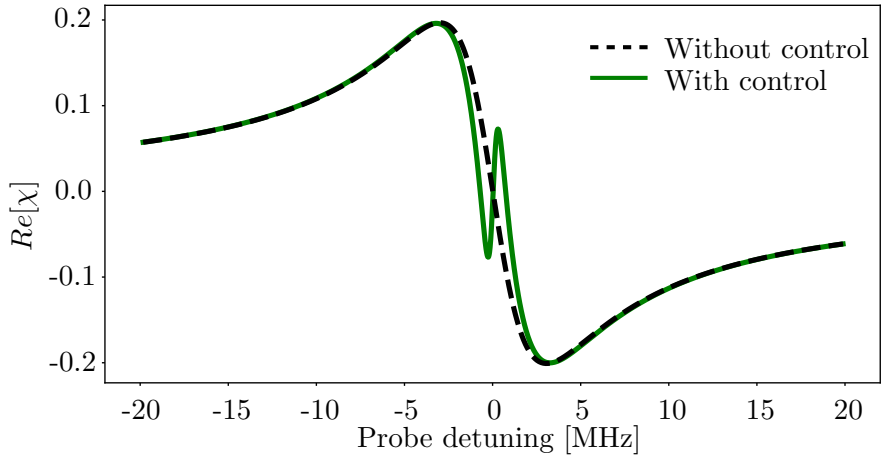

Figure 2.4.: Real part of susceptibility for probe scan. In the presence and absence of control laser.

2.1.2. Absorption

As has been discussed in the previous sections a light beam passing through a cloud of atoms encounters significant change by means of both the absorption and the dispersion. The results are quantified by the real and the imaginary components of refractive index. The absorption lineshapes are illustrated in this section while the significance of the dispersion is left for the Chapter 6. To quantify the values of absorption, as a figure of merit, optical depth, OD is estimated by

$$I = I_0 e^{-OD}, \tag{2.35}$$

where, I and I_0 are the intensities of the incoming and outgoing beam through the atomic medium. The transmission is defined as $I/I_0 = e^{-OD}$. Value of OD is obtained from the imaginary part of the refractive index as

$$OD = 2k_p n_i l, \tag{2.36}$$

where, k_p is the magnitude of the wavevector, i.e. $2\pi/\lambda_p$ and l is the cloud length through which the probe beam propagates. The results are illustrated in the Figure 2.5 for the various OD values.

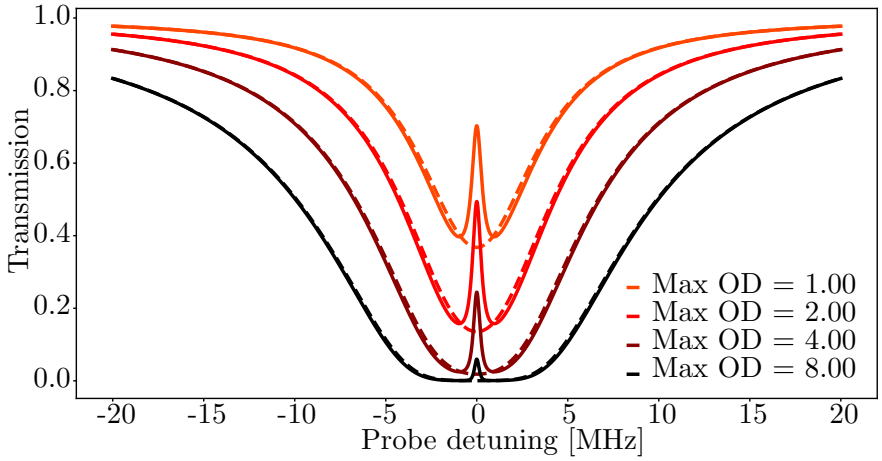

Figure 2.5.: Transmission signals for different optical depths. Dashed lines represent transmission without the presence of control field and solid lines for EIT lines.

2.1.3. Slow light

One of the remarkable results of the near resonant detunings is that the values of the both, $Im[\chi]$ and $Re[\chi]$ vary dramatically. The situation becomes a lot more interesting in case of EIT conditions. The refractive index, n_r is responsible for the propagation speed of the given wavepacket. This relates to the group velocity of the

light as follows,

$$v_{group} = \frac{d\omega_p}{dk_p} \tag{2.37}$$

where k_p is the wavenumber in the given medium and is related as

$$k = \frac{\omega_p}{c} n(\omega_p). \tag{2.38}$$

Now, using the Equations 2.38 and 2.37, the expression for the group velocity is obtained as follows,

$$v_{group} = \frac{c}{n + \omega_p \frac{dn}{d\omega_p}} \tag{2.39}$$

Depending upon the laser parameters, such as the power and the detuning the value of dispersion, $\frac{dn}{d\omega_p}$ could become extremely high. This results in extremely low group velocity. In terms of control Rabi frequency, Ω_c the group velocity is expressed as

$$v_g \approx \frac{\hbar c \epsilon_0}{2\omega_p} \frac{|\Omega_c|^2}{|\mu_{12}|^2 N}. \tag{2.40}$$

The dependence of v_g on the control Rabi frequency provides an easy way to tune the speed of the propagating light pulse in a medium. In certain cases, speeds of several m/s have been measured [45].

2.1.4. Dressed state picture

In a special case with $\delta_c = \delta_p = \delta$, the expression for the Hamiltonian given by the Equation 2.16 reduces to

$$H = -\frac{\hbar}{2} \begin{bmatrix} 0 & \Omega_p & 0 \\ \Omega_p & -2\delta & \Omega_c \\ 0 & \Omega_c & 0 \end{bmatrix}. \tag{2.41}$$

To obtain the eigenstates conveniently, a set of mixing angle terms are defined as follows,

$$\tan\theta = \frac{\Omega_p}{\Omega_c}, \tag{2.42}$$

$$\tan 2\phi = \frac{\sqrt{\Omega_p^2 + \Omega_c^2}}{\delta}. \tag{2.43}$$

The eigenstates for the Hamiltonian are

$$|\psi_+\rangle = \sin\theta \sin\phi |1\rangle + \cos\phi |2\rangle + \cos\theta \sin\phi |3\rangle, \tag{2.44}$$

$$|\psi_D\rangle = \cos\theta |1\rangle - \sin\theta |3\rangle, \tag{2.45}$$

$$|\psi_-\rangle = \sin\theta \cos\phi |1\rangle - \sin\phi |2\rangle + \cos\theta \cos\phi |3\rangle. \tag{2.46}$$

The state $|\psi_D\rangle$ is called dark state as it is evident from the above expression it has no contribution from the intermediate state, $|2\rangle$. This means that the lack of the overlap with the intermediate state $|2\rangle$ leads to no scattering of the laser beams, hence atoms in the dark state are transition forbidden. In other words, on the one hand once the atoms are prepared in $|\psi_D\rangle$ they remain there as the two states, $|1\rangle$ and $|3\rangle$ are long-lived as compared to $|2\rangle$. On the other hand the states, $|\psi_+\rangle$ and $|\psi_-\rangle$ can "leak" into the dark state due to the overlap between the atomic states $|1\rangle$ and $|3\rangle$. As a result, due to this unidirectional process, the atoms end up in dark state in a process known as *coherent population trapping* (CPT) [4]. Now, by adjusting the relative Rabi frequencies of the probe and the control beams, the contribution of the two long-lived stated to the dark state can be controlled. Let's assume the probe beam is very weak, i.e. $\Omega_p << \Omega_c$, that means the dark state mostly consists of state $|1\rangle$. By slowly increasing the power of the probe beam in an adiabatic manner, i.e. $t_{ramp} << 1/\Omega_c$, the contribution of the state $|3\rangle$ can be increased. Simultaneously, by reducing the control power the dark state can be prepared with full contribution from the state $|3\rangle$ in a process known as *stimulated Raman adiabatic passage* (STIRAP) [35].
The intermediate state in many cases is short lived thus causes limitations on the coherence time. In the case of the EIT processes, the intermediate state can be completely avoided and the coherence processes are then mainly dependent on the two long-lived states. Combined with the result from the Equation 2.40, the group velocity of the propagating probe beam can be reduced to zero by reducing the control Rabi frequency. This makes it a powerful tool to store the probe photons into the atomic ensemble. Here both, the photonic states and the atomic states are mixed together coherently in what is known as polaritonic states. Furthermore, by adiabatically ramping up the control laser power the stored probe photons can be retrieved on demand. Such precision control over light is being explored in the fields of quantum optics and quantum information.

2.2. Rydberg atoms

In the most simple atom – Hydrogen, the observation of the discrete energy lines is a profound example of quantum mechanical processes. The results were generalized by Johannes Rydberg and formulated as follows

$$\Delta\nu = \mathcal{R}\big(\frac{1}{m^2} - \frac{1}{n^2}\big), \tag{2.47}$$

where, m and n are integers corresponding to the associated transition states and $\mathcal{R}$ is the Rydberg constant. Later, the integers, m and n were interpreted as the principal quantum numbers by Bohr [14]. The value of the Rydberg constant, $\mathcal{R}$ is obtained as

$$\mathcal{R} = \frac{Z^2 e^4 m_e}{2(4\pi\epsilon_0\hbar)^2}, \tag{2.48}$$

where, Z, e, m_e and $\hbar$ are atomic number, electron charge, electron mass and reduced Planck's constant.

Atoms in the ground state are typically found in low lying energy levels with the principal quantum number, $n < 8$. By various means these atoms can be excited to higher principal quantum states. Rydberg atoms refer to the atoms when they are excited to principle quantum numbers beyond around 20, however there is no clear boundary and could range up to 100 or above. In a highly excited atom, the outer shell electron has a weak overlap with the nucleus and the remaining electrons. consequently, this loosely bound electron is prone to strong perturbations even in the presence of relatively weaker external fields. Such fields can be produced from charges, magnetic field, etc. including neighbouring atoms in the ensemble. These perturbations can be measured by means of the spectral features, such as lineshapes, shift, etc. which produce important information about the nature of interaction and the underlying physics. In addition to the highly enhanced sensitivity, the Rydberg atoms have shown extended lifetimes which is a extremely favourable requirement for exploring applications in the quantum memory storage, information processing and quantum sensing. In the upcoming subsections, some of the most exotic features are discussed along with the basic properties. Some of the interesting features are highlighted in the Table 2.1.

Properties	**n* scaling**	$5S_{1/2}$	$61S_{1/2}$
Polarizability	n^{*7}	$1.96e^{-7}$	$2.08e^{+2}$
Orbit radius	n^{*2}	$5.6a_0$	$4797.7a_0$
Lifetime at 0 K	n^{*3}	26.4 ns ($5P_{3/2} \rightarrow 5S_{1/2}$)	242.7 μs
Lifetime at 300 K	n^{*2}	26.4 ns ($5P_{3/2} \rightarrow 5S_{1/2}$)	105.0 μs
Blockade radius	$\sim n^{*1}$	$\sim$ nm	6.2 μm
Dipole moment ($nS_{1/2} \leftrightarrow nP_{3/2}$)	n^{*2}	$2.99\, ea_0$	$-2201.94\, ea_0$
Energy spacing ($nS_{1/2} \leftrightarrow nP_{3/2}$)	n^{*-3}	$3.84 \cdot 10^{14}$ Hz	$1.64 \cdot 10^{10}$ Hz

Table 2.1.: ^{87}Rb Rydberg atom properties. Comparison of typical values for $5S_{1/2}$ and $61S_{1/2}$ states. The values are obtained from [47].

2.2.1. Energy states

The configuration of a Rydberg atom resembles closely to a Hydrogen-like atom as the outer shell electron experiences an approximately central potential. This approximation breaks down for the case when the outer shell electron wave-function lies close

to the nucleus. A non-zero azimuthal quantum number, L further adds complexity in the model due to its angular dependence. A quantum defect, δ_{nLJ} is introduced to account for the deviation from the exact Hydrogen model. The mathematical form of the energy eigenvalues of a Rydberg atom is expressed as

$$E_{nLJ} = -\frac{hc\mathcal{R}}{(n*)^2} = -\frac{hc\mathcal{R}}{(n-\delta_{nLJ})^2}, \tag{2.49}$$

where, n^* represents an effective principal quantum number whereas n, L and J are the principal, azimuthal and total angular quantum numbers. Besides a simple model the Rydberg atoms offer a wide range of enhanced features suitable for the experiments in atomic physics. The main attraction comes from the ability to tune these features by adjusting very few parameters. For instance, By choosing a particular Rydberg state, n, L or J, the sensitivity towards external fields can be tuned to a high degree. Experimentally, this is achieved by addressing the associated state just by detuning a laser to a different frequency. As evident from the Equation 2.49, the line spacing for higher principal quantum numbers become narrower in the order of sub-nanometer wavelengths. This allows for easy addressing of multi-levels using a single tuneable laser source.

2.2.2. Long lifetime

The radiative coupling to the ground states are relative weak for higher Rydberg states as the wave function overlaps tend to diminish. As a consequence, the transition dipole matrix elements have significantly smaller values as compared to the atoms in the lower states. This results in prohibition in any decay to the ground states from the Rydberg states. The enhanced lifetime scaling, shown in the Table 2.1 is favourable for experiments that seek longer coherence times. In this case, the lifetime of immediate higher state ($5P_{3/2}$) in ^{87}Rb atoms is only 26.4 ns whereas that for the higher state is orders of magnitude longer. such long lifetimes allow for treating the excited states as an alternate "ground" state which is one of the key requirements for the realization of an EIT using Rydberg states. Applications like storage of photon and quantum information processing greatly benefit from such longer lifetime. However, at the room temperature the lifetime further suffers from alternate decay channels induced by the black-body radiation (BBR) as the broad spectral radiation initiates the coupling through the neighbouring states. This way atoms prepared in certain Rydberg state branches its coherence through multiple states which leads to an additional decay rate. The effective lifetime is calculated by

$$\frac{1}{\tau_{eff}} = \Gamma_0 + \Gamma_{BBR} = \frac{1}{\tau_0} + \frac{1}{\tau_{BBR}}, \tag{2.50}$$

where, τ_0 and τ_{BBR} are the lifetime at 0 K and at 300 K. Interestingly, even for the additional decay channels opened at room temperature the lifetime for $61S_{1/2}$ state is above 100 μs which is significantly large for certain time critical experiments.

2.2.3. Stark shift

In the presence of an electric field, the energy level of a Rydberg state gets shifted in a process what is known as Stark effect. It can be understood from the argument that the electron being loosely bound to the nucleus can encounter stronger deviation as compared to the ground state atoms where and outer shell electron is tightly bound. Using perturbation treatment, the Stark shift is estimated for a given pair of states which results in a shifted transition peak. It turns out that the first order Stark shift is absent due to the selection rule associated with the atomic transition, whereas the second order shift is still present which is quadratic in nature. Furthermore, the different sub-levels have significantly altered line shifts for a given electric field which is quantified as

$$\Delta = \frac{1}{2}\alpha|\mathcal{E}|^2, \tag{2.51}$$

where, α is polarizability. The value of α scales rapidly with the principle quantum number as presented in the Table 2.1. An enhancement of 9 orders of magnitude can be obtained for an $n = 61$ state. The high sensitivity has been utilized for sensing very weak electric fields such as those found near surfaces due to atom depositions [20]. In the later part in this thesis the field sensitivity aspects have been explored to estimate field inside the HC fiber used in the project.

2.2.4. Rydberg-Rydberg interaction

The large polarizability associated with the Rydberg atoms has significant enhancement in the sensitivity towards an external electric field. Such fields, however, can also be generated from the charge distribution of an another Rydberg atom in the near vicinity. Therefore, a strong electric potential between the two Rydberg atoms can be expected. In the classical picture such interaction can be understood by considering the two atoms with dipole moment, μ_1 and μ_2 separated by a distance R as shown in the Figure 2.6. Here, the interactions are considered among the positively charged cores and the negatively charged outer electrons. In the quantum mechanical description, the dipole matrix elements are expressed as $\mu_{ij} = \langle i|er|j\rangle$ and the dipole-dipole interaction is given by

$$U_{dd} = \frac{\mu_1 \cdot \mu_2}{|R|^3} - 3\frac{(\mu_1 \cdot R)(\mu_2 \cdot R)}{|R|^5}. \tag{2.52}$$

The second term in the Equation 2.52 signifies angular dependence and can be ignored for isotropic states, as in the case with S state [80]. In this case where the atoms are prepared in the same Rydberg state, $|nS\rangle$, the dipole interaction is expressed as

$$U_{dd} \propto \frac{1}{R^3}\sum_{\phi_1,\phi_2}\langle nS|\mu_1|\phi_1\rangle\langle nS|\mu_2|\phi_2\rangle = \sum_{\phi_1,\phi_2}\langle nS, nS|\frac{\mu_1\mu_2}{R^3}|\phi_1,\phi_2\rangle, \tag{2.53}$$

where, ϕ_1 and ϕ_2 are all the dipole transition allowed states. However, for practical calculations, the main contribution comes from $|nP\rangle$ and $|(n-1)P\rangle$ states. To illustrate the interaction, an excitation of a virtual photon can be considered as a result of

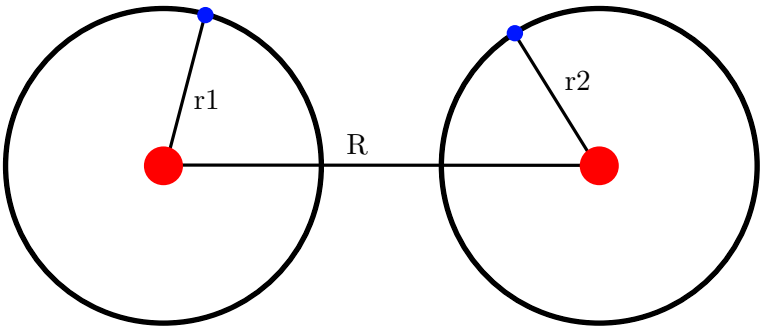

Figure 2.6.: Two atoms prepared in Rydberg state, separated by a distance R. The mutual interaction among the outer electrons and the nuclei has dipolar nature.

one atom undergoing transition from its initial quantum state $|nS\rangle$ to either $|nP\rangle$ or $|(n-1)P\rangle$. The wavelength associated with the photon lies in the microwave regime due to the narrow spacing for higher Rydberg states. In a typical experimental setting, the wavelength can be much larger than the inter-atomic distances and thus it satisfies the near-field condition. In this scenario, the virtual photon interacts with the neighbouring atom resulting in a state transition. Hence the dipole-dipole interaction exhibits in exchange of atomic energy states as

$$nS + nS \leftrightarrow nP + (n-1)P. \tag{2.54}$$

The right most part of the Expression 2.53 represents the interaction in the pair state basis. In that the initial pair state, $|nS, nS\rangle$ is coupled by U_{dd} to the state $|nP, (n-1)P\rangle$. The defect in the energy, i.e. $\Delta_F = E_{nP} + E_{(n-1)P} - 2E_{nS}$ is called Förster defect and has significance in describing the nature of interaction associated with the pair of atoms. The value of Δ_F completely depends on the atomic states and their response to external fields, in particular electric field. In the pair state basis, the Hamiltonian is written as:

$$H = \begin{bmatrix} 0 & U_{dd} \\ U_{dd} & \Delta_F \end{bmatrix}, \tag{2.55}$$

with the eigenvalues

$$U_{\pm} = \frac{\Delta_F}{2} \pm \sqrt{\left(\frac{\Delta_F}{2}\right)^2 + U_{dd}^2}. \tag{2.56}$$

Now, let's explore the the physically visualization of this type of interaction. In first case when the two atoms are far apart, the dipole-dipole interaction term, U_{dd} is very small. Therefore, in this approximation using Taylor expansion the equation 2.56 can be expressed as

$$\Delta U = -\frac{U_{dd}^2}{\Delta_F} = -\frac{(\mu_1\mu_2)^2}{\Delta_F R^6}. \tag{2.57}$$

Here, the expression can be seen as a van der Waals type potential with $V_{vdw} = -\frac{C_6}{R^6}$ with the coefficient, $C_6 = (\mu_1\mu_2)^2/\Delta_F$. Evidently, it can easily be shown that the value of C_6 scales with n^{*11} since Δ_F is similar to the energy spacing, it scales with n^{*-3}. With a given sign of the Förster defect, Δ_F the nature of interaction can be attractive or repulsive [8]. Experimentally, this can be achieved by selecting specific set of energy states in combination with an added electric field [78]. Moreover, the interaction strength scales inversely proportional to the Förster defect.
In another interesting regime where, the Förster defect is completely canceled out, i.e. $\Delta_F = 0$, the equation 2.56 can be simplified to

$$U_{\pm} = \pm\frac{\mu_1\mu_2}{R^3}. \tag{2.58}$$

In this situation, also called as Förster resonance, the energy scaling follows $U_{\pm} = \pm\frac{C_3}{R^3}$ where the C_3 coefficient has an n^{*4} dependence. The important feature here is the tunablity from R^{-6} to R^{-3} dependence that makes the atom-atom interaction a long range type.

2.2.5. Rydberg blockade

As is being discussed, high electric fields can be generated due to the excitation of one atom to Rydberg state which can shift the energy levels of a neighbouring Rydberg atom. If the Stark shift is beyond the characteristic laser linewidth, the atom would be off-resonant to the given transition and hence would not excite to the same Rydberg state. The inverse square dependence on the electric field forms a volume of a given radius, known as blockade radius where no further Rydberg excitation is possible. For a state, $n = 61S_{1/2}$ the Rydberg blockade radius is above $6\,\mu$m which is orders of magnitude larger than a single atom radius. One way of creating Rydberg excitation is by using three-level excitation in the case discussed under EIT section. In that the critical requirement for the Rydberg excitation is that the two lasers must match the respective transition lines. Within the Rydberg blockade radius, clearly the EIT condition is destroyed which leads to additional consequences. In the given blockade volume, once an excitation is made all the other probe photons would be absorbed. This result can be seen as extreme non-linearity induced at single photon level [92]. An illustration is presented in the Figure 2.7.
Another remarkable aspect of the Rydberg blockade can be seen as the excitation being shared among all the atoms within the given volume as there is a finite probability of each atom undergoing through the Rydberg excitation as illustrated in the Figure 2.8. This leads to a phenomenon known as collective excitation which enhances the light-matter coupling strength as represented by

$$\Omega_{tot} = N^{1/2}\Omega, \tag{2.59}$$

where, Ω_{tot} is the two-photon Rabi frequency of a single atom coupled to the light fields and N is the number of atoms within the blockade radius. In another words, the collective excitation represents Rabi oscillation as seen in a two level system but

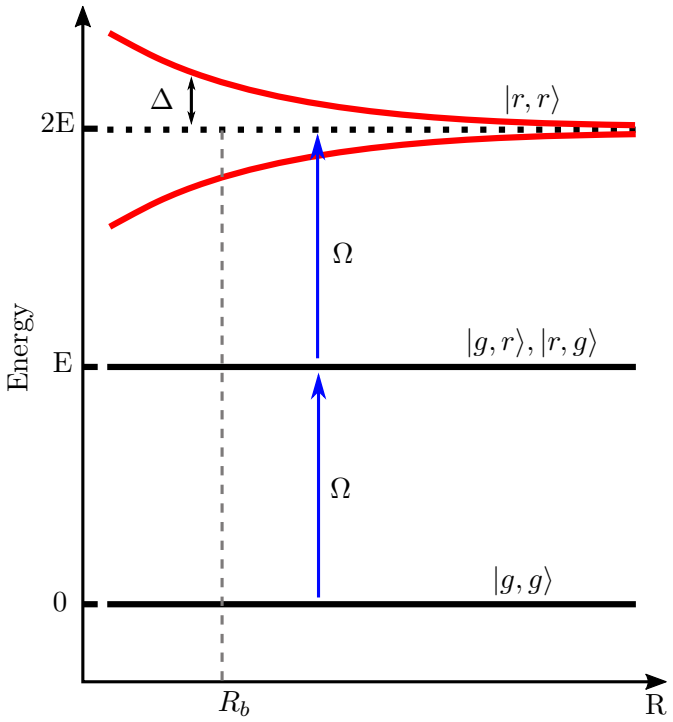

Figure 2.7.: Rydberg blockade. Excitation of two atoms to Rydberg states within the volume is prohibited. The red lines indicate the shifted energy line in case of pair excitation. The sign of the potential can be tuned to create attractive or repulsive potential.

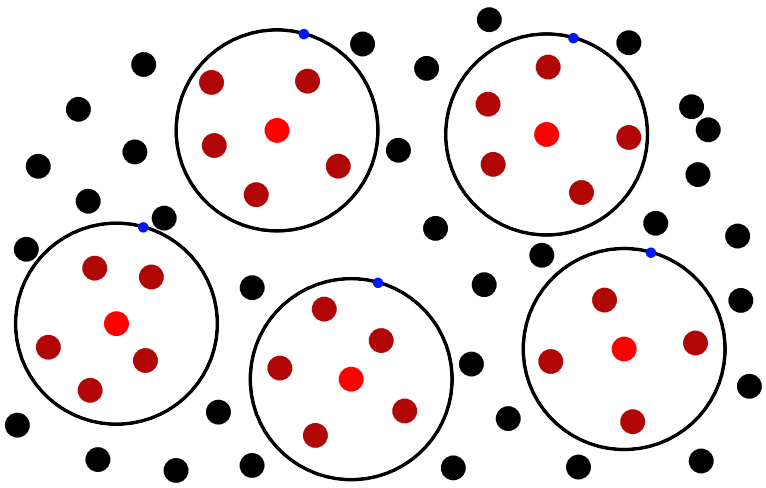

Figure 2.8.: Collective excitation within the blockade volume. Black dots represent ground state atoms. Brown and red dots represent atoms sharing the Rydberg excitation.

with an enhancement due to the multiple atoms present in the blockade volume. In this regard, the entire collection can be thought of as a super-atom with an scaled enhancement in light-matter coupling strength.

2.3. Rydberg EIT

In this section, the features of the two previously discussed sections, i.e. the EIT and the Rydberg atoms are combined together. On the one hand, through EIT processes a precision control over light is achieved by rendering the medium transparent or dispersive. On the other hand, the Rydberg atoms offer a range of enhanced interactions. The combined system has shown promising applications in the fields ranging from quantum simulation to quantum sensing, quantum information processing and communication.
For the experimental techniques, cold atoms provide a clean environment for precision measurements. In this case where the linewidth of the EIT lineshapes can be narrowed down to 100s of KHz since the measurements do not suffer from any Doppler shifts as the atomic motion is seized. The process of Rybderg excitation involves shining two lasers in a ladder configuration as depicted in the Figure 2.9. For Rb the two wavelengths are 780 nm and 480 nm for the probe and the control transitions. The laser detuning schemes shown in the figure need to be considered to obtain the two photon resonances. Due to the absence of any Doppler shift, the two configurations – counter-propagating and co-propagating cases show no difference on the spectral features. It is only for the experimental constraints, in case of co-propagation scheme, the strong control needs to be decoupled from the sensitive detector. The lineshapes are shown in the figure for different Ω_c. The two-photon resonances occurs at $\delta_p = -\delta_c$ for either cases. For increasing control power the transmission increases while it also increases the broadening. The outcomes are highly linked with the Autler-Townes splitting which is a regime where the control power is much higher such that the two peaks appear separately [6].
As was discussed previously, utilizing EIT process quantum information of a photon can coherently be stored to the atomic ensemble. Here, the strong tunability nature of Rydberg atoms can be introduced to effectively create photon-photon interaction. The EIT line is plotted in the Figure 2.10 where conveniently control laser is scanned while the probe laser kept on-resonance. This way the atomic absorption lineshape is completely removed from the study of EIT lineshape which will be of significant importance in the coming sections.

2.4. Rydberg EIT with thermal atoms

While it is spectroscopically very clean to work with cold atoms, the preparation and feasibility sets experimental limitation due to demanding constraints. Cold atom experiments require a systematic control of a large number of lasers and different fields. Measurements are limited to a fraction of time over it takes to prepare. Vapour cells

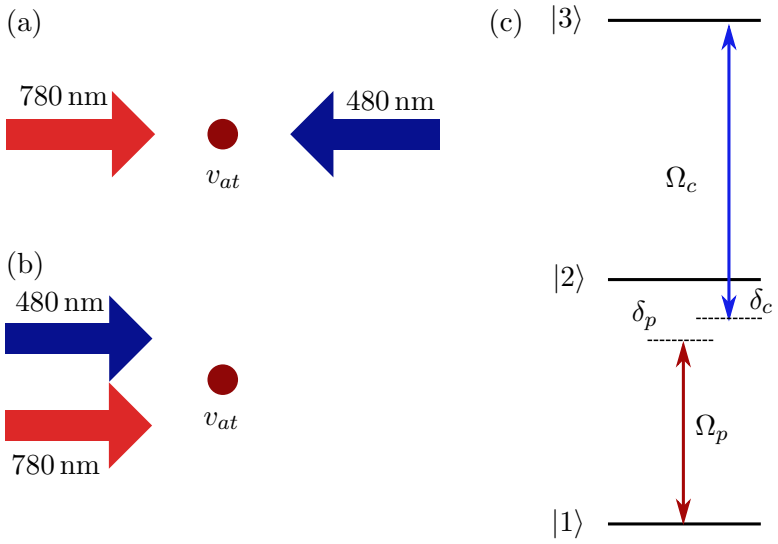

Figure 2.9.: EIT schemes: (a) counter-propagating and (b) co-propagating configurations. (c) Ladder type EIT scheme with probe and control detunings.

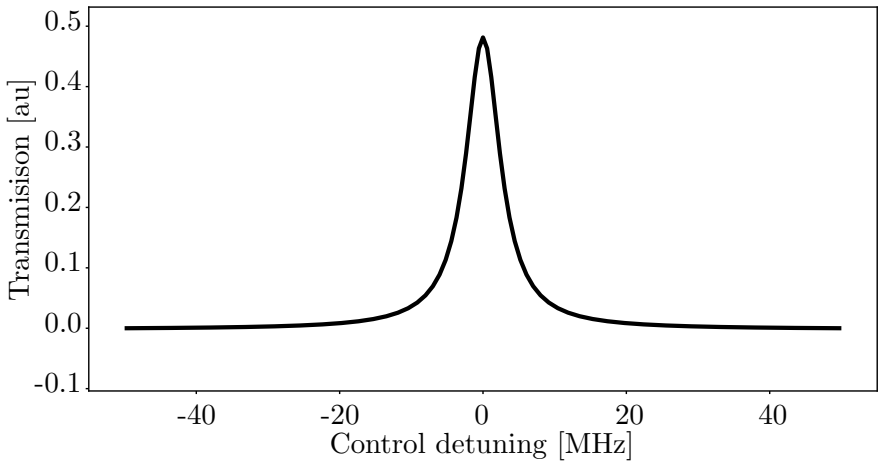

Figure 2.10.: EIT line shape for cold atoms. Control beams is frequency scanned and the probe laser is kept on-resonance.

filled with atomic samples have shown interesting results in certain experiments. In particular, EIT measurements when done in a Doppler free arrangement leads to much better line shapes comparable to that obtained from cold atoms measurements. In this case, the two configurations have significant effects on the detected spectral features. In one case, where the beams are in co-propagating, the Doppler shift adds to the two laser beams and the total effect is highly adverse. In the case where the beams are counter-propagating, the shifts tend to cancel each other and hence the results are much better. However due to mismatch in the wavelengths, the cancellation is not complete which results in deviation in the lineshape from the cold atom lineshapes.

To calculate the susceptibility, the atomic velocity distribution is integrated over the entire velocity range dictated by the temperature. The susceptibility from the Equation 6.8 for a given velocity class atoms is

$$\chi(v) = \frac{\sigma_0 \rho(x,y)}{k_0} \frac{i\gamma/2}{\gamma/2 - i(\delta_p + \delta_p^v) + \frac{\Omega_c^2(x,y)}{\Gamma/2 - i((\delta_p+\delta_p^v)+(\delta_c+\delta_c^v))}}, \tag{2.60}$$

where, δ_p^v and δ_c^v are the shift in the probe and control laser frequencies due to Doppler effect. The values are calculated by

$$\delta_c^v = k_c v_{at}, \tag{2.61}$$

$$\delta_p^v = k_p v_{at}, \tag{2.62}$$

where, k_p and k_c are probe and control wavevectors and v_{at} is the velocity of the atoms. The susceptibility for the complete velocity class is calculated by integrating over the given velocity distribution as

$$\chi = \int_v G(v)\chi(v)dv, \tag{2.63}$$

where, $G(v)$ is the Boltzmann distribution.

2.4.1. Doppler free line shape

The thermal velocity distribution of the atoms results in shifted EIT features as presented by the Equations 2.61. However, interesting geometrical arrangements can be made to cancel the shift in the lineshapes. It is apparent that for the ladder type EIT, counter propagating pair of the probe and the control lasers counteract the shift. To illustrate this, in the Figure 2.9(a) the atom with velocity would see one laser upshifted while the other laser downshifted. This way the EIT conditions are met. However for the case of $\Lambda-$type EIT, it would be the copropagating configuration that does the cancellation of the shifts.
A simulated model using the Equation 2.60 is plotted in the Figure 2.11(b). Here, the EIT lines for different velocity classes are represented by the color bar.
An easy visualization is made by plotting horizontal cuts for few velocity classes as shown in Figure 2.12(b). As it is clear from the fact that the Rydberg EIT in Rb atoms with this scheme where the two wavelengths $\lambda_p = 780\,\text{nm}$ and $\lambda_c = 480\,\text{nm}$ are distinctly different the Doppler compensation will not be completely effective. It is clearly noticeable that the peaks for different velocity classes are shifted apart.
For comparison, a hypothetical situation is presented in the same ladder-type EIT scheme but the two wavelengths chosen to be the same. Two photon Rydberg excitation in Yb atoms somewhat resembles this situation where the two transition lines are 399 nm and 395 nm. The simulated model as shown in Figure 2.12(a) clearly shows the peaks mainly stay at zero detuning confirming a complete cancellation of the Doppler shifts. The 2D EIT map of this scheme, shown in Figure 2.11(a) appears significantly different than the former case.

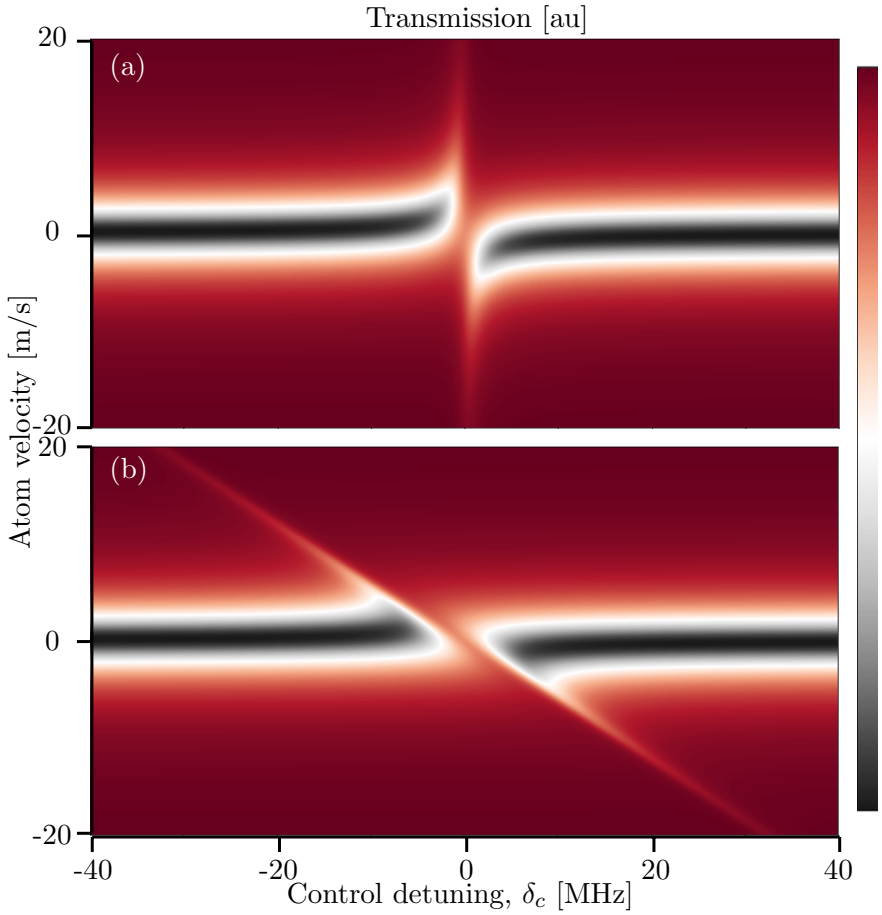

Figure 2.11.: Transmission contour for atoms of different velocity class, with (a) no Doppler mismatch and (b) Doppler affected EIT.

The complete EIT lineshape for the thermal vapour is compared in the Figure 2.13 by adding the contributions from all the velocity classes. The surprising dips can be noticed near ± 5 MHz detuning as a clear signature of Doppler mismatch. Interestingly, the signal from the cold atom and that from the hypothetical thermal vapour looks extremely overlapping.

2.5. Broadening mechanism

Even though the intermediate state involved in the EIT process has a linewidth of 12 MHz, the observed EIT signals are much narrower. Obviously, this is one of the features of the EIT that the intermediate state does not contribute in the dynamics. However, the linewidth of an EIT process still depends on the physical conditions such as the temperature of the vapour, power of the control laser along with the intrinsic coherence time. The study of the broadening mechanisms become important to un-

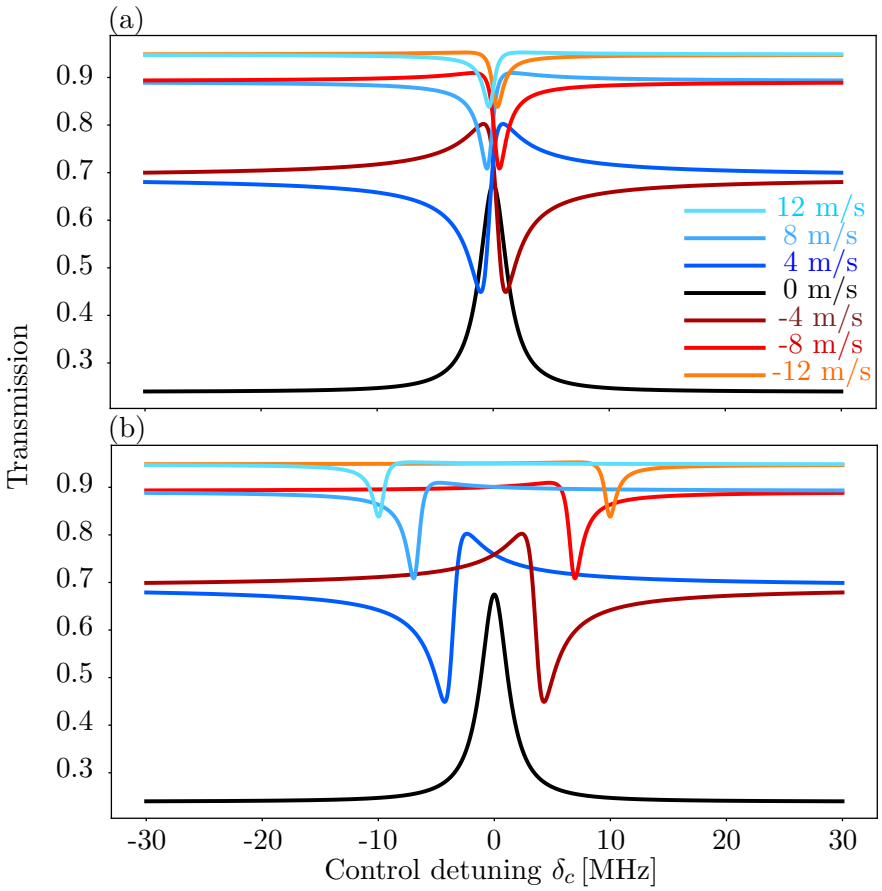

Figure 2.12.: EIT lines for several velocity class atoms towards the probe beam. No Doppler mismatch (a) EIT lines and Doppler affected traces (b) are shown.

cover the underlying physical processes. In what follows, some of these mechanisms are discussed.

2.5.1. Doppler mismatch

The model discussed for the thermal vapour illustrates the contribution of the Doppler mismatch. Here, due to the incomplete cancellation, the linewith and lineshape are both distinct from either Lorentzian or Voigt profile – convolution of a Gaussian with a Lorentzian function. Therefore, it becomes difficult to assign any characteristics linewidth. Instead, the complete thermal vapour EIT model needs to be solved in order to obtain the actual physical processes causing the broadening.

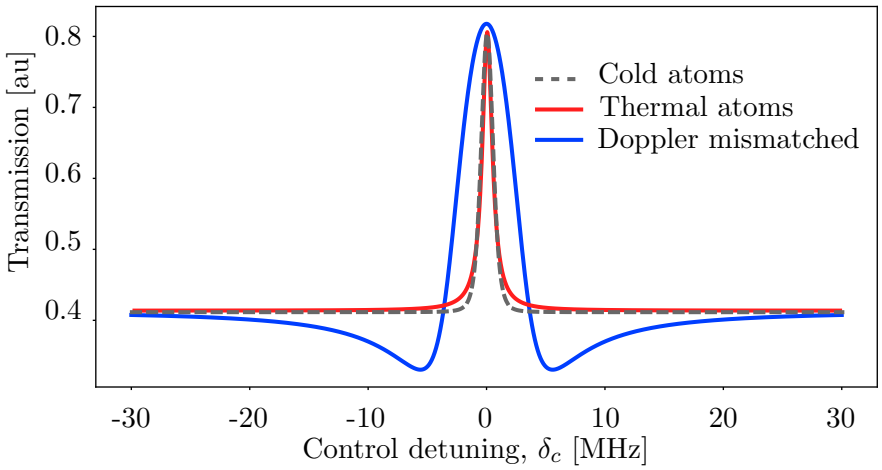

Figure 2.13.: EIT lines at different conditions. Scaled to fit for perspective.

2.5.2. Lifetime of Rydberg states

As seen in equation for χ the line shape has dependence on the coherences, γ and Γ for different states. Furthermore, the coherence timescale for the Rydberg state has n^{*3} dependence on the principle quantum number as shown in the Table 2.1. Therefore, for higher quantum state the linewidth gets narrower and is favoured for precision experiments as the other quantities also show positive effects.

2.5.3. Control Rabi frequency

The line width of the EIT line shape is roughly proportional to the control Rabi frequency for larger Ω_c as it adds to the original linewidth. As the control Rabi frequency is intensity dependent which has a spatial distribution, it becomes important to consider the complete spatial Rabi frequency distribution to understand the actual lineshape. Such scenario becomes extremely important when the control beam confinement is tightly overlapped.

2.5.4. Transit time broadening

During the probe time if an atom under detection moves away, it would result in drop of a signal associated with the transition. The duration of time is related uncertainty in measurements. The energy-time uncertainly, which results from Fourier transformation, dictates corresponding broadening in the observed linewidth. For cold atoms, the transit time effects are insignificant as the motion of the atoms are seized. The situation is not so favourable with the atoms at room temperature. In cases where a considerably large probe beam is used, the time an atoms takes to cross the beam could be significantly large resulting in linewidths of several 100s KHz which may be small as compared to other broadening mechanisms. However, when the beam sizes are very narrow, the interaction time becomes much shorter and the associated

linewidth needs to be considered. Atoms moving with average speed, v_{av} takes time,

$$t_{tr} = d/v_{av}, \tag{2.64}$$

where t_{tr} is transit time, d is beam diameter. The expression for v_{av} at a given room temperature is obtained by thermal velocity distribution,

$$v_{av} = \left[\frac{8k_BT}{\pi m_{Rb}}\right]^{1/2}, \tag{2.65}$$

where, K_B is Boltzmann constant, T is absolute temperature and m_{Rb} is mass of individual Rb atoms. The linewidth associated with the given transit time is obtained by

$$\Gamma_{tr} = 1/t_{tr}. \tag{2.66}$$

In the particular case, where Rb atoms at room temperature are filled inside a hollow-core fiber, the beam size is limited to 40 μm. The associated transit time is on the order of 150 ns which leads to a line broadening of $\sim$ 6 Mhz. Figure 2.14 shows the general transit time broadening for the atoms transiting different beam sizes at room temperature.

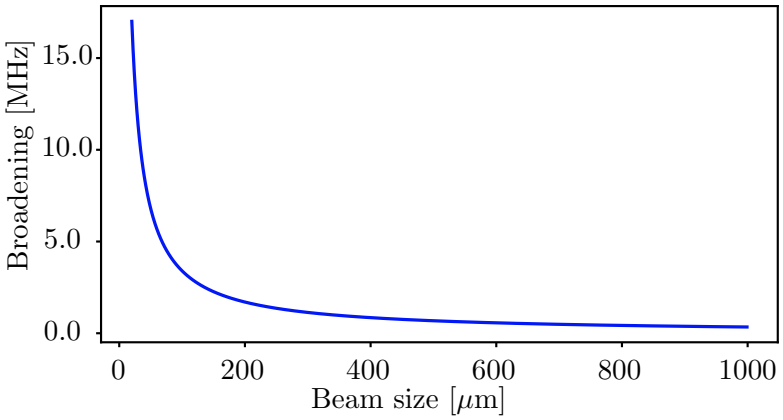

Figure 2.14.: Transit time broadening.

As a remark note: there are studies where certain measures are taken to reduce the atom-wall collision induced decoherence [7, 15] and hence the expression 2.66 for transit time broadening may not be valid. In fact, the similar enhancement in spin relaxation time with the atoms excited to the Rydberg states would be the desired goal. In the chapter 5 in this thesis, efforts are made to explore the possibilities.

3. Atoms in quasi-one dimensional confinements

One dimensional quantum systems have drawn considerable attention in the experimental as well as in theoretical physics. The simplicity and feasibility make such systems particularly suitable for practical applications. While such system represents a simple model, it still provides detailed information about the underlying physics in a quantum mechanical process. One of the crucial experimental realizations is a chain of trapped cold atoms which represents a many-body system with a plethora of control parameter space. Such as BEC to BCS cross-over transition has been observed in such system just by tuning the trap depth of the lattice confinement [39]. In the heart of such confinements lies the trapping potential created by coherent optical forces such as those created by dipole traps. However, in free space the trapping region is limited due to the optical wave propagation. This limitation adversely affects the light-matter interaction. To overcome this problem, a novel experimental system is presented in this chapter. Here, the cold atoms are transported inside a hollow core fiber making them confined for an infinitely extended quasi-one dimensional geometry. The key feature of the experiment is to gain a better control over the atoms along both, the transverse and the longitudinal directions. In atomic physics, generally light-matter coupling strength is weak in nature. A simple approach is to extend the region of light-matter overlap so that the encountering photons spend longer time together with the atoms. For a naturally limited scattering rate, this extension in interaction time would scale up the total number of scattering events.
In a free-space trapped-atom configuration, due to the limited Rayleigh length and the large blockade radius, it has become a challenging task to excite more than two Rydberg atoms in a chain. An important motivation concerning this project is to overcome this limitation and explore physics with several Rydberg blockades in a chain. The setup presented in this project promises to overcome the limitation by creating an extended trapped atomic cloud. Thus the setup provides an ideal condition for the excitation of multiple Rydberg atoms in a chain. Creation of interacting photons and thus interesting regime such as Luttinger liquid or fermionization of photons are some of the long term goals [63, 65].
In this chapter, a general principal of optical trapping is introduced with the limitations of free space trapping. The usage of a hollow-core fiber as a remedy to overcome the confinement lengths is presented in subsequent sections. To gain a better axial control over the atoms, a conveyor belt is realized by creating a standing wave of trapping field which allows for a precise positioning of the cold atoms along the fiber length.

3.1. Free-space beam propagation

In free space, as shown in Figure 3.1, a Gaussian beam is confined using a lens which is characterized by the Rayleigh range,

$$z_R = \frac{\pi w_0^2}{\lambda}, \tag{3.1}$$

where, w_0 is beam waist and λ is the wavelength of the propagating beam. At distance, z_r away from the focal point, the beam size increases to $\sqrt{2}$ times the beam waist. It is clearly evident that for a tighter focal point, i.e. smaller w_0, the confinement length, z_R becomes smaller.

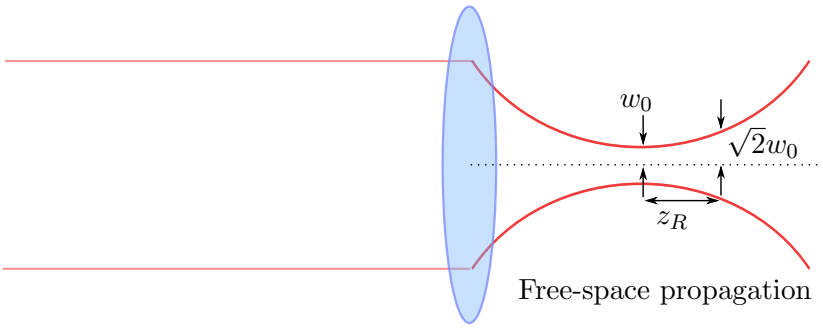

Figure 3.1.: Beam confinement in free space using a lens leads to immediate expansion.

A general form of a Gaussian beam evolution is given as

$$w(z) = w_0\sqrt{1 + (\frac{z}{z_R})^2}, \tag{3.2}$$

where, z is the axial distance from the focal point. The beam size expansion takes a linear form for larger distances.

3.2. Optical dipole trap

In the presence of a light-field, a two-level atom shows response that depends on the wavelength of the light beam. When the laser beam and the atomic transition frequencies are the same, it results in a resonance condition. In this case, the scattering of photon from the atom is maximized. Each scattering event imparts a momentum to the atom which is equal and opposite to the scattered photon. This is the underlying principle explored for laser cooling techniques by manipulating the atomic motion. However, as discussed in the earlier chapter, this process has a random nature which induces decoherence phenomena in a quantum system. For storage of a quantum system such traps are highly restricted.
Interesting results have been explored in the case, when the laser detuning is kept very far from the atomic transition. In a classical picture, the charge distribution

of an atom responds to the electric field present in the light beam. The magnetic interaction is much weaker and hence it is ignored. It is the induced dipole moment due to the light field which in turn creates a potential for the atom when it interacts with the light field. At this stage, depending upon the sign of laser detuning the atom either gets attracted to or repelled from the laser beam. In case, when the laser detuning is negative, i.e. the electric field oscillation is slower than the atomic transition frequency, the atomic charge distribution is capable of following the electric field change. Such process leads to attractive potential for the atoms. Conversely, for the blue detuning case, the induced dipole of an atom does not follow the change in field hence it encounters a repulsive potential. For a Gaussian beam geometry, the trapping laser has to be red detuned in order to trap the atoms. This type of trap is known as dipole trap for the reasons explained here.
The off-resonant scattering and the trap depth depend on the laser detuning as

$$\Gamma_{sc} \propto 1/\delta^2, \tag{3.3}$$

$$U_{dip} \propto I/\delta, \tag{3.4}$$

where δ is the detuning of the laser and I is the laser intensity. Even though the proportionality constant for scattering rate is higher, the steeper $1/\delta^2$ term rapidly decays to zero while, the dipole trap term is still non-negligible.
For this experiment, the laser was tuned to 805 nm which corresponds to a negative detuning for all the major transition lines. The total force is estimated by considering both, the D1 and the D2 lines. Even though the D1 transition strength is weaker, the laser detuning is rather small for this transition hence its contribution can not be avoided. The exact trap depth of a dipole beam is expressed in the forms of detunings from the D1 and D2 lines as

$$U_{dip} = 2\pi c^2 \Big[\frac{2\Gamma_{D2}}{\omega_{D2}^2 \Delta_{D2}} + \frac{2\Gamma_{D1}}{\omega_{D1}^2 \Delta_{D1}}\Big] I(r,z), \tag{3.5}$$

where, Δ_{D1} and Δ_{D2} are detunigs from the corresponding energy states and the ω_{D1} and ω_{D2} are the on-resonant transition frequencies for the $D1$ and $D2$ states.
Now, considering a typical Gaussian intensity distribution, the atoms are attracted towards the center of the beam as the trapping potential is minimum at the focal point as illustrated in Figure 3.2.
For the focusing Gaussian beam using a lens, the atom density takes the shape of the dipole trap beam which has significant importance in manipulation of the atomic cloud. In this case, the atom distribution is governed by the potential which has a wider spread along the beam propagation direction. As a result, position control over the atoms is not precise. A strong periodic longitudinal modulation is introduced to trap and precisely locate the cold atoms which is discussed in the next section.

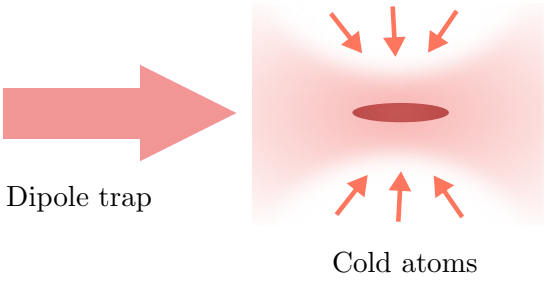

Figure 3.2.: Atoms trapped in optical dipole trap.

3.3. Optical lattice

The limitation due to the smooth and shallow potential along the beam propagation axis is broken by an additional trapping beam from the counter direction. In the case, when the two counter-propagating laser beams are derived from the same source, i.e. the phase and the frequency stay fixed, the two beams form a standing wave pattern. This results in longitudinal intensity modulation with a periodicity of $\lambda/2$. The atoms are attracted towards the intensity maxima and thus they end up trapped in the periodic potential. This resembles the lattice configuration as seen in a solid state crystal, thus it is widely known as optical lattice.
The optical potential for the lattice configuration mainly follows the Equation 3.5 with a modified intensity pattern

$$I(r,z) = I_0 \exp\Big(-\frac{2r^2}{w(z)^2}\Big)\cos^2(\phi - kz), \tag{3.6}$$

where, ϕ is the relative phase between the two lasers and k is the wavenumber associated with the laser beam. The intensity for the two laser beams is modified as

$$I_0(r,z) = \frac{2P}{\pi w(z)^2}, \tag{3.7}$$

where, P is the power in each of the beams. For maximum intensity modulation, the powers in each of the beam is kept equal besides the spatial overlap. The intensity pattern and subsequently the trapping potential simulated for the lattice configuration is illustrated in the Figure 3.3. Note the scale is exaggerated for visual clarification.

3.3.1. Conveyor belt

Atoms trapped in the optical lattice have tight radial confinement due to beam focusing. However, the axial confinement is even more steeper due to the formation of standing wave as a result of interference which has extent of $\lambda/2$. Atoms stay trapped in the local potential wells even though the global minima does not coincide with it. Such confinement has been explored for trapping and isolating atoms for quantum mechanical experiments. In such configuration atoms are trapped from an

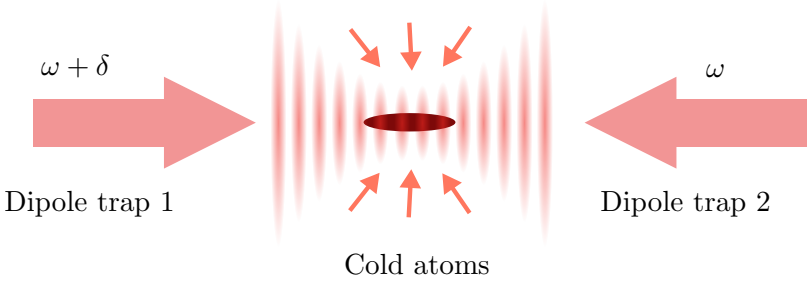

Figure 3.3.: Atoms realized in optical lattice with $\delta = 0$.

accessible region, i.e. MOT cloud and they can be transported to regions which are inaccessible [70, 61].
At this stage, it turns out from the Equation 3.6 that the axial position of the lattice sites can be shifted by modulating the phase, ϕ. The trapped atoms will now follow the potential and occupy the new location given that the change in ϕ is slow enough. The constraints on the rate is described by the adiabaticity condition

$$\dot{\phi} << \omega_{trap}, \tag{3.8}$$

where, ω_{trap} is the trap frequency. Under this condition, the transport velocity of the atoms is given by

$$v(t) = \frac{\lambda}{2}\delta. \tag{3.9}$$

Here, it is to be noted that $\delta = \dot{\phi}$. Now, by introducing a phase shift in one of the laser frequency will shift the lattice position, keeping the same lattice periodicity. In a typical experiment, one of the lasers is detuned precisely creating a continuous moving lattice, known as optical conveyor belt. With the help of optical conveyor belt, atoms are trapped and transported along the optical lattice beams in a highly controlled manner.

3.4. Light-matter interaction

The light matter interaction is achieved by overlapping a probe beam along with the atomic cloud. As a figure of merit, OD signifies the strength of coupling. For a given atomic density, the OD scales with the length of the interaction length, l as

$$OD \propto \rho l, \tag{3.10}$$

where, ρ is atomic density.
As it is clear for a free space beam, the length of the interaction region, l is roughly equal to the Rayleigh range, z_R which sets a natural limitation on the maximum OD. Even for atomic cloud trapped in an extended length by other means such as magnetic trapping [67], the probe beam does not stay overlapped with the entire atomic region. Hence, this technique results in a limited light-matter interaction strength.

A way to overcome this limitation is to utilize a waveguide such as an optical fiber. However, in order to accommodate both, the light beam and the atoms, a typical solid core fiber fails to meet the goal. An ideal solution would be an empty core waveguide where atoms can potentially be filled in as illustrated in Figure 3.4. In the guided geometry, the Rayleigh range has no limitation that is found in free-space propagation. This feature can be utilized to extend the length, l for macroscopic distances ranging several cms as opposed to the free-space case where this length is limited to few 100's of μm. ODs above 1000 have been realized in such simple arrangements [12]. Such goal is met by hollow core fibers which is the central topic of discussion for the next section.

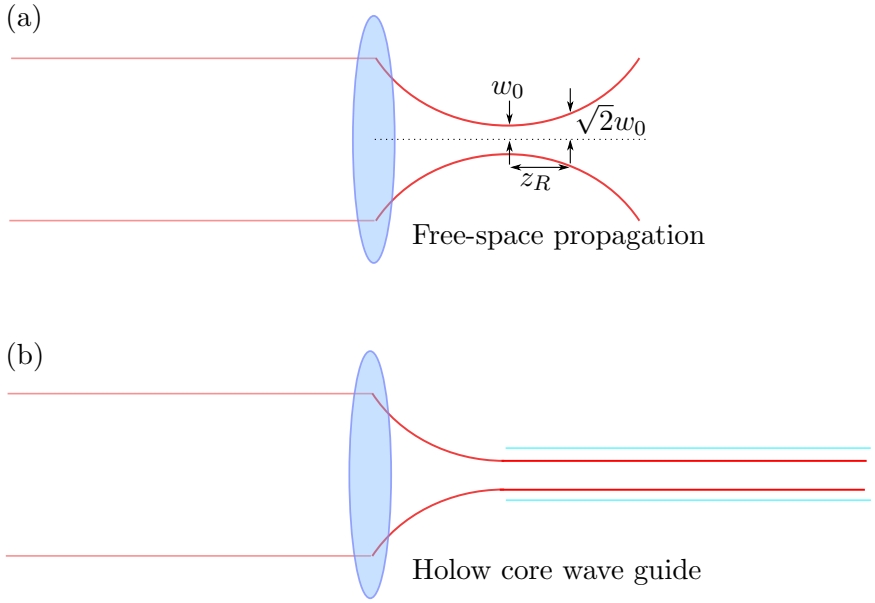

Figure 3.4.: Light beam diverges in free space. A guided wave stays confined.

3.5. Hollow-core fibers

Guided transmission of light has been critical and revolutionary to a wide range of applications. As a typical example, optical fibers have been implemented for along with scientific research, inter-continental high speed data transfer via sea-link fiber cables. In a typical atomic physics lab, fibers are utilized for carrying light close to the main experiment. Common to all these fibers, the principle of light guiding relies on the total internal reflection. A necessary step for this condition is a definite relationship between the refractive indices on the core and the cladding. In particular, the refractive index of the core material needs to be higher than the cladding in order to support the guiding mechanism. Such conditions, however, set limitations on manipulation of light. For example, transport of high power laser beam could induce non-linearity in the core medium which can lead to damages or losses. To circumvent

the issues, in the recent times a different approach have been made to guide light which crucially relies on the light propagation through the empty space in the core. This not only allows for high power transmission but also offer very low or no distortion on the light field. Moreover, the empty core now can be filled with atoms or molecules to produce a range of interesting physics in a confined geometries which otherwise is limited due to free-space beam divergence as has been discussed in the previous sections.

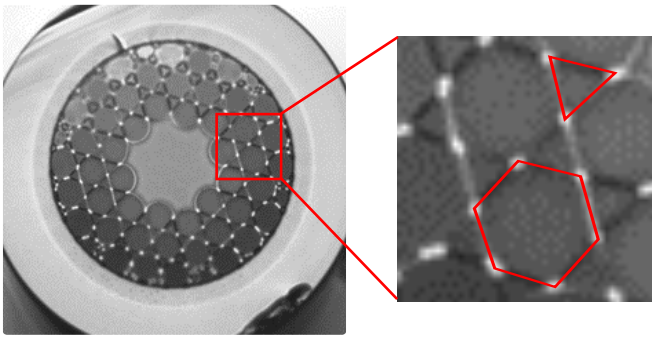

Fiber tip

Figure 3.5.: Cross section of the fiber. Empty core is surrounded by lattice structure which is responsible for light guiding. Zoomed shot of lattice structure indicating Kagomé type lattice.

The fibers used for this work are produced in the group of Dr. Fetah Benabid at XLIM, Limoges, France. A Kagomé type lattice structure of the core is shown in the Figure 3.5. The periodic lattice structure is responsible for an interference pattern which has none of very small values for the outside the core region. In a process known as inhibited coupling, the guiding mechanism is well explained [21]. With such a large core size, the fiber is highly multi-moded. As a result higher spatial order mode of light can be excited and supported by the fiber. A critical requirement for the trapping and transporting of atoms utilizes the Gaussian beam shape. Moreover, the light-matter overlap for creating strong interaction demands guiding of the same mode. Hence, a careful coupling procedure is needed in order to excite the fundamental mode of light into the HC fiber. In what follows the characterization procedure of the fiber is presented in the coming subsections. Another technical aspect concerning the cleaning of the HC fiber for UHV compatibility is discussed in the Appendix C.1.

3.5.1. Light guiding

One of the key requirements for the chosen fiber is the guiding properties of the different wavelengths which are required for trapping and transport of atoms followed by two-photon Rydberg excitation. In particular, the trapping and guiding is achieved by a laser at 805 nm. The probe and control lasers for Rydberg EIT are at 780 nm and 480 nm. An important aspect here is to observe the mode quality in addition to

the high coupling efficiency for all the different wavelengths. The test and characterization of the mode shape and the coupling efficiency are performed separately before installing the fiber inside the UHV chamber to benchmark the fiber properties.
In the Figure 3.6(a), the test and characterization setup is shown where the HC fiber can be mounted on an XYZ translation stage. A lens mount is placed in front of the fiber tip to accommodate lens of different focal lengths as well as a microscope objective for a detailed mode optimization of the outcoupling beam. The outgoing beam is recorded on a sensor for further analysis. Once the fiber is qualified for the experiment, it is then placed horizontally inside the UHV chamber in a V-groove mount shown in the Figure 3.6. No additional force is applied to hold the fiber in position since any external force can stress the fiber resulting in a scrambled mode. The hanging ends of the fiber is not of any concern as the fiber is sufficiently stiff. This claim is also confirmed by observing no vibration of the light beam that comes out of the fiber end.

(a)

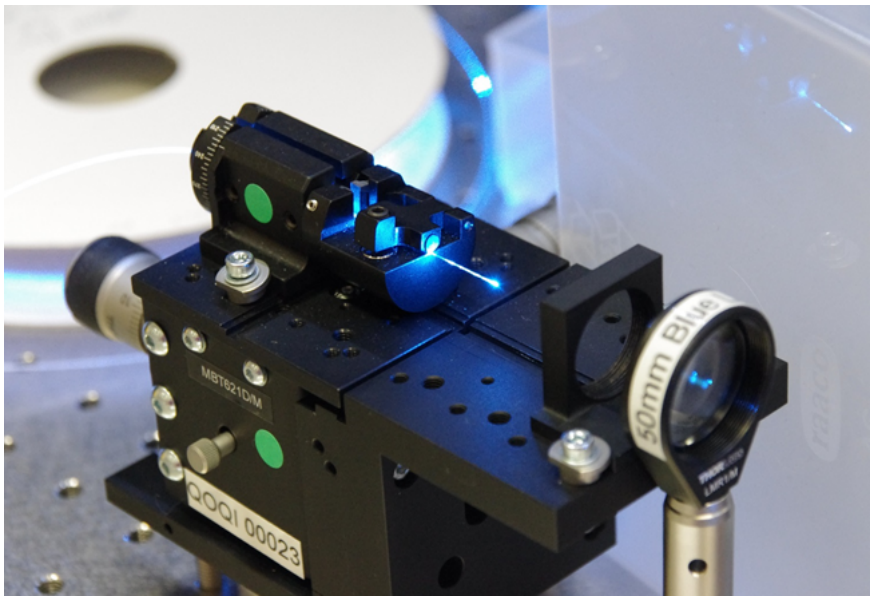

(b)

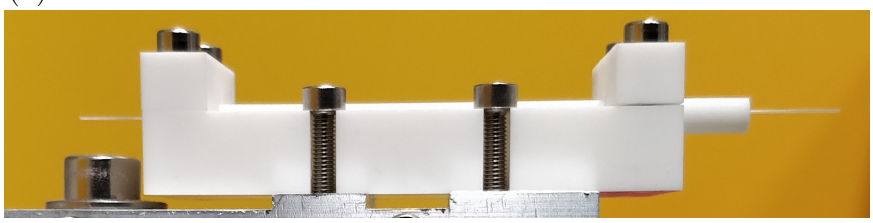

Figure 3.6.: (a) HC fiber characterization setup. Fiber position adjustments made with a micro-meter knob. (b) The fiber placed in a ceramic V-groove positioned horizontally inside the UHV system

The coupling of a wideband spectrum of light in the fiber is a challenging task, particularly for the reason that the large fiber core size $\sim 50\,\mu$m is capable of guiding higher order modes. In this case, the usual optimization technique where the output power is maximized, fails to work. Misaligned beam can still be guided through with little or no drop in the total power. The strategy here is to observe the mode shape and optimize for a Gaussian shape. In the Figure 3.7, a set of different mode profiles are displayed. The focal length of the lens and the incoming beam diameter is selected to match the mode field diameter (MFD) of the fiber by using Gaussian optics. In the initial stage, when the incoming beam just hits the fiber cladding, the Kagomé structure pattern can be illuminated as seen in the Figure 3.7(a). By iteratively optimizing the angle and the lens position of the beam, the coupling in the fundamental mode can be enhanced. The results are indicated by the Figures 3.7(b), (c) and (d). An indicator of a good coupling is that the mode shape starts to appear smooth and less sensitive to fiber movements.

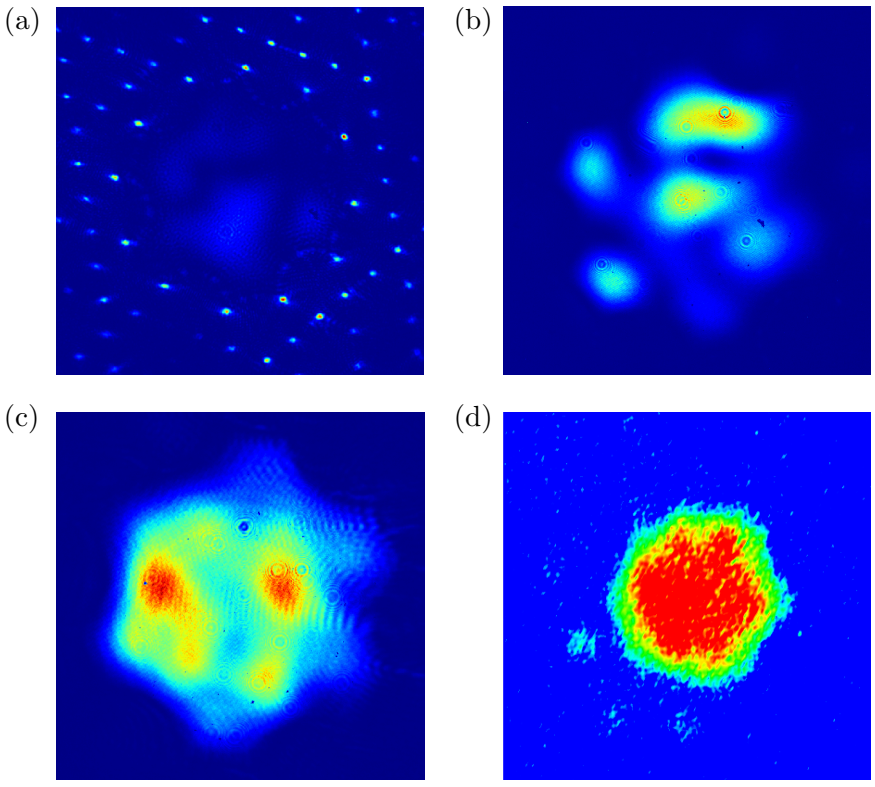

Figure 3.7.: Near-field mode profile at different coupling stages from worst (a) to best (d). The hexagonal pattern is an indicator of the 6 periodic edges of the core.

Different wavelengths are detected for the near field and the far field configurations as shown in the Figure 3.8. The coupling efficiency for all the wavelengths is obtained above 95 % which is a favourable for the atom transport and the EIT spectroscopy.

After qualifying the fiber characteristics for this project, it is then implemented in the main experiment.

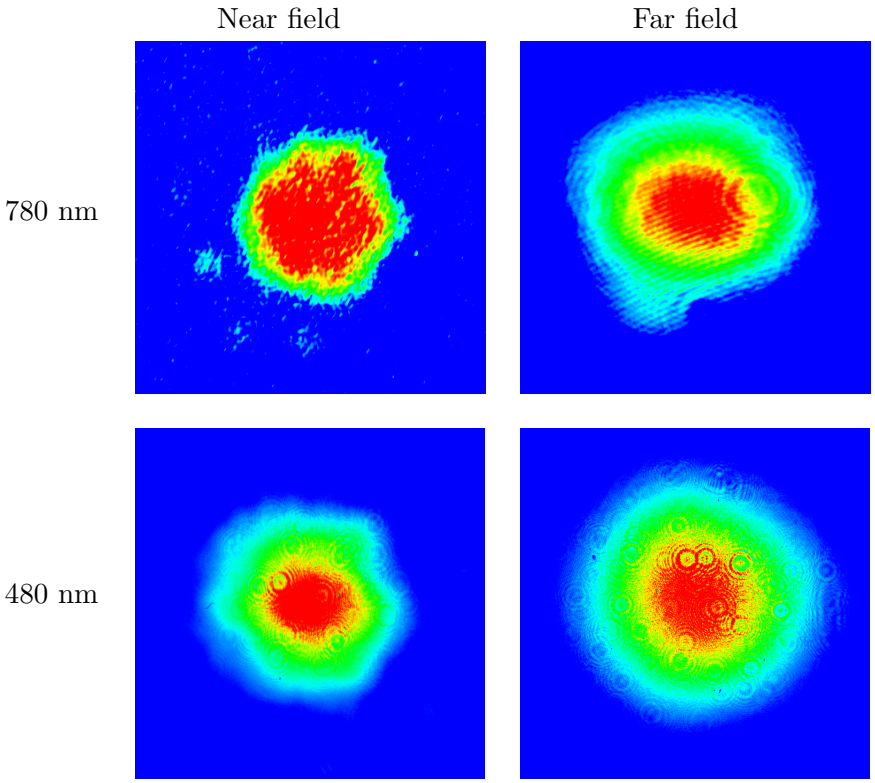

Figure 3.8.: Near-field and far-field intensity profile for different wavelengths.

3.5.2. Mode matching

One of the key requirements for the formation of standing wave is the overlap of the counter-propagating dipole trap beams. Particularly interesting is to explore the feasibility in the cases where the beams are propagating through the HC fiber. As the HC fiber is highly multi-moded, the quality of overlap is not always guaranteed to be perfect. For the simplified fiber setup shown in Figure 3.9 the reasonable way is to roughly couple the dipole trap beam, DT1 into the HC fiber. The outgoing beam is coupled into the DT2 single mode fiber. Now, retracing the path, the dipole beam, DT2 is overlapped and coupled into the HC fiber. The transmitting beam is now coupled into the DT1 fiber. By improving the coupling iteratively, the best mode overlap is achieved. visual verification of the far field images also confirms the coupling quality.

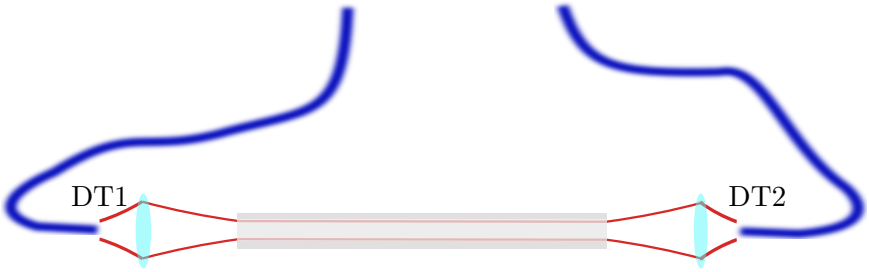

Figure 3.9.: Dipole trap beams mode overlapping.

3.6. Atom-HC fiber interface

To guide cold atoms into hollow-core fibers, dipolar forces are utilized. Cold atoms are trapped in MOT and further cooled and positioned in front of the hollow-core fiber as sketched in the Figure 3.10. A dipole trap beam passing through the hollow-core fiber overlaps with the atomic cloud. The initial trapping potential for the atoms are lowered down while increasing the dipole beam intensity. This results in transfer of atoms into the dipole beam intensity maxima. The untrapped atoms disperse away due to both, gravity and thermal velocity distribution. As it is evident the intensity of the dipole beam increases towards the fiber tip as the confinement gets narrower. Hence, the atoms naturally follow towards the fiber tip as shown in Figure 3.10. These atoms keep going further and further inside the fiber as the potential is favoured for the atoms. This way a controlled radial confinement is realized to fill the fiber. However, in order to study the atom transport process as well as how light propagates through such extended cloud, axial control additionally would be an immediate requirement.

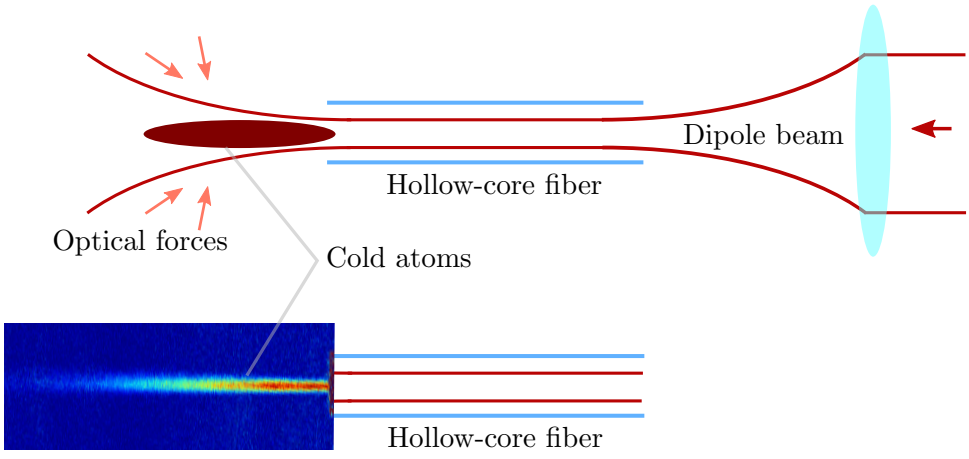

Figure 3.10.: Cold atoms trapped in dipole trap moving toward hollow-core fiber. Absorption image of cloud with fiber end is overlaid with sketch.

As discussed in the previous section, in order to control the atoms along the fiber axis, another dipole beam is overlapped through the fiber from the counter-propagating direction. This is to realize an optical lattice through the fiber is sketched in Figure 3.11. At this stage the atoms get trapped in the extended optical lattice sites.

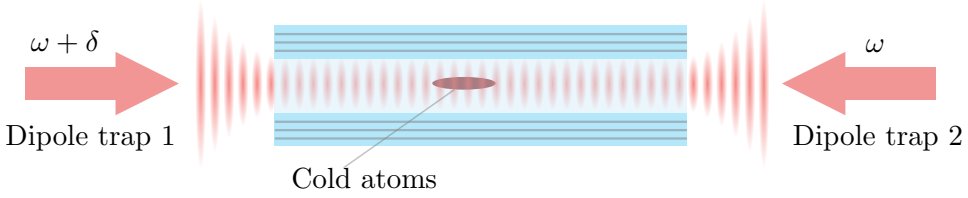

Figure 3.11.: Schematic of the cold atoms in optical lattice.

By controlling the detuning of either of the laser beams, the trapped atoms can precisely be moved with a desired speed which is obtained by the Equation 3.9. The relative detuning of the two lasers are controlled by a commercial FPGA controlled DDS solution, flexDDS by Wieserlab. The control program in our lab is developed and described in this bachelor's thesis [89]. These RF sources drive two separate AOMs through which the dipole beams are passing as shown in Figure 3.12. The tuneable Ti:Sapphire laser is the original source of the 805 nm. By tuning the absolute frequency, the trap depth and the scattering rates can be adjusted which follow the Equation 3.5. The source laser beam is seeded to the two separate thermally stabilized tapered amplifiers (TA). The output beam passes through optical isolators and beam shaping optics through two separate AOMs. The frequency of the AOMs are controlled by a DDS synthesizer synchronized to a single clock source. The frequency of the two AOMs are adjusted independently to high precision which provides a high degree of control over the atomic position. Additionally, the RF amplitude of the AOMs can be adjusted to control the trap depth of the trap. Using TTL controlled switches, the output power is enabled or disabled at very high speed that has significant importance for the detection procedure which is discussed in the next chapter.
With the experimental setting shown in the Figure 3.12, the optical lattice through hollow-core fiber is realized. A detailed study of the transport of cold atoms is described in these theses [98, 59]. In the Figures 3.13, the absorption images of atoms reaching the HC fiber tip is presented. Here, by setting the detuning, the atoms are set into motion. The detuning is reversed back to halt the atom at a desired location. The cloud is detected along the transverse axis using the absorption imaging to obtain the position, number of atoms and the temperature. For the controlled parameter space, the transport efficiency of above 70 % has been achieved. Temperature of the atoms stay below 300 μK with a lifetime above 500 ms. Once the atoms are transported inside the fiber, the usual detection scheme fails to work. This leads to establish an independent detection scheme using a weak probe beam passing through the HC fiber and is a part of separate discussion for complexity involved with beam propagation. The experiment and the theoretical model are discussed in the Chapter 6.

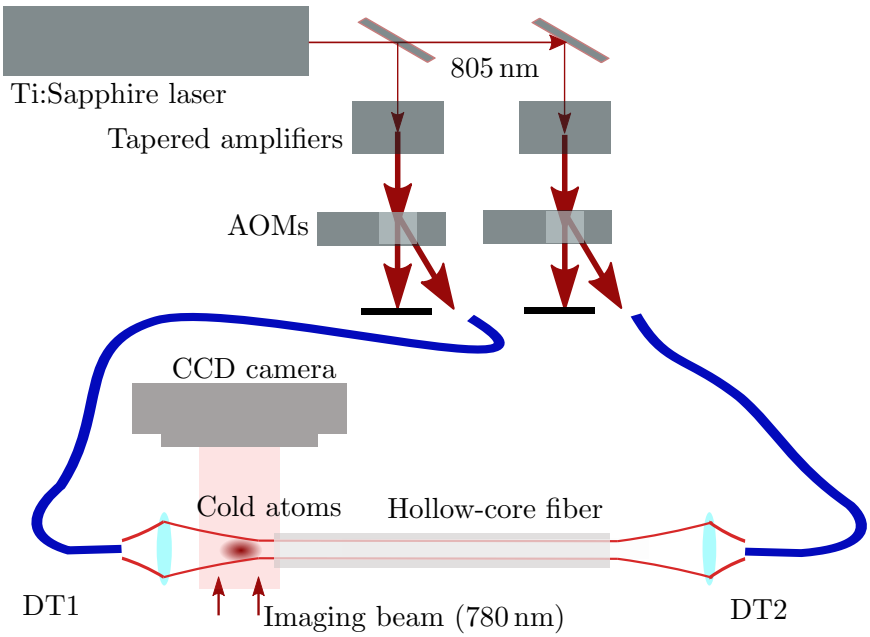

Figure 3.12.: Dipole laser schematics. Ti:Sapphire laser produces tuneable wavelengths which is then amplified using TAs.

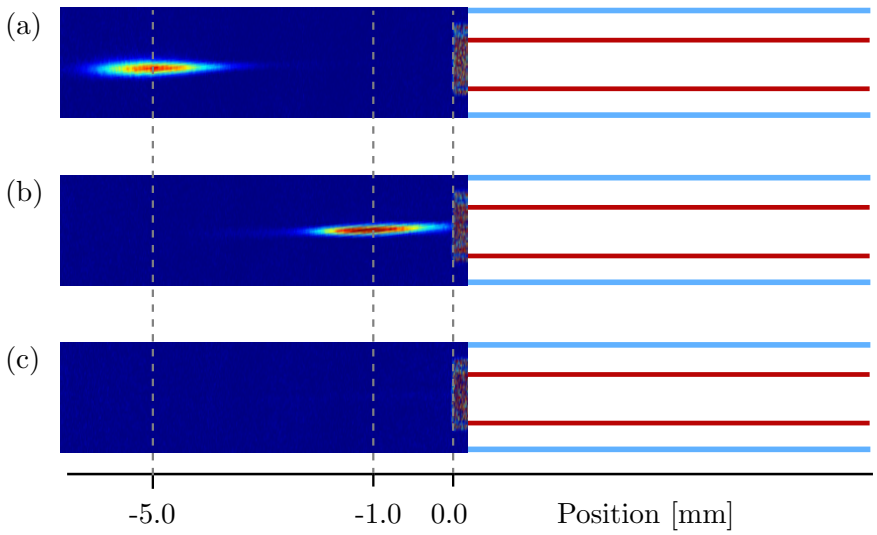

Figure 3.13.: Cold atoms trapped in optical lattice at (a) MOT position, (b) moved to the fiber tip and (c) inside the fiber.

This high degree of control over the atomic position establishes the quasi-one dimensional confinement for cold atoms. The results from the experimental achievement serves as a playground for creating strong light-matter interaction. To further the stability and control over the phase noise present in the two counter propagating laser

beams, we made an effort to detect the phase via interferometry techniques [55]. This detected phase information can be used to feed back the AOMs for a phase-noise free optical lattice.

4. Experimental techniques: control and detection

Experiments in atomic physics typically require high precision and stable timing controls. The stringent requirements are demanded by the time scales associated with the various experimental parameters such as coherence lifetime, atom-loss rate or spin relaxation times, etc. In this chapter, the system for the high precision experimental controls and detection relevant for this project are discussed. The main principle relies on the precision time pattern generation referenced to a single stable clock. This is achieved by using a hardware timed digital solution to control a sequence of signals, eg. laser pulses, ramp trigger, etc. Consequently, additional synchronized triggers are produced to mark and store data only for the interesting time windows. The high speed pulse pattern generator used for this project eventually is integrated with the existing "slow" experiment controller along with the software interface. The main experiment controller is designed in LabVIEW using a commercial controller by ADwin-pro from Jäger Computergesteuerte Messtechnik GmBH which is limited to a time resolution of $10\,\mu s$. Furthermore, creating loops and complex patterns is not that trivial with the existing control.

4.1. Pulse pattern generator

The precision experiments performed in Chapter 5 required high-precision timed control pulses as shown in Figure 4.5. In such experimental control and measurement, time scales ranging from nanoseconds to several seconds are desired. To meet such requirements, hardware timed, stable clock based signal pattern generators and a fast oscilloscope are used. Certain dedicated hardware devices are typically interfaced with a central processing unit (CPU) for control and user access. Although, CPUs run at very high clock speeds and are utilized in such time demanding experiments, they themselves lack the generation of precision timing sequence because the various tasks are processed in a sequential order and thus time repeatability is not guaranteed. Hardware timed devices such as Application Specific ICs (ASICs), Field Programmable Gate Arrays (FPGAs) are the natural choices for such experimental controls. While ASICs are capable of handing and producing signal at frequencies over several GHz, they lack the reconfigurability and therefore the versatility is limited. Moreover, the time-to-implementation in a general application is significantly long and costly which limits its practicality. For the context of the experiment in this thesis, FPGAs are fast enough to produce all the relevant control signals. In this work, a Xilinx FPGA (Spartan-6) [101] based high precision-timed sequence generator is im-

plemented which then is integrated with the main experiment controller hardware to facilitate high speed measurements. In the Figure 4.1 a visual implementation of the FPGA sequence generator is depicted. Here, the sequence pattern data is captured from the user input using a GUI on the computer. The data is pushed via USB port to the FPGA internal memory. Specific USB communication devices are used for this purpose. The treatment of the user data is configured in the FPGA using HDL codes which are presented in the appendix. The IO part of the hardware is interfaced to drive the AOMs, switches and triggers. The sequence pattern is generated in sync with the external trigger input. In this experiment, the trigger is given from the main experiment controller. The precision experiment section is then handled by the FPGA sequence generator.

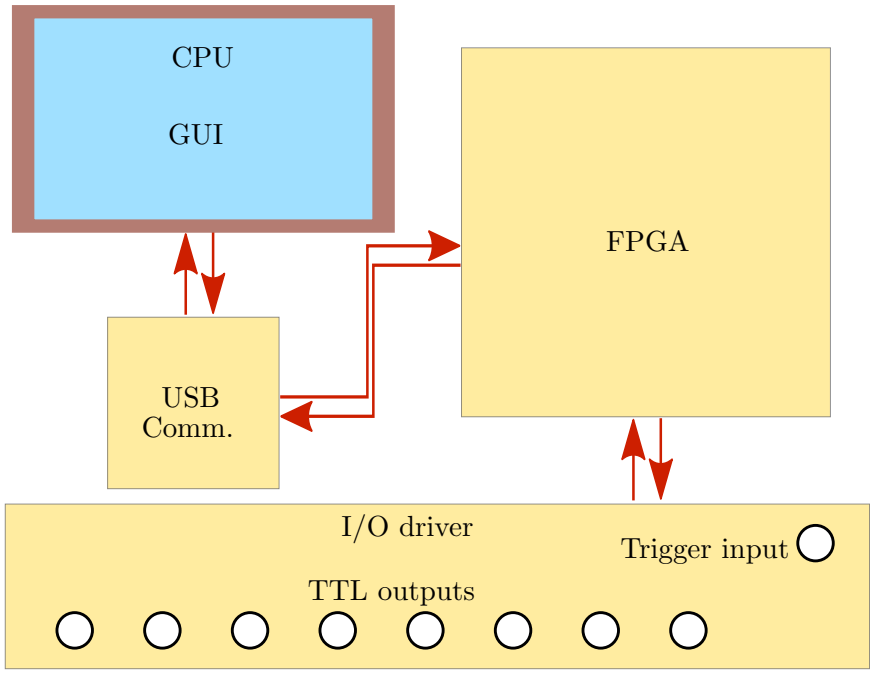

Figure 4.1.: Schematic of working principle of USB-FPGA interface for the pulse generator. Pulse-pattern is stored on the FPGA memory via USB communication. External trigger enables the output on demand.

4.1.1. FPGA

As shown in the Figure 4.2, an FPGA primarily consists of three types of functional components– logic block, IO block and interconnects. The logic block consists of basic logic cells such as flip-flops, selector switches, comparator, etc. whose task is to perform the primitive gate operations. The IO block comprises of transistors and registers for driving and storing the input and output state. This block interfaces with the outside world with various types of signals, such as transistor-transistor logic

(TTL), low voltage differential signal (LVDS), etc for clock or data operation. The two blocks are interlinked with a large number of wires which can be configured to route the signal in a number of ways. Such routing is made possible by the interconnects which make an FPGA a platform for reconfiguration in the field operation. This reconfigurability is what gives an FPGA the main power in the domain of digital electronics. It stands clearly away from microprocessors and microcontrollers in the sense that the logic "wiring" in the later ones are hard burnt making them only suitable for specific applications. Furthermore, even single logic operation undergoes a series of events making them unreliable for time critical applications. In contrast, the functionality of an FPGA can be thought of as real hardware logic units operating all in parallel. Such challenges are met by the interconnect which can be configured to trigger in sync with a single global clock input. On a side note, the clock rate of an FPGA only ranges upto several 100's of MHz which is much smaller than the modern CPU clocks which have surpassed 5 GHz. Nevertheless, the capability of parallel processing provided by an FPGA can not be fulfilled by any CPU as CPUs work on sequential operations. However, the benefits an FPGA enjoys from the primitive logic architecture also poses certain limitations. For instance, any specific application would require reconfiguration of a large number of logic cells in a specific structure. Additional difficulty comes from the actual human readable code as the structure of the code does not strictly follow a sequential manner due to the feasibility of parallel operations.

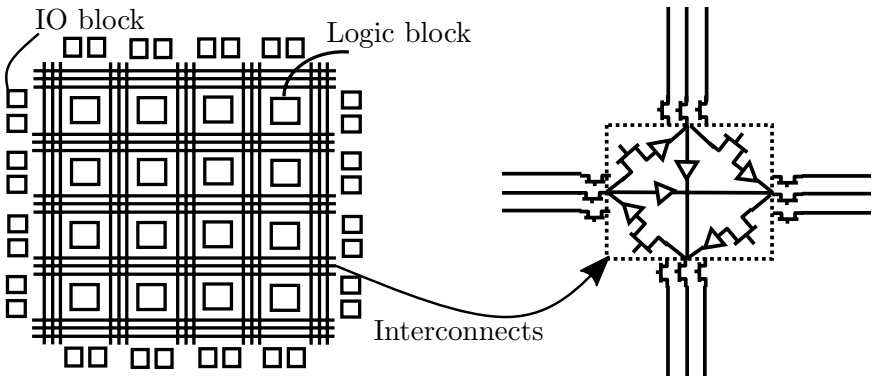

Figure 4.2.: Internal functioning of FPGA.

The clock line of an FPGA is distributed internally throughout the IC, i.e. to different logic cells with equal propagation time delays at each gate. Using static random access memory (SRAM) based memories, different interconnects and logic cells are configured based on a given application. An SRAM is essentially a large array of flip-flops which makes it significantly fast in order to perform single clock operation. The programming software mainly translates the human written codes into a binary file which is stored inside the FPGA chip. The language is called hardware description language (HDL) since it configures the various logic cells, flip-flops, SRAM and the associated wirings. For this project the task included in the HDL code is to establish a communication

protocol inside the FPGA which can read data transferred over USB-Serial device which is discussed in the next section. The data is then transferred to the internal memory, block RAM (BRAM) of the FPGA which can be read on demand. The configuration further defines the different IO pins for input or output as it is required for clock, trigger or output channels. One limitation lies with the FPGAs as the internal memory is all based on SRAM type which looses its state once the device is powered off. This means, the device needs to be reconfigured every time it boots. For this purpose a flash memory also comes soldered on the development board where the configuration binary data is saved and reloaded. Once configured and the time-pattern data is loaded from the computer, the given pulse pattern can be generated on the multiple pins of the FPGA. The pulse generation events are triggered with an external event to maintain the synchronization with the main experiment.

4.1.2. USB-communication

USB being one of the most common ports in the modern computers offers an easy and universal solution for data transfer between a host and a client. For this project, a very simple USB UART protocol was used. As the need to the data was not too large, it worked mostly fluently for our purposes with a cable length larger than 15 meters.
UART is an acronym for Universal Asynchronous Receive and Transmission. The data is sent from the experiment control PC to the FPGA board with a fixed rated, also know as baudrate or bits per second. In order to set a proper communication, the baudrate has to be known in advance as this kind of communication does not carry any additional clock. The data is broken and sent in packets, with each packet carrying 10 bits of those 8 are actually used as data, while the other 2 bits are overhead that is needed for the communication protocol. As shown in Figure 4.3, the idle state of signal on the Rx/Tx is high. Which after detecting the negative fall starts a trigger to sample data after predefined intervals. In this case, the data is sampled in the middle to avoid ambiguity. A dedicated device is used for converting USB to serial type data. The serial data is then interpreted and saved in the FPGA Memory which is discussed in the next chapter.

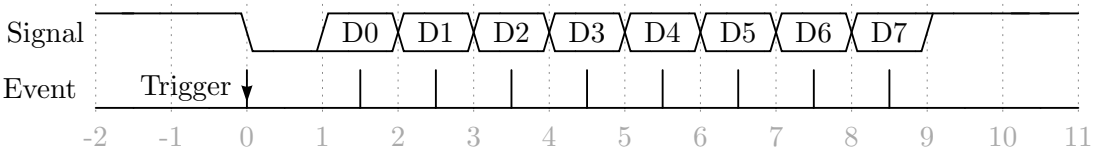

Figure 4.3.: Time diagram of UART communication protocol. Idle state of signal is high which is lowered at the beginning of communication. Data bits are sampled after a predetermined time period.

4.1.3. Control interface

The data received from the PC is stored in the block RAM or BRAM of the FPGA. The FPGA outputs the data on the digital pinouts once it gets a trigger on the preconfigured input pin. The digital signal pattern and time information is stored in multiple words with each word length set to 108 bits. The first 48 bits controls the registers attached to the output pins, while the remaining 64 bits are used for interpreting time information. The way it is implemented in the FPGA is that for a given step, the 48 digital pins are toggled to states defined by the 48 bit word. This output configuration waits for a time defined by the 64 bit word with each clock ticking at 10 ns. The FPGA is further configured to create loops of certain part of the time-steps to create more complex pulse patterns.
A typical GUI software interface is shown in the Figure 4.4. In this example interface, a 8 bit pattern is generated with time resolution of 10 ns. Multiple loops of these patterns are realized by placing values on the right side, eg. *num1* and *num2*. The loops are also independent to each other, meaning they can be operated in sequential order or one loop inside other. Such flexibilities offer a number of possible output pulse pattern which are extremely important for control and measurements. The GUI program is written in Python using Tkinter library which is included in the Appendix.

4.1.4. Pulse generation and testing

In this section, the performance of the home-built pattern generator is presented. The device is capable of generating pulses as short as 10 ns and multiples of it for a duration up to several weeks which is way beyond one would need for the applications in cold atom experiments. In the final stage, buffer line driver ICs were implemented for both, protection and high current driving capabilities. A measured pulse pattern is shown at high sampling rate in Figure 4.5. The different digital signals drive the AOMs for the two spectroscopy signals, namely probe and control lasers and the two dipole trapping lasers.
In the shown trace, the two dipole trap lasers are turned off when the detection is made. In order to avoid the overlap between the detection, additional delays are padded to the both sides of the probe/control AOM signals to account for the actual delays in AOM driving signals. The rise time and the fall time ($10\% \leftrightarrow 90\%$) of the signals (shown only for the blue trace) are well below 10 ns. The exact timings as sent from the PC are shown in the Table 4.1. All the high speed measurements in the project range over several 100's of ns. The ringing effects can be seen which is a trade-off with the rise-time. However for our application, use of a proper termination solves the issues which was also confirmed by the actual laser pulse timings.
In conclusion, a simple and easy solution is implemented for a relatively high precision and time demanding performance. The device is implemented in the experiment with a trigger input, afterwards, the device takes control of both the dipole trap lasers and probe and control beams along with all the trigger outputs for the oscilloscope for data acquisition.

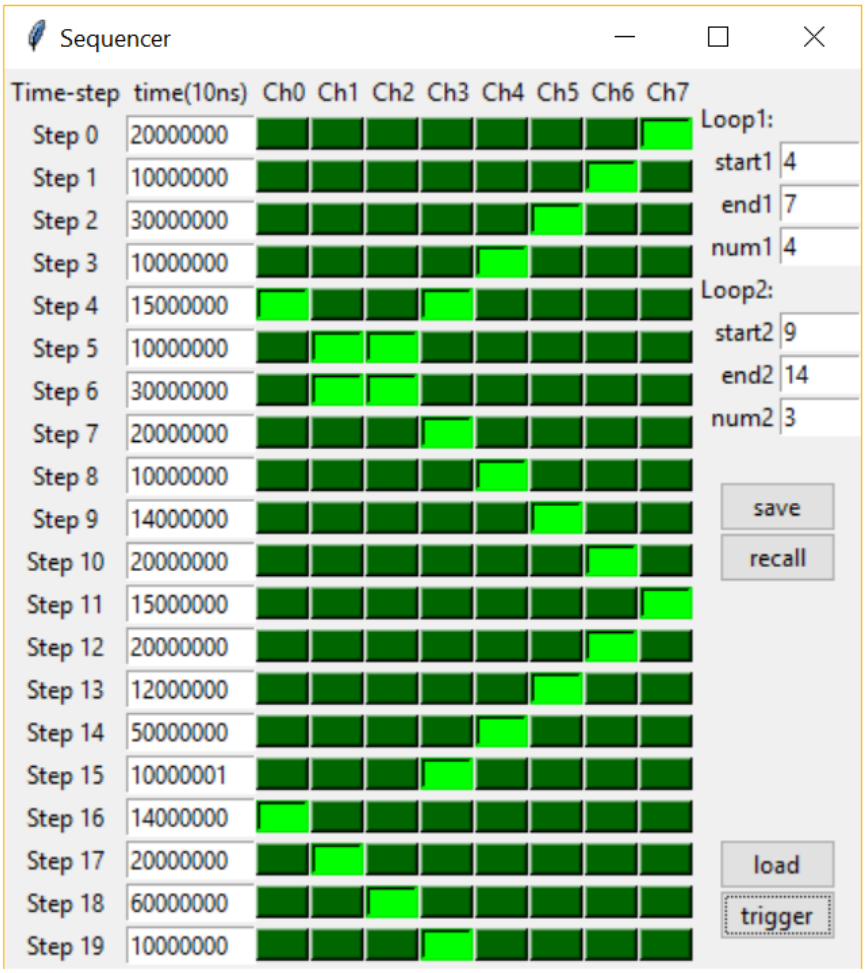

Figure 4.4.: Control software interface for FPGA pulse generator. The word pattern is stored using a GUI interface. Output pattern is generated via either a software or an external trigger.

	Set timings	Measured timings
Delay 1	20 ns	26.5 ns
Pulse Time	50 ns	47.5 ns
Delay 2	20 ns	22.5 ns

Table 4.1.: Time diagram of signals for controlling various AOMs.

4.2. Detection and data processing

Pulsed signals are stored on high-speed oscilloscope (Lecroy WaveRunner 625Zi) for further analysis. The scope is capable of storing signals in segmented memory configuration to reduce the total data size while only storing the useful events. Data files

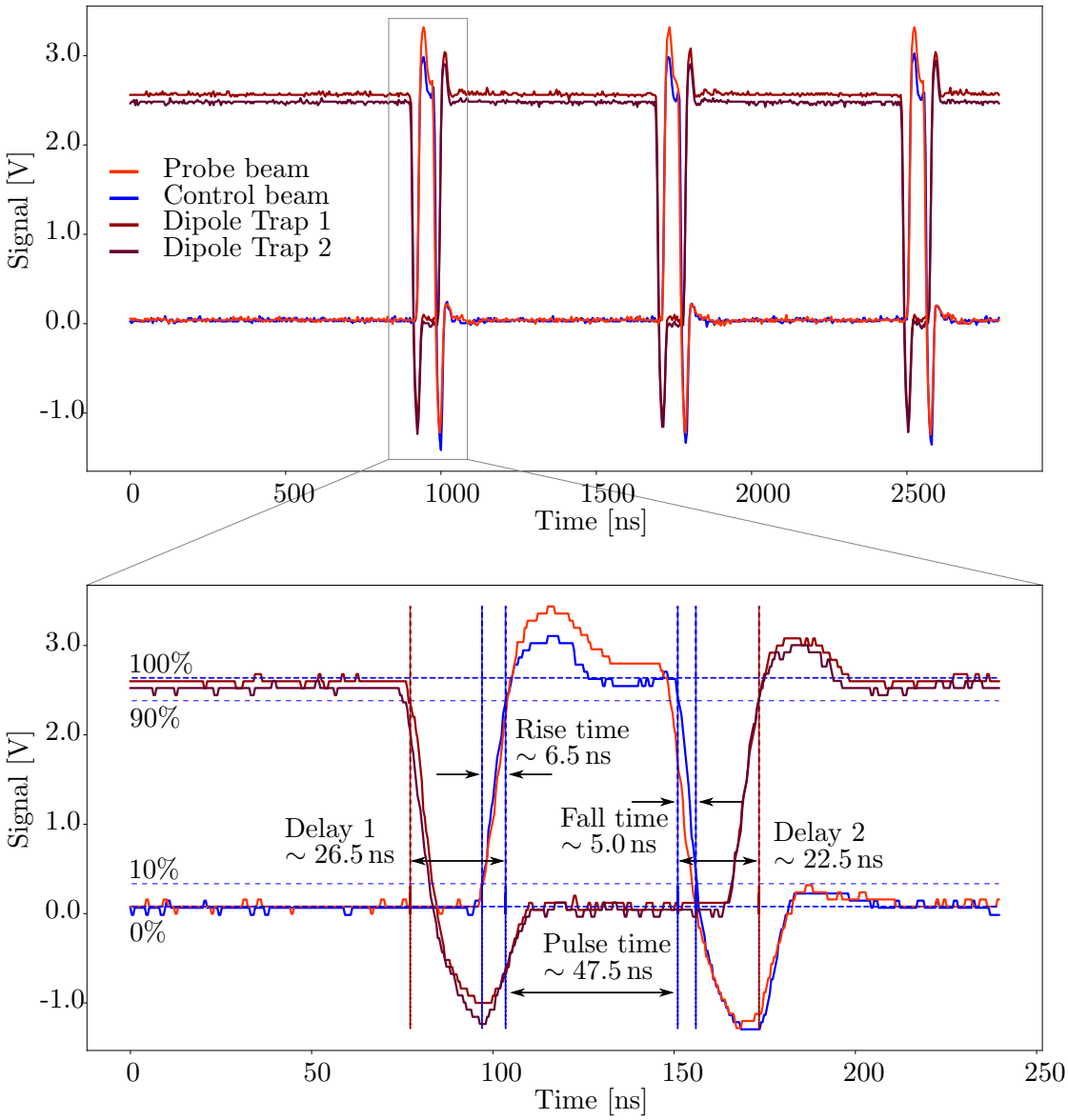

Figure 4.5.: Pulse durations for different channels. Delays were added between the probe/control and the lattices switch signals.

are stored in the hard drive which is shared with a local PC. The data is loaded in MATLAB or Python for further analysis. A series of traces are taken which includes signals with atoms, without atoms and without probe beam to remove background noise and offsets.
To match the right timings, a trigger pulse is generated from the pulse generator to synchronize the detected probe beam pulses. Timing offsets are matched by observing the signal on the scope which appears due to the delays in the different electronic stages

for the probe beam AOM.

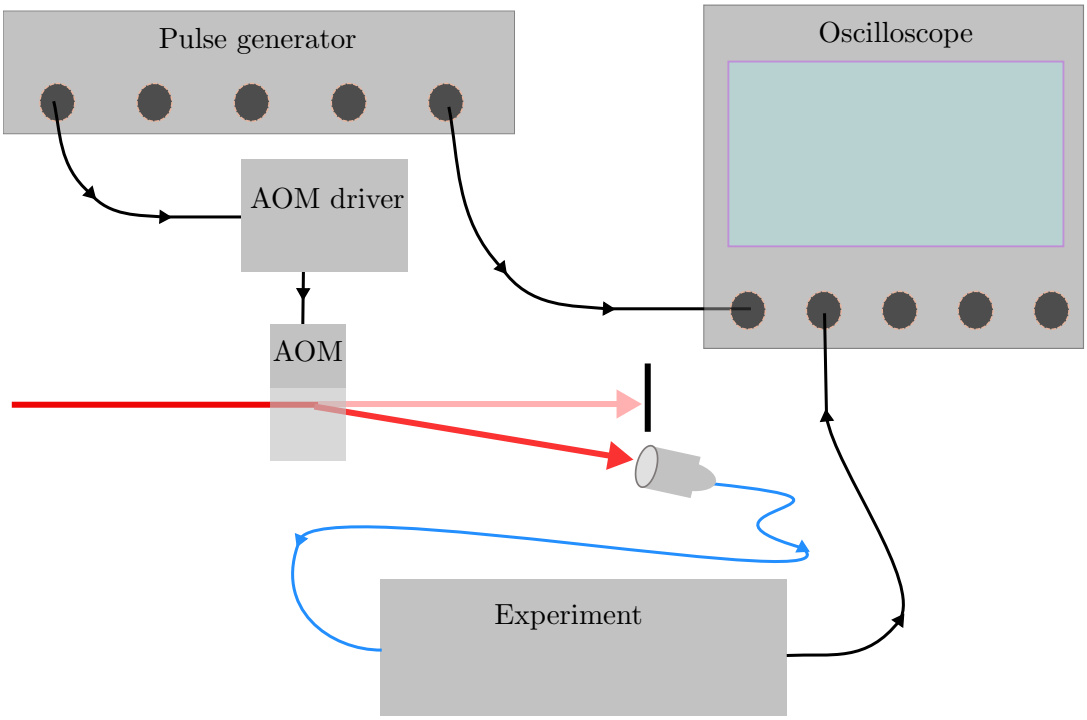

Figure 4.6.: General detection setup with trigger and AOMs signals driving the experiment and detected on fast Oscilloscope.

4.3. Laser stabilization

One of the most crucial requirements of a cold-atom lab is a source of a highly stable and tuneable laser beam. Such stringent requirement is needed for a wide range of applications such as laser cooling, manipulation of atomic states, spectroscopy, etc. There are different techniques developed to stabilize the laser frequency. In this work, we used reference line from atomic spectra to stabilize the laser to different states. To precisely modulate and control the frequency, we used AOMs. In this work, frequencies of the several lasers were stabilized using frequency modulation (FM) spectroscopy technique. In this technique, the phase of a laser source is modulated which results in generation of sidebands. This beam is now scanned near the atomic transition and when demodulated using the Pound-Drever-Hall detection technique [11], it generates error signal which is fed back to the laser driver to stabilize the laser frequency.

4.3.1. Laser locking

Lasers are stabilized and locked to the relevant 2-level atomic transition line for laser cooling and detection. For our experiment, we use ^{87}Rb atomic vapour cell for sta-

bilization. A near-resonant weak laser beam is passed through the cell which then is probed on to a photo detection. By scanning the laser detuning, the absorption signals are obtained which corresponds to multiple lines consisting of fine and hyperfine lines. However, a well known reason discussed earlier in Chapter 3, Doppler shifts due to atomic motion gives rise to significant broadening in the line shapes. Typically such line shapes are several 100's MHz broad which makes it difficult to address the hyperfine lines as they are separated by similar values. To circumvent these issues, Doppler-free saturation absorption spectroscopy is set up.

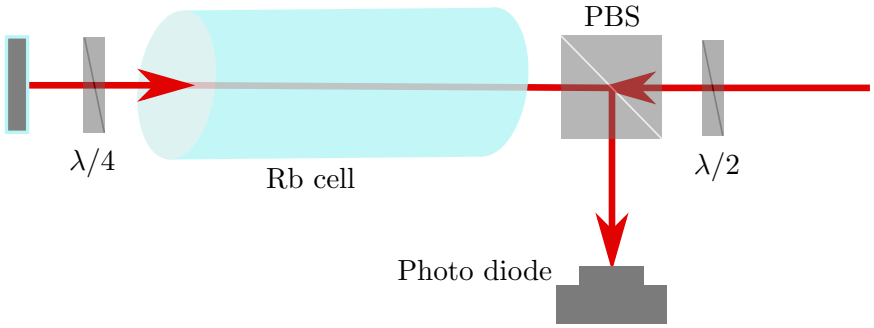

Figure 4.7.: Saturation absorption spectroscopy for laser locking.

To obtain a Doppler free atomic, some part of the scanning laser beam is split up and sent from a counter propagating direction inside the Rb vapour cell. Alternatively, a similar result can be achieved by retro-reflecting the probe beam and separating it using a $\lambda/4$ waveplate and a PBS as shown in the Figure 4.7. This results in velocity independent detection of atomic transition lines. Additionally, it also shows what are known as cross over lines which are even stronger than the constituent transition lines as shown in the Figure 4.8.
Using the Pound-Drever-Hall detection scheme, the laser is stabilized to either of the transition lines or the cross-overs. By adjusting the laser input frequency, by an AOM, the final laser frequency is precisely controlled. Although this method has advantage of keeping the power constant while scanning the frequency, this lacks the speed and control at which the laser is modulated. Furthermore, it also lacks power controls. An additional AOM is placed after the stabilization stage to allow for power adjustment along with the frequency control. This method offers very high speed power and frequency adjustment of the laser in the time scales of 100's of ns only.

4.3.2. EIT locking

Laser for addressing Rydberg states are stabilized using EIT-locking where error signal is generated by using a control laser in addition to the probe beam. Some details of which are also explained in this bachelor thesis [94]. In this scheme, a weak probe laser stabilized to the $F = 2 \rightarrow F' = 3$, using the previous method, is sent through a vapour cell. From the counter propagating direction, the control beam near a given Rydberg state transition line is scanned. As the laser scans, it creates a transmission

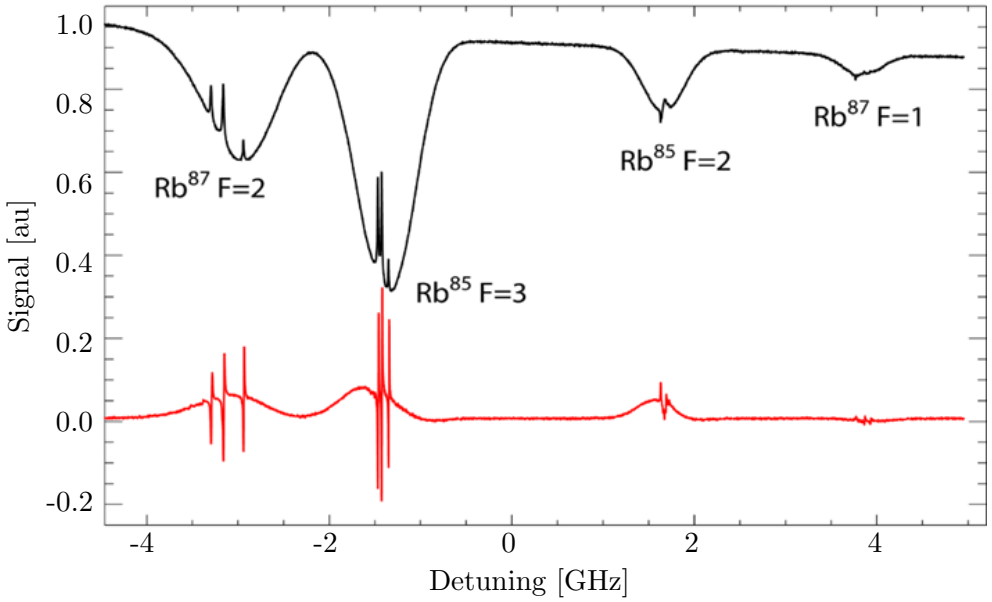

Figure 4.8.: Doppler free lines and error signal for laser locking [1].

signal, via the process already discussed, EIT. To stabilize the control laser frequency, again, an error signal is generated. This is achieved by frequency modulating the probe laser and demodulating using Pound-Drever-Hall technique. The error signal is now fed back to the control laser via a PID lock box. With a right selection of the parameters, the laser locking is engaged which then stabilized to the error signal. The

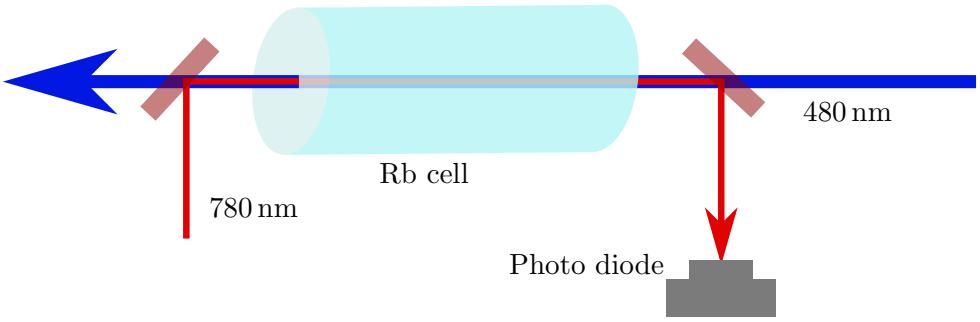

Figure 4.9.: Doppler free Rydberg EIT locking scheme.

detuning of the control laser is controlled by either changing the reference probe laser frequency or by using an AOM in the output of the control laser. As discussed earlier, there are trade-offs between the two methods and what is implemented depends on the particular requirements. However, it is important to note here that since the two laser wavelengths are not equal so the Doppler cancellation is completely achieved hence a clear understanding is required. Two-photon EIT signals are under off-resonant probe

frequency require the understanding of the Doppler shifted detunings,

$$\delta_c = -k_c v, \tag{4.1}$$
$$\delta_p = k_p v, \tag{4.2}$$

where, at a given velocity of an atom, the control and probe detunings are δ_c and δ_p. For the thermal cloud, there is always abundance of atoms at velocities near zero. This is important to take it under consideration as the EIT lines are extremely two-photon detuning dependent. In that, the lines would be strong only if the two detunings are matched and moreover, the probe laser is on resonance. For a given probe detuning Δ_p, a class atoms with velocity, v such that $\Delta_p + \delta_p = 0$. This results in

$$v = -\Delta_p / k_p. \tag{4.3}$$

Now, the same atoms would see the control laser at a detuning

$$\Delta_c = -k_c(-\Delta_p/k_p), \tag{4.4}$$
$$\Delta_c = -\Delta_p \lambda_p / \lambda_c. \tag{4.5}$$

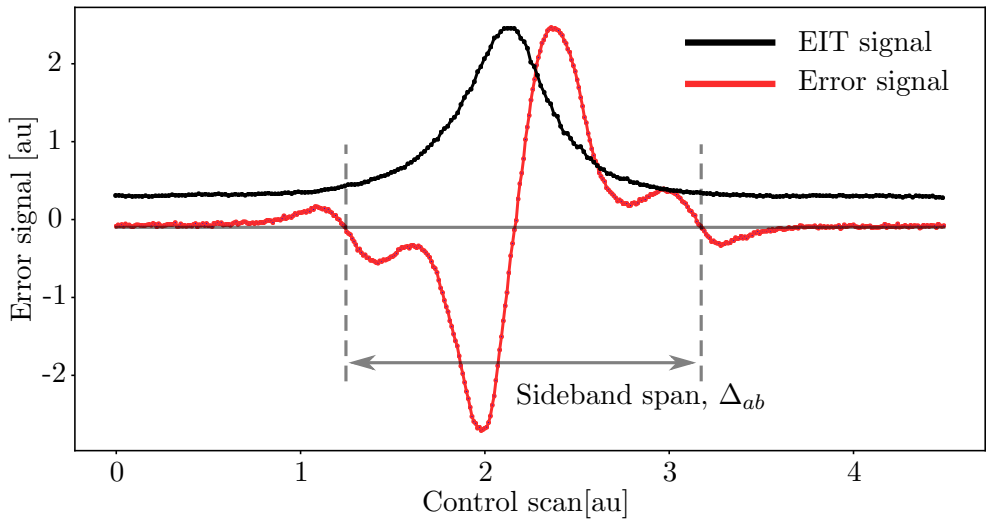

Figure 4.10.: Doppler free EIT locking scheme.

Using the sideband span, Δ_{sb} the axis is calibrated. The Δ_{sb} is obtained from the EOM frequency of driven by a function generator. In this experiment, the value of $\Delta_{sb} = 10.4\,\text{MHz}$. The observed span between the two cross points is

$$\Delta_{ab} = 2\Delta_{sb}\frac{\lambda_p}{\lambda_c}, \tag{4.6}$$
$$\Delta_{ab} = 2 \times 10.4 \times \frac{780}{480} = 33.8\,MHz \tag{4.7}$$

In simple words, the control laser detuning is set to the ratio of the wavelength of the two lasers times the detuning of the probe laser. In particular, with our laser configuration, the control frequency is adjusted by 1.625 times the detuning of the probe. This factor was taken into consideration in all the experiments performed and analyzed.
In this chapter the details of some of the main parts of the experiment control is presented. The existing commercial experiment controller is flexible enough for preparation of cold atoms, however, it lacks generation of fast pulses. Experiments suited for manipulation of atomic states, such as storage and retrieval of quantum information require controlled light pulses on a sub-microsecond time scale. An FPGA based solution presented in this chapter is integrated to the main control system allows for a time control of 10's of ns which is further implemented for a detection and measurements.

5. Rydberg excitation inside hollow core fibers

As has been discussed in the introduction and Chapter 3, atoms in the Rydberg states have drawn considerable attraction in the recent times. On the one hand long-range interactions allow for a tuneable control via the Rydberg states while on the other hand longer lifetimes offer a range of advantages for the practical usage. Combined with the quasi-one dimensional systems demonstrated by the hollow-core fiber interface, atoms excited to Rydberg states should propose another novel platform for quantum information processing or simulations. By tuning the blockade radius excitations the dimensionality can be tuned which can be used to modify the photon statistics.
However, the task becomes challenging particularly due to the closeness of the fiber wall surface near the atomic ensemble. Such interfaces have been known to show high electric fields which lead to shifts and broadening hence reducing the contrast of the EIT signals [20]. With our approach, the first part of this chapter discusses the first Rydberg EIT signals with the cold atoms loaded inside the fiber. In the later part the characterization and measurements with another setup where room-temperature atoms are loaded inside hollow-core fiber are presented. The idea is to understand the influence of fiber inner core structures and coating of different materials.

5.1. Rydberg EIT with cold atoms

The challenging goal is to realize a controllable system where atoms excited to Rydberg states form spatial correlation due to Rydberg blockade effects. This type of system has potential applications in understanding many-body photonic states, storage of quantum information and repeater. A handful of research has been performed in this direction [90, 79, 37, 92]. However, this work differs from others by two means – first, the extended long atom-light interface enhances the interaction strength and second, again due to the extended system, the accommodation of multiple excitations along the ensemble length would allow for interesting correlations. The photon storage and retrieval experiments have significant benefit from the cold atomic ensemble. This is due to the frozen atomic movements which reduces the decoherence processes as well as allow for longer interrogation times.

One of the ways to go about exciting atoms to Rydberg states is via EIT processes where two photons of addressing atomic transition in ladder scheme are projected to atomic sample. In this case, the EIT measurements are performed with the cold atoms transported inside the hollow-core fiber. The task itself is challenging due to

the presence of the atoms very close to silica surface. On such dielectric materials, charges are prone to attach and have known to create significant amount of field. These fields are highly undesirable as they produce lineshifts and broadenings in addition to facilitating ionization processes. In the following parts the experimental procedure and results are presented. A big part of the experiment is performed with my colleagues which is also presented in this thesis [59].

5.1.1. Experiment

The experimental sketch is shown in Figure 5.1. In the setup, a hollow-core fiber is placed horizontally inside the main UHV chamber. Cold atoms of ^{87}Rb is trapped in MOT in front of the fiber at a distance of about 5 mm. The guiding principle is discussed in the Chapter 3 where a pair of counter-propagating dipole trap beams are mode matched through the HC fiber. The control over the position of the atomic cloud has been demonstrated as shown in Figure 5.1. To address the Rydberg states, a probe beam at 780 nm and a control beam at 480 nm are overlapped in the counter propagating configuration using two photon processes as discussed in Chapter 2. These beams are also mode matched with the dipole beams in order to assure that the maximal coupling with atomic ensemble is achieved. As discussed earlier in the Chapter 3 the guiding properties for a range of wavelengths allow for such good overlaps. Using dichroic mirrors the probe beam is aligned and overlapped through the fiber. Consequently, the probe beam is deflected off and sent to a PMT for detection.

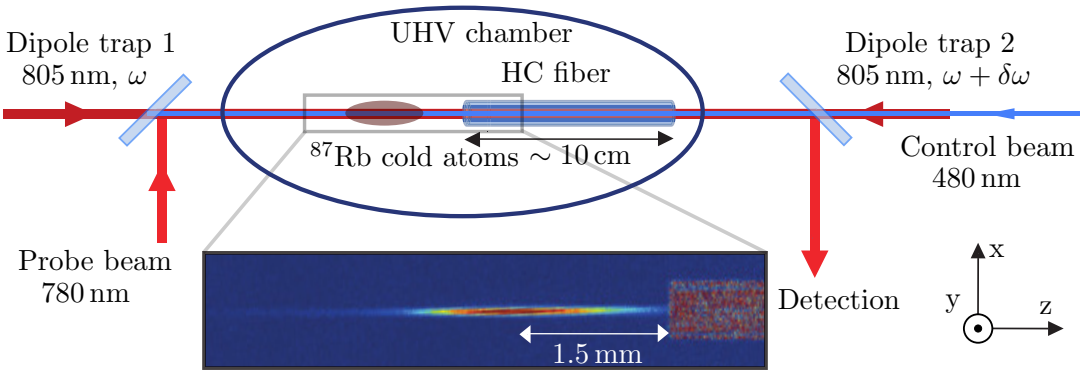

Figure 5.1.: Experiment setup for cold atoms Rydberg excitations. Inset shows a real image of atoms reaching the HC fiber.

5.1.2. Time resolved detection

The experimental sequence consists of loading the MOT, transferring the atoms to the optical lattice, transporting them to a desired position along the fiber length and finally detection. This section mainly focuses on the details of detection schemes. Broadly, the detection process involves a two photon excitation while avoiding the

lightshifts produced by the trapping lasers. Using the home built FPGA pulse pattern generator, special patterns are generated which control different AOMs to perform EIT experiment. Moreover, these pulsed detection scheme allows for detection of EIT signal in time domain which is helpful to understand the coherence and the loss rates.

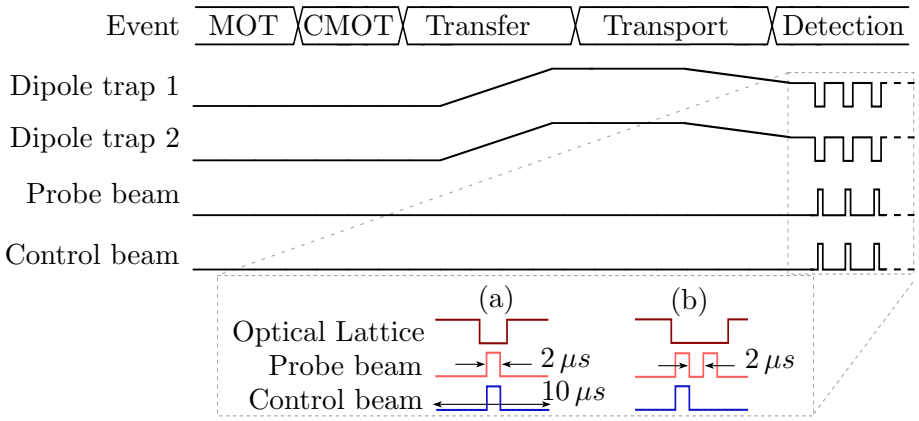

Figure 5.2.: Experiment time sequence. In the inset, dipole beams are turned off when the probe and control beams are sent. Two different schemes used to verify Rydberg EIT processes.

As the atoms are transported inside the fiber, the confining trapping potential from the optical lattice keeps the atoms away from the fiber wall. This is also important for spectroscopic reasons as the cold atomic ensemble can heat up due to the collisions with the fiber wall. For such a narrow core size, the atoms, as they are released can hit the fiber and will eventually be lost. Such dynamics can occur at the time scales on the order of 500 μs. In order to detect these atoms while reducing noise level, repeated measurements are made. The ac Stark effect due to the dipole trapping beam can cause inhomogeneous line shift, therefore while probing, dipole beams have to be turned off. Such a sequence follows a repeated on and off pattern as shown in the Figure 5.2(a). When the probe pulses are turned on, simultaneously a set of trigger signals is sent to a fast oscilloscope in order to synchronize the signal from the PMT which captures the transmitting probe beam. Between each probe pulses there is a relatively large settling time when the trapping potential is re-initiated. The oscilloscope is set to run in a segmented memory mode in which it only captures the signal around the time window of the probe beam. This way the unnecessary amount of data is avoided, i.e. when the probe beam is not present. By altering the detuning of the probe laser a complete EIT profile can be captured. Moreover, the temporal information associated with the EIT process and loss are also recorded. A comparison between the EIT signal outside and inside the fiber is shown in the Figure 5.3. Here, the x-axis represents the probe detuning and the y-axis demonstrates the temporal behaviour of the EIT profile.

A cross section at pulse number 100 is plotted in the Figure 5.4 for the two data sets

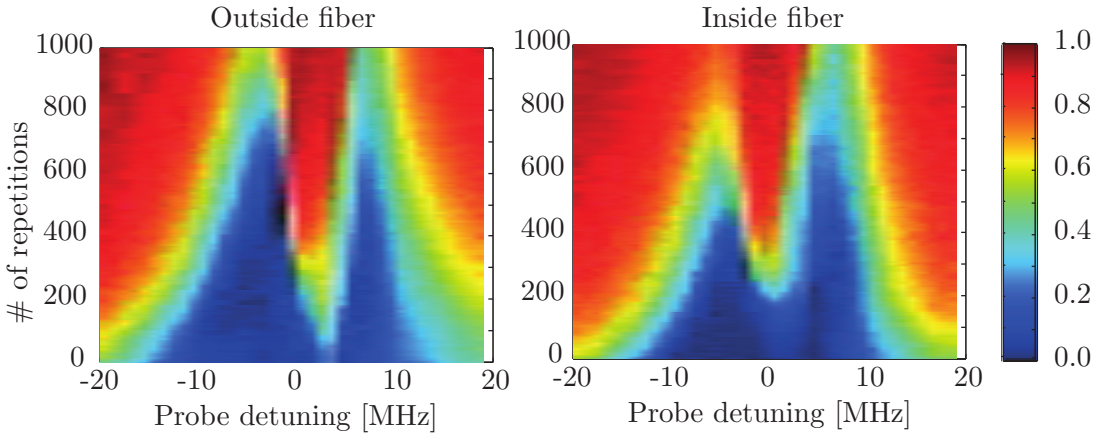

Figure 5.3.: Full time resolved Rydberg EIT signal for inside and outside the fiber.

to obtain the EIT behaviour. From the fit, it can clearly be seen that there is about 60% and 40% of transmission for the signal outside and inside the fiber. Besides the lineshift, it is important to note that the EIT fits are particularly not good. The reasons and a better model to explain this behaviour are presented in the Chapter 6.

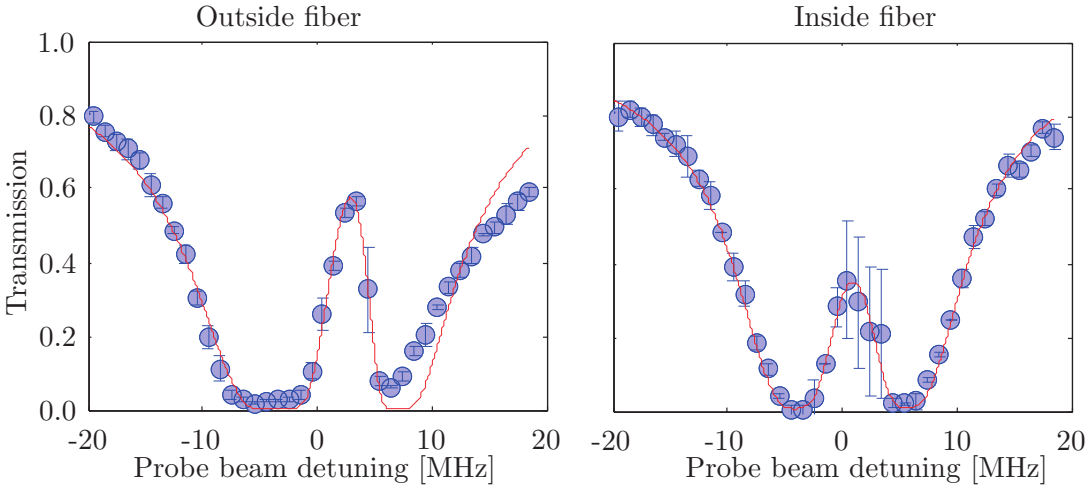

Figure 5.4.: Cross section at pulse number 100 Rydberg EIT signal for inside and outside the fiber.

To verify the coherence processes and hence actual EIT signal, scheme using double probe pulses as shown in Figure 5.2(b) is used. In this case, the first pulse, where the control beam is also enabled should show typical EIT feature while the second pulse should monitor the optical density. In order to understand if the signals are not affected by other destructive mechanism such as hole-burning, the second pulse, i.e. the OD signal is utilized. In particular, to illustrate the loss mechanism, the OD signal is subtracted from the EIT signal. In the Figure 5.5, the time resolved

subtracted transmission signals are shown for outside and inside the fiber. The positive values, i.e. the red zone shows the actual transmission process governed by the EIT mechanism. The negative values shown in the blue zone are due to the off-resonant EIT where dispersion can cause a loss of transmission.

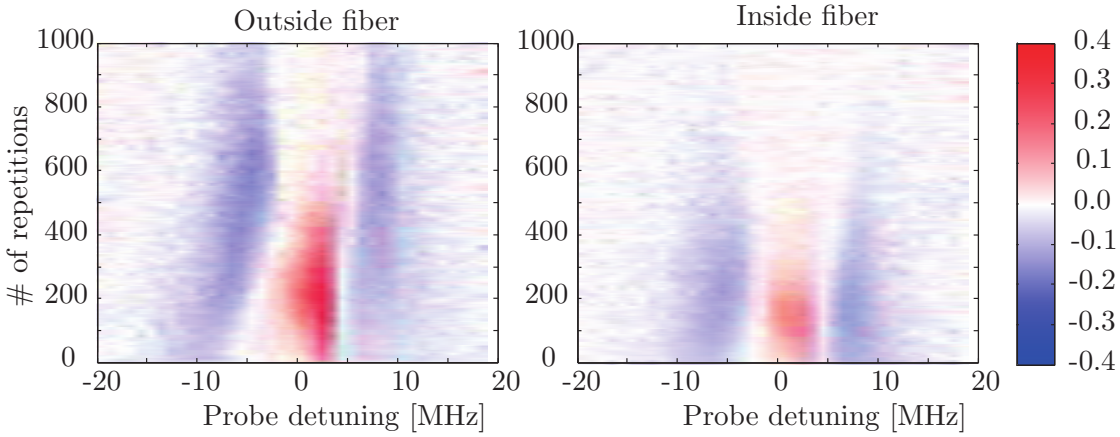

Figure 5.5.: Difference of EIT and OD signals for outside and inside the HC fiber.

The EIT and OD signals directly measured using double pulse technique are plotted for different pulse numbers in the Figure 5.6. As is evident that initially, the EIT pulses are showing clear distinction from the OD pulses which means that the conditions required for EIT are met. At the later time, the OD signals and EIT signals merge together, indicating hole-burning effects as result of atom loss or certain decoherence processes. These results are also clear form the EIT-OD difference plots in Figure 5.5.

As hinted from the previous results where control laser is kept fixed and the probe laser laser detuning is scanned, the shift in the Rydberg line results in an off-resonant EIT process. A correction in the control laser detuning needs to be made in order the meet the on-resonant condition. An alternate approach is to scan the control laser while keeping the probe detuning on-resonance. In this configuration, continuous detection of Rydberg EIT signals are made. For this scheme, the trapping beams were switched off first as shown in the Figure 5.7.
A weak probe beam is continuously sent through the expanding atoms which is detected on the PMT. To induce the EIT process, the control beam is flashed with a repeated time interval. In the presence of the control beam, the transmission window opens up which is visualized in the Figure 5.8. Here, the signals from the outside and the inside of the fibers are displayed. For comparison, separately measured continuous absorption traces are also plotted which have similar decay time scale. Eventually, the ensemble becomes completely transparent for a longer time due to all the atoms disperse from the core region inside the fiber.
To further confirm the transmission and analyze the spectral features, the control beam is scanned near the resonance frequency. Clearly, a peak shown in the spectrum

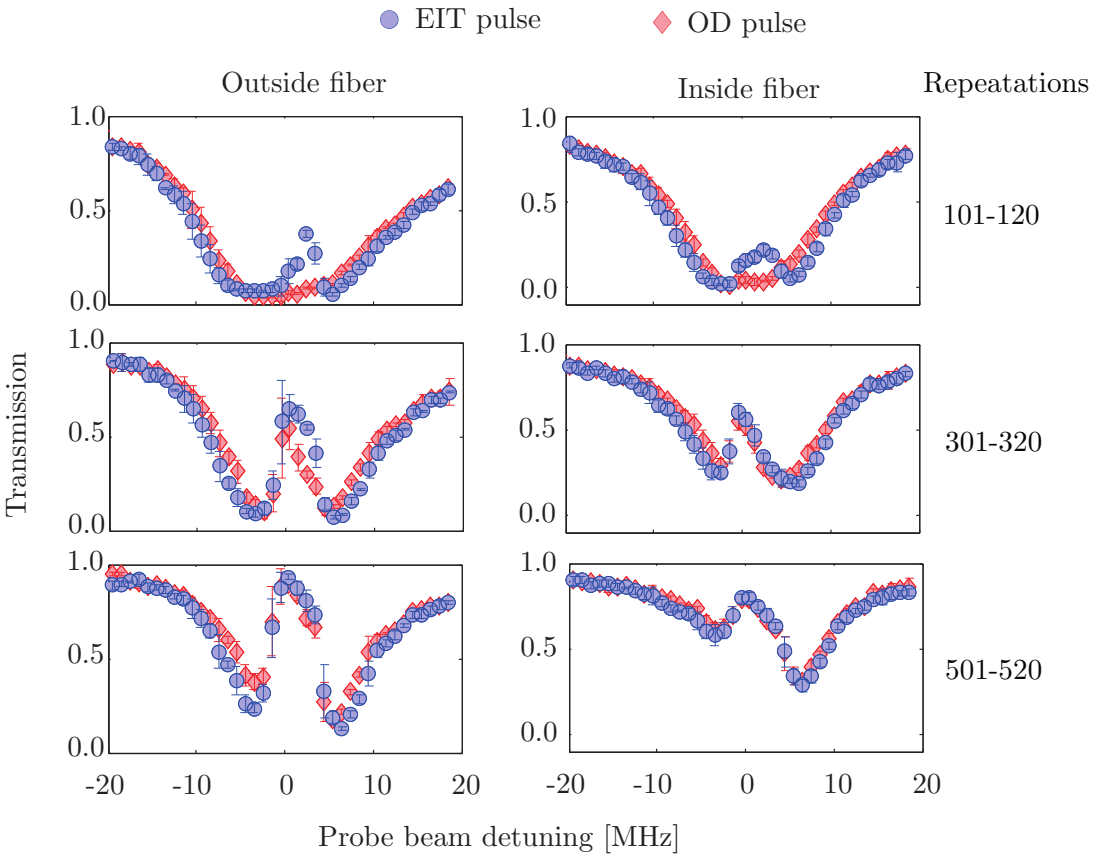

Figure 5.6.: OD and EIT signals at different release time.

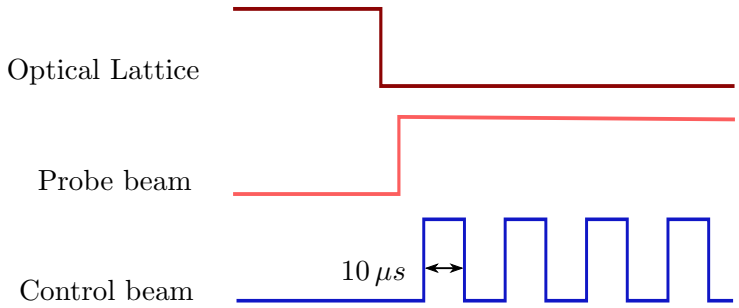

Figure 5.7.: Continuous detection scheme: Probe beam turned on shortly after switching off the optical lattice. The control beam is periodically pulsed.

in the Figure 5.9 confirms the process associated with EIT.
Additional effects of probe power is studied in order to avoid unwanted effects such as heating of atoms or decoherence in the spectral feature. In this case, for the probe beam with 4 nW and 400 pW powers are used while keeping all the other parameters fixed. At these power levels the beams correspond to intensity of $0.25I_{sat}$ and $0.025I_{sat}$

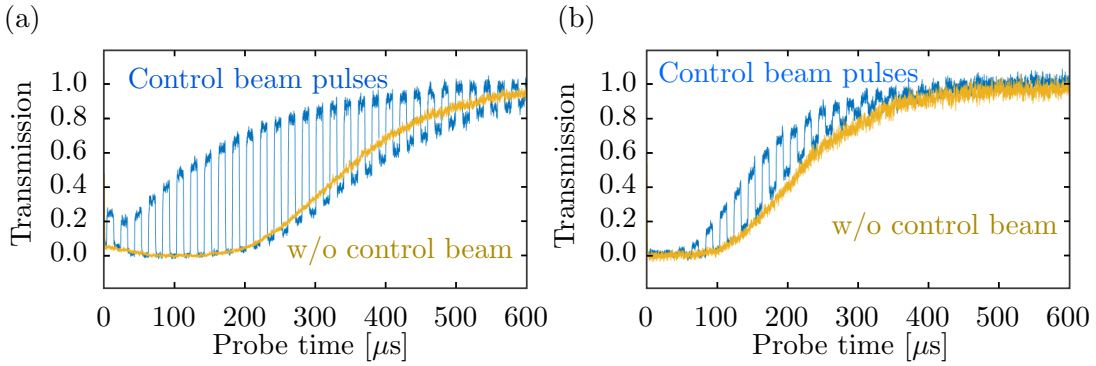

Figure 5.8.: EIT signals: Outside the fiber (a) and inside the fiber (b). Resonant probe beam passes through atomic ensemble and is detected on the PMT. Periodic pulses of resonant control beam induce transmission.

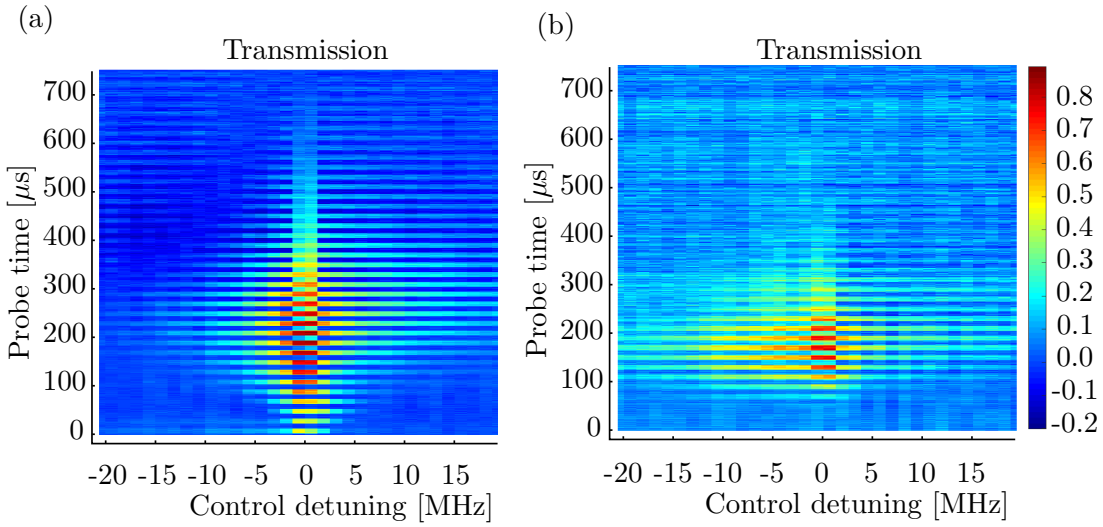

Figure 5.9.: EIT signals: Outside the fiber (a) and inside the fiber (b). Probe beam set on resonance while the control laser is pulsed for different detunings.

where I_{sat} is saturation intensity associated with the probe transition. The measured spectral features are plotted in the Figure 5.10. Note that the data is modified by subtracting the probe transmission from the EIT part, i.e. when the control laser is powered on. It is evident that the on-resonant process undergoes through a rapid change in the transmission. This can be attributed to the loss of atoms from the region of interest. As it was discussed in the Chapter 2, in the case with a Rydberg EIT process, the steady state population of the atoms in the Rydberg state scales with the probe Rabi frequency. Therefore, for the higher probe powers the number of atoms going to Rydberg state would be higher. Due to the relatively short lifetime, a decay channel opens up resulting in loss of coherence. The rapidly increasing transmission at resonance can be attributed to this effect which is also known as spectral hole burning.

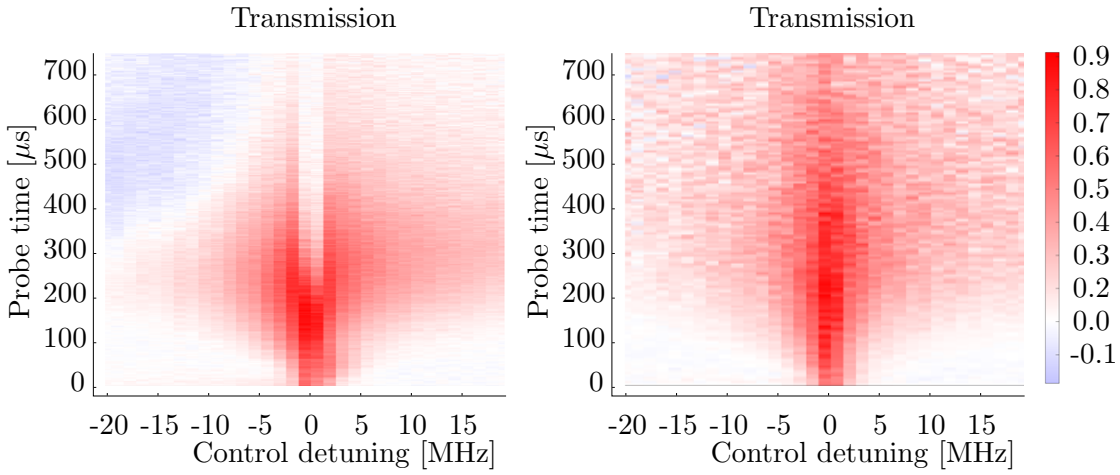

Figure 5.10.: Background subtracted EIT signals for two different probe intensities (a) $0.25I_{sat}$ and (b) $0.025I_{sat}$. Measurements are taken for the atoms outside the fiber. The negative value is due to the imbalance in the subtraction.

It is further important to study the temporal behaviour of the built up of the EIT window over time. This is to understand if the initial probe and control pulses affect the later measurements by any means. To investigate these properties, the control beam is switched on at a set of different delays while leaving all the other parameters fixed. The measurements results shown in the Figure 5.11 suggest that the rise in the transmission signal at later time has no cumulative effect of the control beam. There the increase in transmission at later time can be attributed to the reduced density of the atoms which is a result of thermal diffusion since the trapping field is kept off in this time duration. The same argument holds true for the increase in the observed linewidth.

5.1.3. Stark shift and electric field inside fiber

On the one hand, the high sensitivity to electric fields brings the Rydberg physics to an interesting domain by exploring long range interactions while on the other hand presence of even weak stray electric field can cause undesirable shifts and broadening in EIT lines which could result in decoherence. In the presence of an external electric field, $\mathcal{E}$ the Stark shift is calculated by the Equation 2.61.
In this experiment, atoms guided inside the fiber are exposed to fiber surfaces in a very close vicinity. Neutral atoms or ions sitting at the fiber surface can produce significantly large electric field which is capable of shifting the Rydberg EIT lines. This was hinted in the previous measurements by observing the shift as the atoms are taken inside. To explore the nature and the cause of the shift the measurements are made for atoms inside and outside the fiber for different Rydberg states. The Figure 5.12 shows such EIT signals for two Rydberg states outside and inside the fiber. Here, about 3 MHz and 7 MHz of shifts can be observed for the two Rydberg

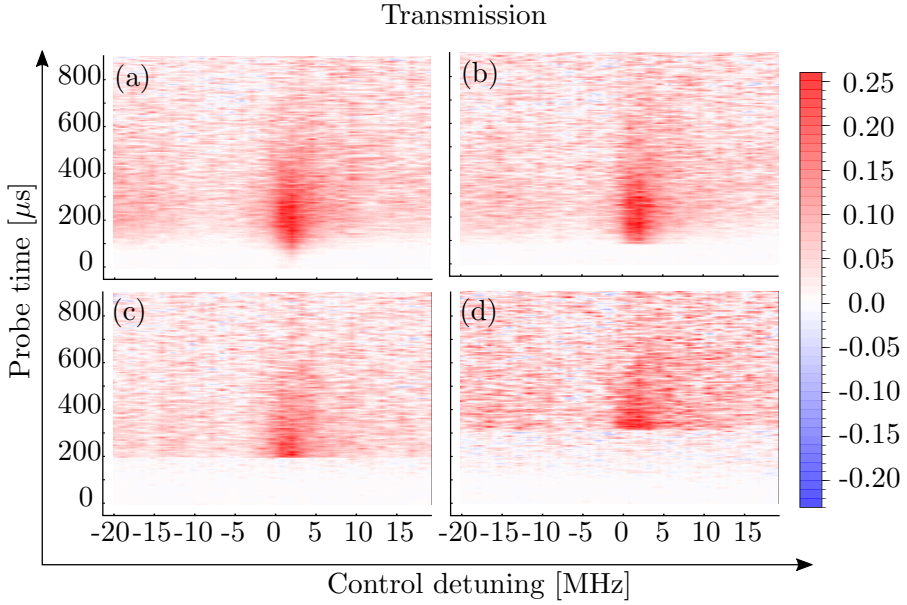

Figure 5.11.: EIT signals control beam turned on for dalays (a) 0 μs, (b) 100 μs, (c) 200 μs and (d) 300 μs. Measurements are performed for $26D_{5/2}$ state. Measurements are made for the atoms outside the fiber.

states.

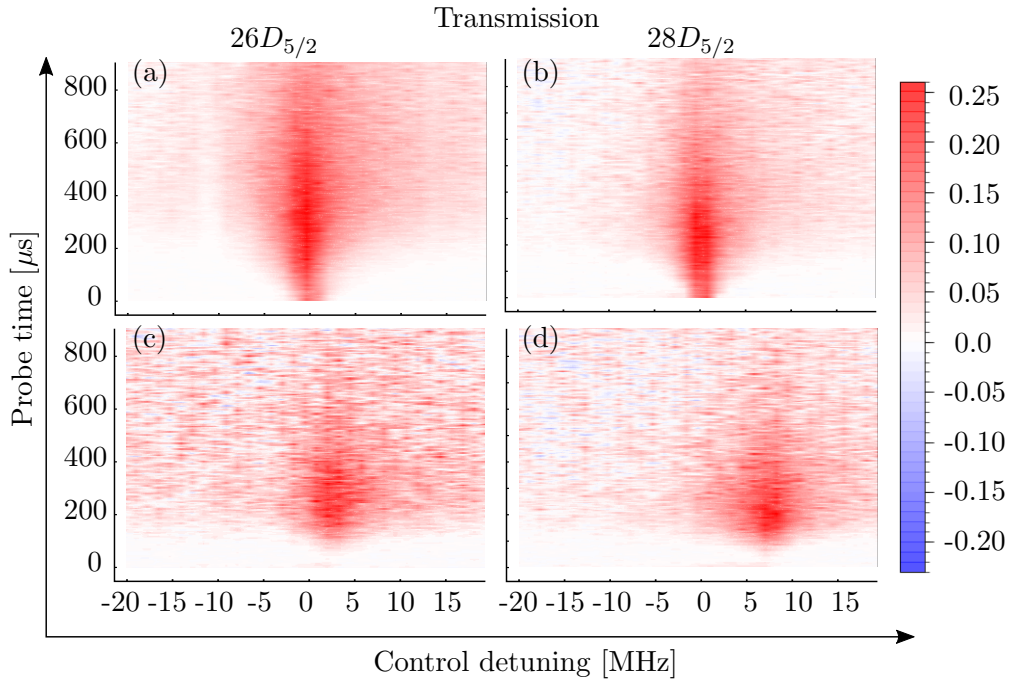

Figure 5.12.: Shift in EIT signals for $26D_{5/2}$ and $28D_{5/2}$ states. EIT signal of the atoms at (a) and (b) MOT position and at (c) and (d) 5 mm inside the fiber.

For a systematic study of the nature of the shift, the lineshift for different states is estimated from the data. To obtain the shift only due to the fiber, the EIT peak at MOT position is subtracted from those of the inside the fiber. Now, by fitting a model obtained from the Alkali atom line calculator [47], it predicts the lineshift as n^7 dependence as shown in the Figure 5.13. The good agreement between the data and the model explains the origin of shift which is coming from the electric fields due to residual imbalanced charges. The estimated value of the electric field is about 3.3 V/cm which was also reported in our previous experiment [60].
To continue the study of the fiber's response on the EIT lineshift, further measurements are made for different positions inside the fiber. A chart of such shift measurements are shown in the Figure 5.14. Here, the shift is not clearly consistent along the fiber position. This could be attributed to a random distribution of the adatoms sitting at the fiber wall inside.
From the two sets of the measurements, it is confirmed that the reason for the lineshift is originating from a stray electric field produced by the charges or the atoms sitting at the wall inside the fiber. It can be anticipated that for a given high enough charge density, an enclosed geometrical structure should be able to cancel the fields in the central region. In this case, if the fiber wall gets coated with a large number of charges, the core region should not have any stray field. This imagination led to a

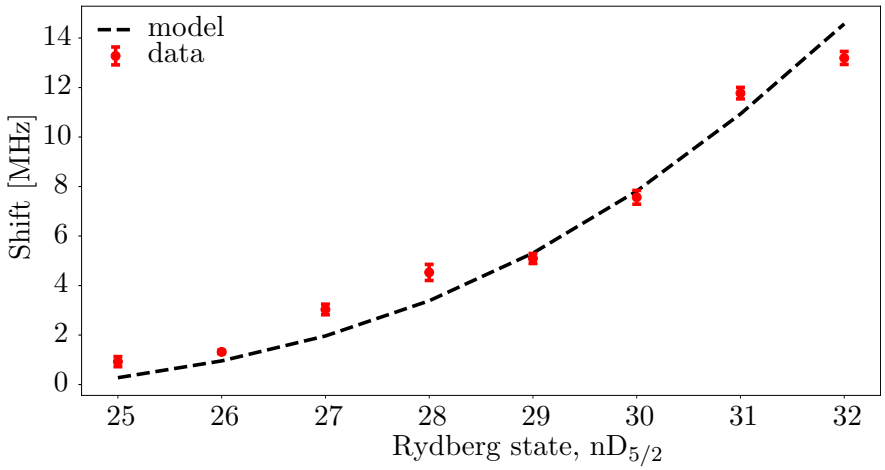

Figure 5.13.: Lineshift for different Rydberg states. Model maps the data to estimate electric field present. Measurements are taken for the atom 5 mm inside the fiber.

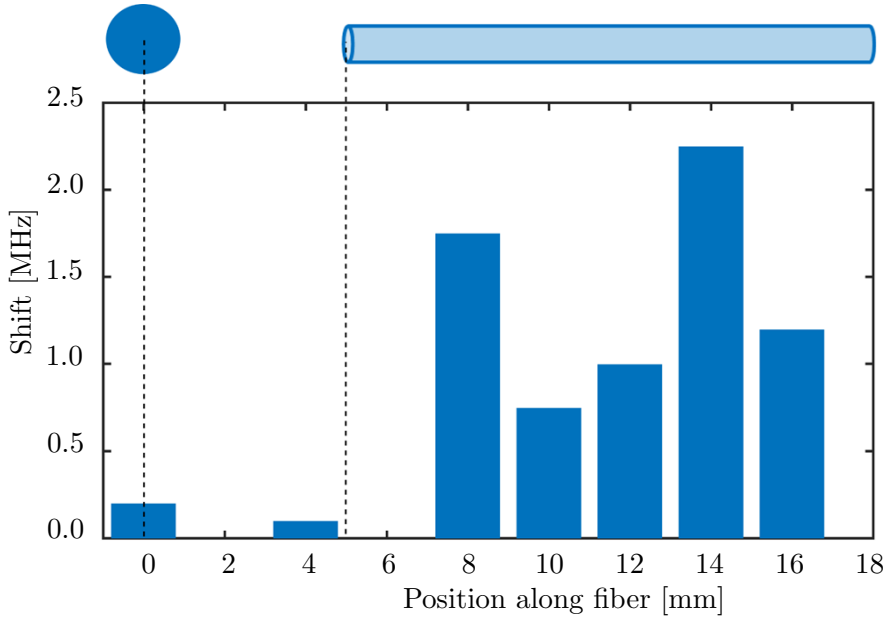

Figure 5.14.: Lineshift at $26D_{5/2}$ state for different positions along the fiber axis.

new experimental setup where different sets of HC fibers are exposed to vapour of Rb atoms at room temperature. Such high atom number should fill and coat the fiber wall from inside. With this motivation, a detailed study of such system is made which is described in the next section.

5.2. Rydberg EIT with thermal atoms

The field of cold-atom physics has been successful in exaggerating many quantum properties at fundamental level. This is primarily supported by the longer coherence times and preparation of pure states. However, all these features come with a cost of highly demanding precision control and stringent experimental needs. Added to that, the actual measurement time is only a fraction of the sample preparation time which also sets a limitation to the number of measurements made in a given time interval. In contrast, atomic ensemble at room temperature, such as vapour cell suffers from unavoidable motional dephasing and broadening. However, for a more practical purpose, such field applications, these room temperature setup should be an ideal candidate for its low demand on resources. With certain limitations, a set of important experiments can be demonstrated with these thermal atoms. A part of this experiment is also discussed in these bachelor's theses in our group [95, 83].

5.2.1. Experiment

The experimental setup consists of several HC fibers placed inside a vacuum chamber shown in Figure 5.15. The inset image shows a number of glass tubes which contain the fibers in order to label them separately. On the one end of the chamber, a sealed glass ampoule of Rb is placed inside bellows attached to a gate valve. The Rb atoms are isolated from the environment to avoid the vigorous reaction with the atmosphere. Once the sufficient vacuum level is reached, the ampoule is broken by bending the bellows. As a result the pressure inside the chamber increases since the glass ampoule is filled with certain inert gas. The surge of released gas can potentially damage the turbo pump since it is running at full speed, therefore care is taken by closing the gate valve before breaking the ampoule and then opening it slowly. The turbo pumping system is kept operational which eventually pumps out the excess particles and the original vacuum level is reached. An ion pump is attached to the chamber to maintain the low pressure inside the chamber for stand-alone vibration free operation. The ion current is also calibrated to monitor the pressure inside the chamber thus no vacuum gauge is mounted to the system. In the end the external gate valve is closed and the pumping-station is removed once the desired pressure is reached. The Rb vapour pressure inside the chamber is controlled by its temperature, therefore, a heating tape is wrapped around the chamber. Additionally, by regulating the gate valve attached to the Rb source, amount of released atoms can be controlled.

5.2.1.1. Fiber cleaning procedure and Rb signals

For a vacuum system, an HC fiber acts as a capillary with extremely narrow hole and long length. Thus the flow rate of particles through these holes should be extremely slow due to differential pumping action. For the experiments with Rb atoms, it is desired to reduce any background pressure. Therefore, the cleaning of the fiber from

inside becomes very important. To accelerate the process of diffusion of particles from the fiber core, it is heated to high temperature. Once the vacuum reaches a quasi-steady state, the chamber is filled with N_2 gas. it is speculated that these N_2 gas particles would rush into the fiber core and thus increasing the molecular dynamics in the core region. By repeatedly filling the chamber and thus the fiber with N_2 and pumping it, the cleaning process of the fibers is achieved. The details of the experimental procedure are described in the Appendix C.1. Once the final vacuum level is reached, the ampoule is broken by bending the bellows as shown in Figure 5.15.

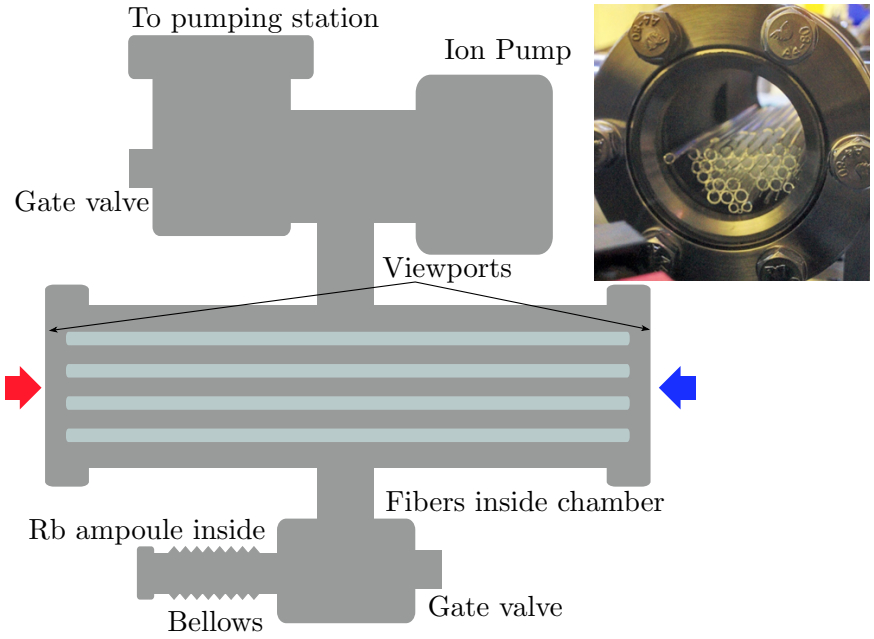

Figure 5.15.: Vacuum chamber for room temperature atom-fiber setup. Optical access are through the two viewports. Hollow-core fibers are placed inside the main chamber.

In the final stage of the setup, a vacuum level below 10^{-7} mBar is achieved which is maintained just by the ion pump. Rb valve is opened and the ampoule container is heated to fill the chamber with Rb atoms. To detect the atoms in the main chamber and inside the fiber, a near-resonant 780 nm laser beam is scanned to observe any absorption signal. Initially for several days no Rb absorption signal was detected which was presumably caused by the atoms sticking to the inner walls of the chamber and other surfaces. This way the actual pressure of the Rb atoms in the chamber is reduced. Once the surfaces coating gets saturated, the sufficient absorption signal is clearly visible in both, the chamber as well as the fiber core.

5.2.1.2. Light induced atom desorption (LIAD)

With the high electron affinity Rb atoms are known to bind with any surface by the process known as adsorption. In the context of the hollow core fiber inner wall, the surface area to volume ratio significantly large due to its small core size. This leads to a large number of atoms filling the fiber and sitting at the inner surface. By shining a light to this interface, these atoms can be released by a process known as light induce atom desorption or LIAD. Much like photo-electric effects, the desorption rate further depends on the wavelength, i.e. for smaller wavelengths the emission rate of atoms is larger. In this project, the 480 nm laser is used to engage the desorption process as the effects are significantly larger as compared with 780 nm wavelength. The blue laser is slightly misaligned such that a large fraction of the light beam propagates through the inner glass material and thus the desorption process can be controlled. Care is taken to avoid any Rydberg transition associated with the 480 nm laser beam in for the absorption measurement.

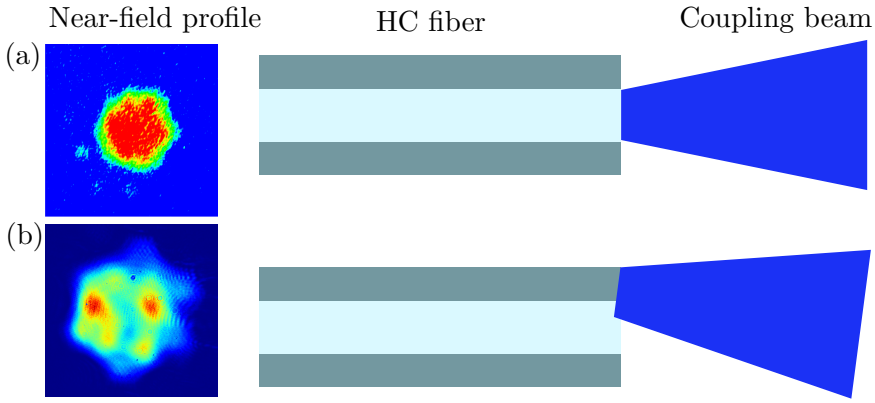

Figure 5.16.: Misalignment of blue beam for LIAD. (a) Well aligned beam and (b) intentionally misaligned beam.

In an ideal condition, the release of atoms from the surface is depicted in the Figure 5.17. Here, initially a high density of atoms are stuck at the fiber wall. After the launch of the blue beam, the atoms start to come out and eventually fill the fiber. This is where the density is maximum. At this moment, the pressure inside the fiber reaches way above than that of the vacuum chamber. This high pressure results in a much higher absorption of the probe beam as shown in the Figure 5.18. Although a perfect coupling into the glass material is not guaranteed by this method, a significantly large OD about 38 is detected as a result of desorption. The LIAD mechanism allow for a rapid control of the Rb atom density inside the fiber. Eventually, the atoms start to flow outside the fiber due to the local pressure difference. Therefore, on the timescale of 100's of seconds the absorption signal starts to reduce as shown in Figure 5.19. In other words, the total number of atoms inside the fiber decays down. After a period of a day, the loss is recovered by a slow influx of ambient Rb atoms.
The adsorption of atoms on the fiber surfaces has been known to introduce uncon-

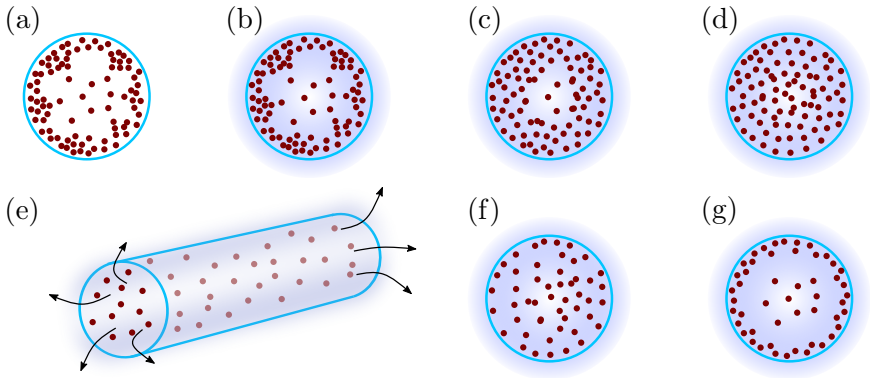

Figure 5.17.: Atoms inside HC fibers. The process of LIAD increases the atom density inside the fiber. (a) Atom distribution inside HC fiber, (b) to (d) with blue light turned on, pressure increases, (e) atoms come out of fiber, (f) and (g) density decreases inside the fiber.

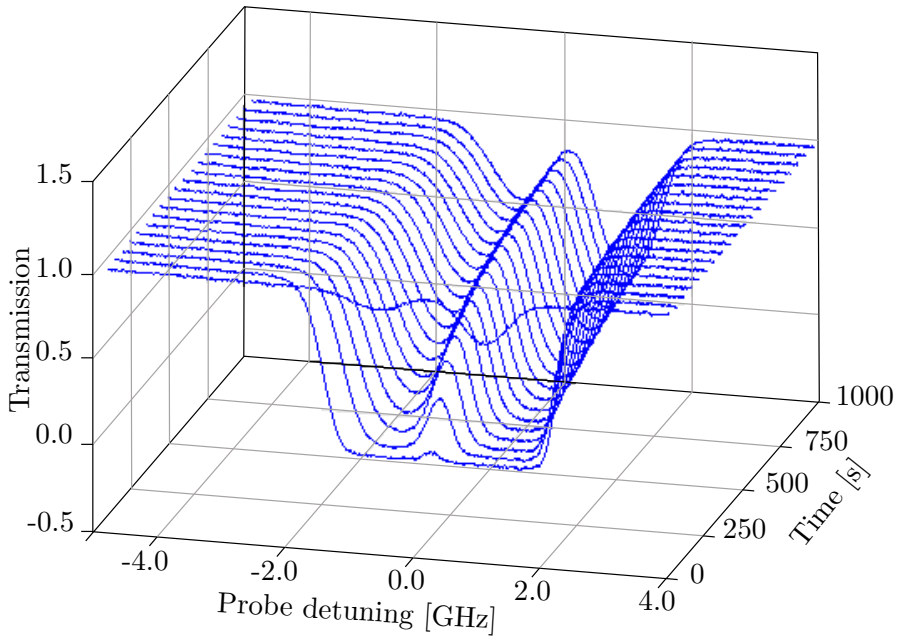

Figure 5.18.: Absorption due to LIAD with the blue light coupled to the cladding.

trolled electric fields. The valence electron of the surface bound atom is attracted towards the Oxygen atoms present in the glass material. This in return creates a positive field near the Rb atoms pointing towards the fiber core. With the LIAD mechanism a shuffle of atom distribution can be achieved thus creating a more homogeneous charge distribution.

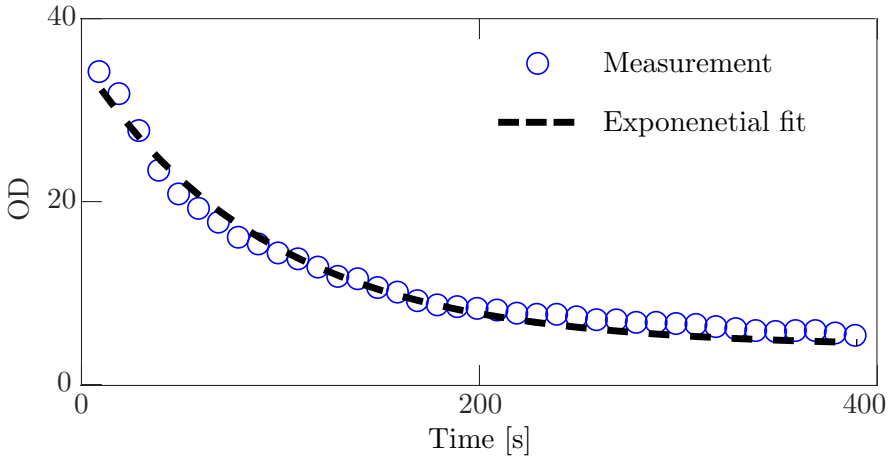

Figure 5.19.: OD measurements with the presence of the LIAD beam.

5.2.2. Rydberg EIT inside fiber at room temperature

Obtaining Rydberg EIT signals at higher states near surfaces has been challenging task due to the atom-wall interactions. In this experiment, the room temperature fiber-atom setup is implemented to study the processes that can affect the line shifts as seen with the previously discussed cold atom setup. Here, a set of fibers with different core sizes, geometries and coatings is used to explore the lineshifts of the Rydberg EIT utilizing its high sensitivity towards external fields. To characterize the EIT signals, the control laser is scanned while the probe beam is kept on-resonance as shown in the Figure 5.20. This way the absorption background due to the thermal atoms can be avoided.

These EIT lines, in contrast with the cold-atom setup can still be seen all the way up to 61 state. These results are remarkable and counter-intuitive as one would expect the cold-atom setup is more "clean". The observation of EIT lines at very high Rydberg states with only marginal shifts proposes several interesting highlights of the thermal atom-fiber setup. These results bring a step close to creating a Rydberg atom-fiber system for strongly interaction photonic system. A first interpretation of these results can be associated with a reduced overall electric fields present inside the fiber. The idea is supported by considering that the layer of atoms sitting inside the fiber can act as a conductive shielding. The high atom density due to continuous filling at vapour pressure should make a homogeneous coating. Hence, any charge produced inside can be distributed in a cylindrically symmetric geometry making the central zone free of field in much like a closed metallic surface. Thus these results hints at a possible way of performing high Rydberg state experiments in the cold-atom setup by utilizing fiber core coated with metallic materials. In what follows is a detailed study of the lineshifts and the lineshapes to evaluate the hypothesis and to explain the origin of the shift and the broadening.

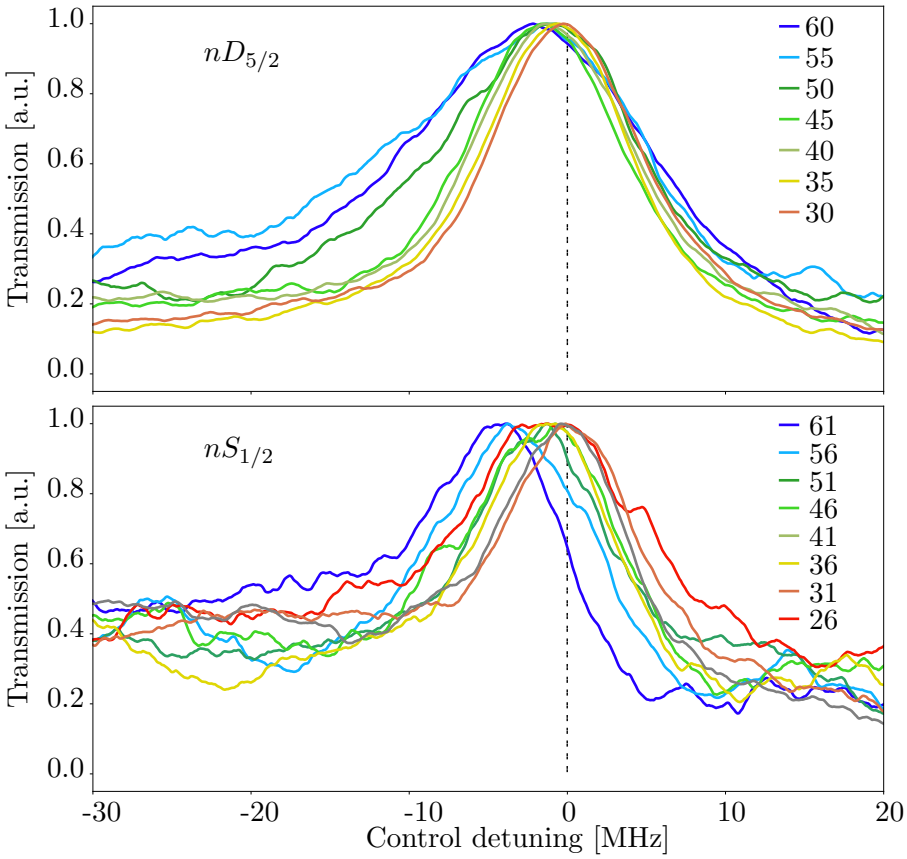

Figure 5.20.: Rydberg EIT for different n states shown by the legends.

In the Figure 5.21 the Rydberg EIT lineshapes are compared for the inside fiber as well as a signal from the free-space in the vacuum chamber along with theoretical models. To reduce the electric field sensitivity, the Rydberg excitation was chosen to 25D state for the subsequent analysis. The EIT inside the fiber has a dramatically different lineshape as compared to the one seen from the chamber signal. Besides the broadened linewidth inside the fiber, the off-resonant dips are absent as one expects in a thermal EIT line as illustrated in the Figure 2.13. In the Figure 5.21(a) a Gaussian model fits well to the inside fiber signal while it lacks certain features in the free-space signal.

To explain the lineshapes, the broadening due to the transit times are taken into consideration for the thermal vapour. As for the given fiber core size of 40 μm the atoms would only spend a time $\sim$ 150 ns exposed in the laser beams. The chamber signal, however, does not suffer from such effects as for the chosen beam size of about 2 mm the interrogation time is significantly large. The short exposure, in the fiber eventually reflects in a limitation of the measurement accuracy as a result of line broadening of about 4 MHz. Furthermore, the intensity of the probe beam is kept

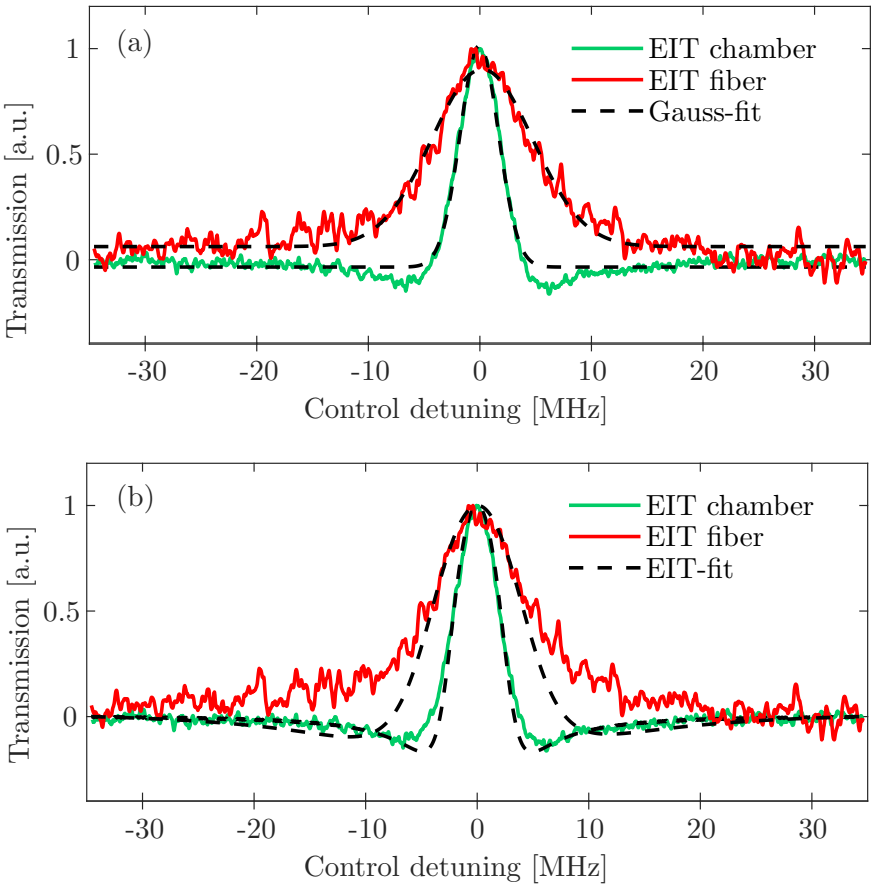

Figure 5.21.: Rydberg EIT lineshapes for signals from the chamber and the HC fiber with (a) Gaussian fit and (b) EIT fit model.

high in order to see any EIT signal which led to a saturation broadening. The fits shown in the Figure 5.21(b) are obtained by numerically solving the optical Bloch's equation for a non-negligible probe intensity. The EIT lineshape from the chamber is very well explained by the model here. However, the signal from the inside of the fiber has significant deviation from the model. The possible reasons could come due to the exact propagation of the probe beam when it encounters an inhomogeneous optical path, for example. In this case, the susceptibility due to the atoms inside the fiber is modified by the control beam which has a steep Gaussian shape. The details of such possibilities are discussed in the next chapter.

The Rydberg EIT measurements for different states have shown alteration in the transmission signal as presented in Figure 5.20. Although the exact mechanism for linewidth is not yet uncovered, the observation of the shift in the peak signal carries certain useful information. A usual speculation is that the shift could arise from stray electric field due to atoms or charge distribution inside the fiber. To analyze the lineshifts, S state signals are considered as the D state contains three sublevels which

have different shifts associated with a given electric field. The measured lineshifts are plotted in the Figure 5.22 with an overlay of a simulated shift by using the polarizability for each states. Keeping the electric field as a free parameter, the optimized fit results in the estimation of the stray electric field. It is remarkable to notice that the field present in the thermal atom-fiber setup is much smaller than that in the fiber for the cold-atom setup 5.13.

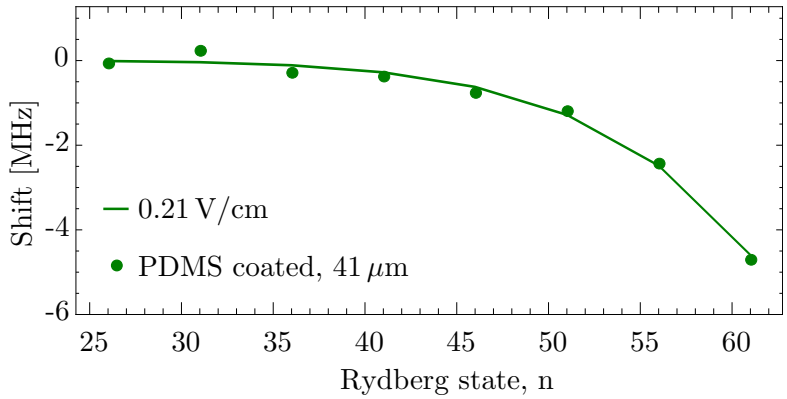

Figure 5.22.: Shift in EIT lines for different states shown by the markers. Fitting a model using stark shift shown by the dashed lines. The legend shows estimated electric field.

One useful interpretation of this result is that the presence of sufficiently large number of atoms inside can coat the inner wall of the fiber. This layer of Rb atoms creates a Faraday cage which further ensures shielding form any fields outside the fiber [68]. Similar measurements have been made in other research groups as well [2].

5.2.3. Fiber core types and coating

Another important purpose of this experiment is to verify the influence of core sizes or material coating which can affect the Rydberg EIT lineshifts. To this end, 4 different types of fibers were used in which each of them were either uncoated or coated with PDMS or Sol-Gel materials. The reason for choosing these materials is that such coatings have been known to enhance spin relaxation times with the ground state atoms [16]. The motivation here is to explore how these coatings affect the EIT lineshapes associated with the Rydberg states.
In the Figure 5.23, the EIT lineshifts are plotted for all the fibers with different coatings. The estimated electric fields associated with these fibers are on the similar order and stay very small. The reason for the relatively high field present in the 4th fiber is not clear yet but it could result from incomplete cancellation due to inhomogeneous layering of Rb atoms inside. Part of the reason can come from the inhomogeneous distribution of the blue beam on the inner surface of the fiber. As a result the redistribution of Rb atoms can only take place in certain regions. These measurements on the one hand confirm the claim made regarding atoms acting as Faraday cage.

On the other hand, coatings or the core sizes do not affect the measurement results significantly.

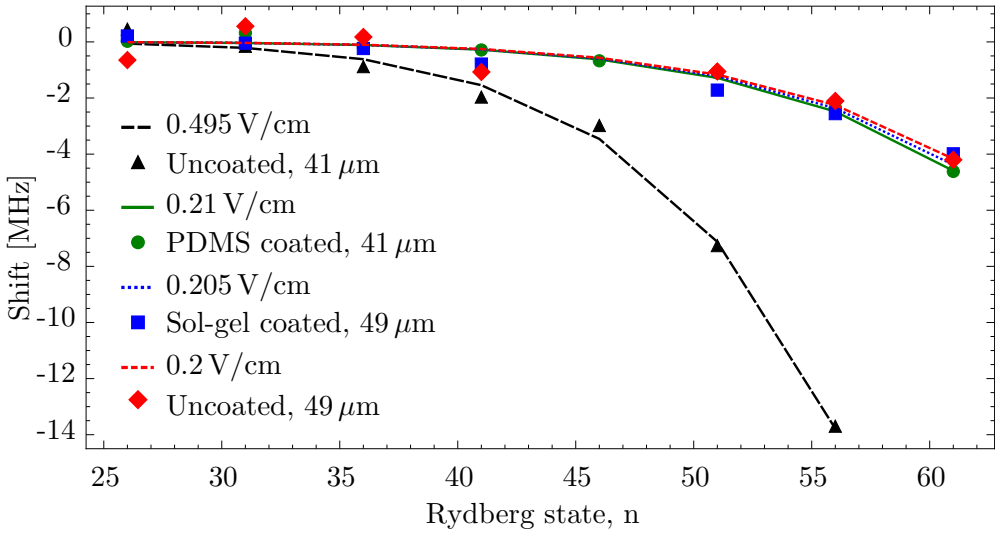

Figure 5.23.: Shift in EIT lines for different states for difference fibers shown by the markers. Fitting a model using stark shift for different states shown by the dashed lines. The predicted fields are shown in the legend.

Motivated with the results from the thermal setup shown in the Table 5.1 led to perform LIAD-like experiment with the cold setup in order to redistribute the adatoms from the inner surface. Thus the blue laser beam which is used as control laser is coupled to the cladding of the fiber. A measurement of the OD failed to show any absorption. In yet another approach, a large sequence was run where atoms were transported and dropped inside the fiber to "create" controlled coating. However, the results on EIT lineshift still showed no change. These null results hint at the fact that the number of atoms that were transported is too little as compared to that in the thermal setup.

Fiber type	Condition	Estimated $\mathcal{E}$ field
41μm	Uncoated, thermal atoms	0.495 V/cm
41μm	PDMS coated, thermal atoms	0.210 V/cm
49μm	Uncoated, thermal atoms	0.205 V/cm
49μm	Sol-gel coated, thermal atoms	0.2 V/cm
60μm	Uncoated, cold atoms	3.3 V/cm

Table 5.1.: Estimated electric field for a variety of fiber types and conditions. The last entry (highlighted) compares the electric field for the cold atom-fiber setup.

As a final remark, the confirmation of Rydberg EIT signals has set up the platform

required for a fiber based light-matter interface. The difficulty of Rydberg excitation near surfaces as found in various research have shown seemingly impossible task. However, in such experiments, flat surfaces were chosen which had shown very high electric field. Work done in this thesis establishes excitation of Rydberg EIT beyond $n = 60$ state which is a promising result for quantum optics with room temperature atom-optics. Here, high Rydberg state is an obvious choice as the associated Rydberg blockade radius becomes significantly large. As an application, achieving storage of quantum information and generation of several non-classical photons at room temperature is a promising goals [79]. Even though, the smaller fiber core size offers a short transit time, the experiments such as storage and retrieval of photons can be performed at timescales of few ns, which can benefit from the simplicity and the implementation of the setup.

6. Beam propagation and detection

The experimental setup discussed in Chapter 5 features a novel technique for creating strong light-matter coupling. Here, such coupling is explored by the geometrical confinement between the atomic and optical overlaps. On one hand, the precision control over the axial direction allows for positioning the cloud accurately at any location along the fiber axis, on the other hand, the radial confinement allows for a control over the coupling of light with the atoms by tuning the spatial overlap. An ensemble of atomic cloud strongly modifies a probe beam specially when it is tuned near the resonance is presented in Chapter 2. In a semi-classical treatment, these atomic media offer a complex refractive index as the weak probe beam passes through. As a result, the beam encounters strong dispersion along with resonant scattering. In a typical transmission measurement, where a probe beam passes through a large atomic ensemble the absorption properties are dominant and have significant contributions in the detected signals. The weak dispersion effects only change the global phase of the beam and leave no influence on the detected signal. In contrast, the confined atomic ensemble featured in the experimental setup in Chapter 5 produces spatially varying phase modulation much like a lens. Due to the inhomogeneous dispersion, the mode of the propagating light beam gets altered which strongly depends on the laser detuning from the atomic transition line. Combined with the absorption which is also spatially dependent due to the atomic density, the exact probe-beam field profile after passing through the cloud requires a complete understanding of beam propagation through the atomic ensemble.
In this chapter, dispersive effects are utilized for non-destructive measurements. The beam profile after passing through confined atomic cloud is calculated by a beam propagation model. By analyzing the full beam propagation, complete absorption line shapes are calculated which are compared with the detected signals. Furthermore, Rydberg EIT line shapes are studied where the control beam additionally modifies the inhomogeneity of the dispersion.

6.1. Atomic ensemble as dispersive medium

In the detection scheme, a Gaussian probe beam is mode overlapped with the optical lattice beams. As the trapped atoms acquire the lattice beam configuration, the probe beam encounters a high degree of mode overlap with the atomic ensemble. Due to the extended overlap between the light and atoms, the interaction strength which is a measure of light-matter coupling, gets enhanced. Among the various other techniques, the system presented in this work provides an interesting light-matter interface. As a figure of merit, optical depth (OD) of this system demands a need for detailed study

of beam propagation through the cloud which acts as an optical media that modifies both, the absorption as well as the dispersion. To a good approximation, the atomic cloud is assumed to have radially symmetric Gaussian distribution with much longer extent along the fiber axis which is expressed as,

$$\rho = \rho_0 \exp\{-\frac{z^2}{2\sigma_z^2} - \frac{x^2+y^2}{2\sigma_r^2}\}, \tag{6.1}$$

where, ρ_0 is the maximum density that corresponds to the center of the cloud. σ_z and σ_r are axial and radial width of the density distribution.
To obtain the beam propagation, the paraxial wave equation (PWE) with the atomic density distribution in the geometric confinement is solved. As discussed in Chapter 2, atomic cloud serving as a medium with susceptibility, χ contains the features of absorption and dispersion and is represented as

$$\chi = -\frac{\sigma_0 \rho(x,y)}{k_0} \frac{2\delta_p/\gamma - i}{1 + 4(\delta_p/\gamma)^2 + I/I_{sat}}, \tag{6.2}$$

where, σ_0 is resonant scattering cross section, k_0, δ_p and γ are wavevector, laser detuning and transition linewidth. The experimentally convenient parameters, I and I_{sat} are the probe beam intensity and the saturation intensity associated with the transition. In the experiment, the power was kept below 200 pW which corresponds to intensity below 1% of I_{sat} and can be ignored for the subsequent calculations. The susceptibility is related to the real and the imaginary parts of refractive index as shown by the Kramer-Kronig relation as shown below:

$$n_r = 1 + 1/2Re(\chi), \tag{6.3}$$

$$n_i = 1/2Im(\chi). \tag{6.4}$$

The Figure 6.1 shows the qualitative values for refractive indices for varying laser detunings. To include the complete atomic distribution, χ is calculated for the atomic cloud released from the trap confinement. Along with the density dependence, the real and the imaginary parts of the refractive index are highly modulated by the detuning of the probe laser beam. An illustration is shown in Figure 6.2 where the real and the imaginary parts of refractive index are represented for a set of detunings and radial positions. It is evident from the simulated results that the values of the two indexes are maximum at the center of the cloud where the density is maximum. Additionally, the spectral response adds meaningful information about the type of interaction – in the pure absorption, n_i, the values drop very rapidly as the detuning increases. While for the dispersion, i.e. n_r, remains non-vanishing for farther detunings. The dispersive detection techniques have been proven useful for non-destructive measurements [75]. Here, the laser detuning is kept far enough to minimize the on-resonant scattering processes while still having significant influence to be detected utilizing the dispersive features. In the coming sections, these features are explored with applications in detection techniques.

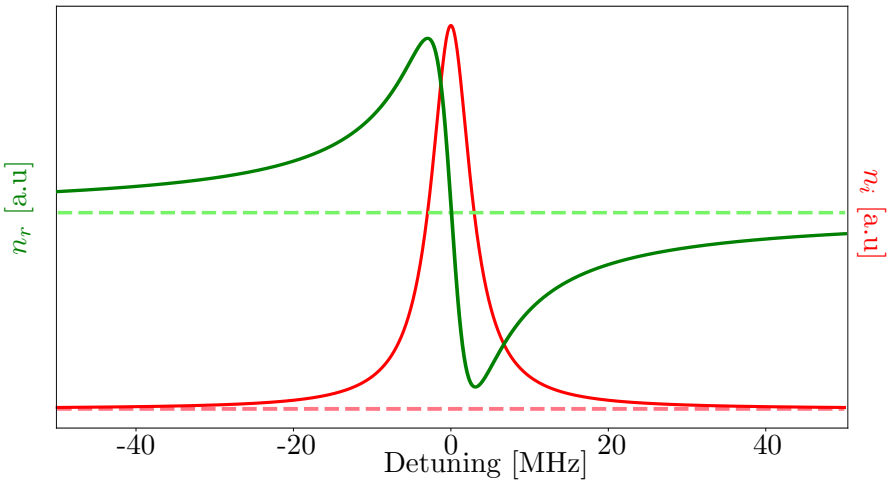

Figure 6.1.: Detuning dependence of real and imaginary parts of refractive index. The dashed lines represent signal in absence of atoms.

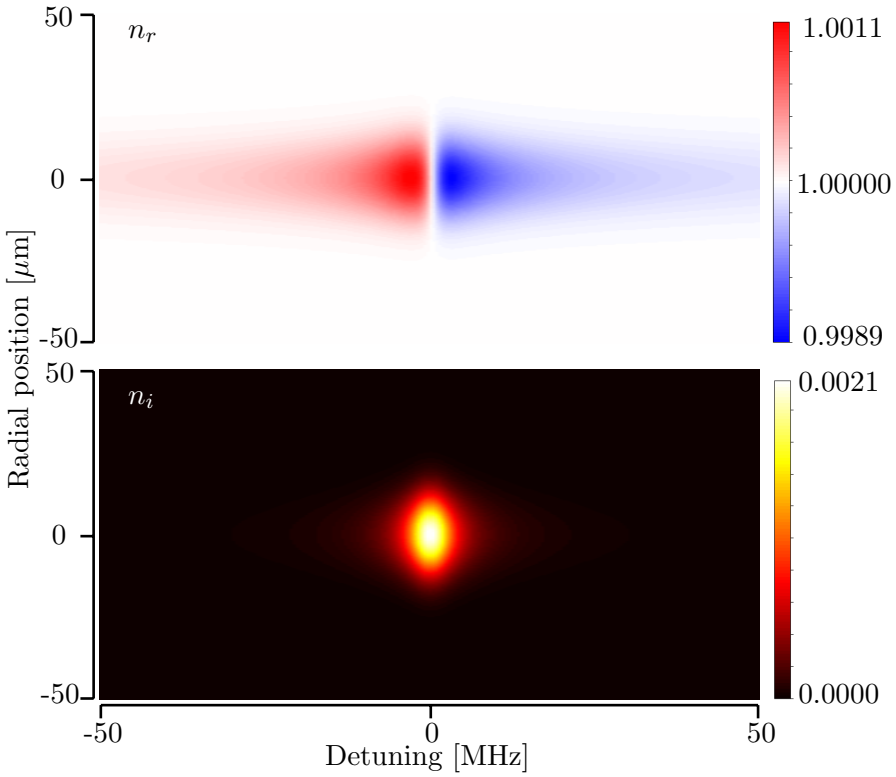

Figure 6.2.: Detuning dependence of real and imaginary parts of refractive index for radial distribution.

6.2. Polarization rotation

In the cold-atom physics one of the most conventional detection schemes is using absorption imaging where an on-resonant probe beam is sent through the atomic sample. As the beam propagates, it gets scattered by the atomic cloud with the maximum scattering rate occurs when the laser is tuned exactly to the corresponding atomic transition line. Fluorescence or absorption imaging techniques are based on this scattering phenomenon. Although such methods are widely utilized in the fields of cold atoms, it also comes with certain issues. One of the major limitations is that this technique is destructive, in that once an atom undergoes the scattering event, either it looses its coherence properties or it gets kicked out of the region of interest due to momentum transfer. No further measurements can be made regarding its quantum properties. Alternate methods need to be established to circumvent these issues. Off-resonant imaging can reduce the scattering rate but it simultaneously suffers from the noise as the signal strength also gets reduced significantly as depicted in the Figure 6.1. Dispersion, as the signal does not decay as rapidly as with the scattering rates shows a potential tool in non-destructive detection. In this case phase of the beam gets altered based on the detuning from the atomic transition as shown in Figure 6.1. Using a phase sensitive detection scheme, presence of atoms can be estimated. To implement this scheme, atomic transition rules are utilized for precise controls. In particular, polarization dependent phase shift is generated which results in rotation of the beam's plane of polarization and can be detected using a balanced pair of photo-detector.

6.2.1. Detection scheme

This detection technique utilizes the ground state hyperfine states of ^{87}Rb that have relatively very long coherence time. These states are suitable for applications like photon storage [64], atomic clock [66], interferometry [50, 22]. Common to all these experiments lies the challenge of making precise measurement of the atomic population of a pair of the hyperfine sates. Among the other noise sources, the shot-to-shot atom number fluctuation causes noise in the measured quantity. The remedy is to measure the population in both the states in the same experimental run. A typical on-resonant detection leading to scattering can alter the population of the two states. Hence, simultaneous measurement of the two states is prone to inaccuracy associated with the measurement process. In contrast, the dispersion signal being non-vanishing even for far off-resonance where the population mixing processes are insignificant. Therefore, simultaneous detection of two states is not limited by the detection process. Furthermore, longer integration times are possible which reduces the detection noise. For the experimental realization, ultra-cold ^{87}Rb are prepared in $|F = 1, m = 0\rangle$. The hyperfine transition resonant radio frequency of 6.835 GHz RF is coupled to drive the atoms to $|F = 2, m = 0\rangle$. These states are decoupled from the first order magnetic Zeeman effects therefor are used for precision measurements as in the case with atomic clock, hence also known as clock states. Based on the amplitude and the pulse dura-

tion, different RF spectroscopy schemes are applied to manipulate the atomic states in what is known as Bloch sphere[ref]. Such schemes are typically used in precision measurements using atom interferometry, atomic clock, quantum information processing, etc. The goal here is to establish a novel detection system while preserving the atomic number state such that repeated measurements can be performed to obtain more accurate information about the atomic population and hence the associated measurements. To achieve this goal, two probe beams, tuned near D1 transition line are used. In particular, the two beams address the transitions $|F = 1, m = 0\rangle \leftrightarrow |F' = 1, m = 0\rangle$ and $|F = 2, m = 0\rangle \leftrightarrow |F' = 2, m = 0\rangle$. To establish the dispersive detection, both the lasers are set off several linewidths away from the actual transitions as shown in Figure 6.3(a).
For the chosen level scheme shown in Figure 6.3(b), the π transition is forbidden due to the transition rules. Hence, a laser beam corresponding to π transition will not have any influence from the atoms. While the σ transitions cause the beam to encounter a phase shift. As a result when a linearly polarized beam at certain angle is passed through the cloud, it becomes elliptical. which results in axis rotation when passed through a quarter waveplate. The rotated beam has different intensity in the two arms as it passes through the PBS. Two detectors placed on the both arms show imbalanced signals.The difference between the two signals is a measure of polarization rotation, which inherently gives an estimate on atom numbers in the two states in the same experimental run.

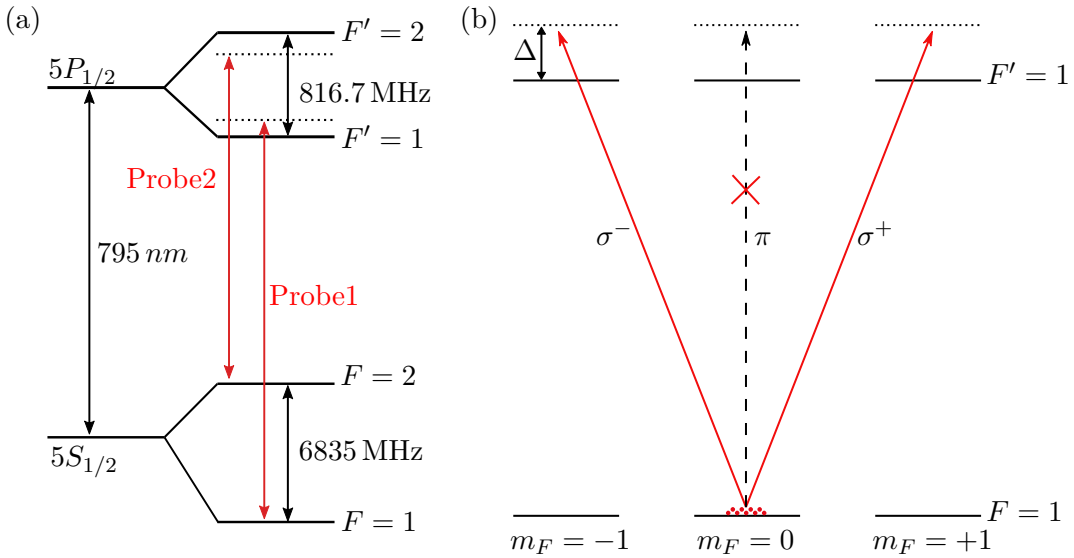

Figure 6.3.: (a) D1 transition line structure of ^{87}Rb. Two beams, probe1 and probe2 address the population in $|F = 1\rangle$ and $|F = 2\rangle$ states. (b) Magnetic sublevels of the two hyperfine lines with allowed transitions.

To illustrate the polarization rotation effects, D1 transition of ^{87}Rb $|F = 1, m = 0\rangle \leftrightarrow |F' = 1, m = 0\rangle$ is utilized as shown in Figure 6.3. Linearly polarized probe beam is

sent through the cloud. The axis of the beam is precisely adjusted using a half waveplate. Additionally, a weak magnetic field is applied to set the quantization axis along y-axis as shown in Figure 6.4. In this configuration the electric field component of the beam along the y-axis can only excite a π transition which is forbidden for the selected transition states. Hence, the beam does not sense the presence of atoms. While the orthogonal component, i.e. polarization axis along x-direction can be decomposed into the right circular and the left circular polarizations. These circular polarizations are no longer forbidden for the transition and excite the σ^+ and σ^- transitions as shown in the Figure 6.3(b). As a result, the x-component of the light field encounters a phase shift while the y-component stays unaltered. After traversing through the atomic cloud, the two components differ in their relative phase that makes the beam elliptical in polarization. A pre-adjusted quarter waveplate rotates the primary axis and make it linear. The beam after passing the PBS shows imbalance in the intensities in the two arms which are detected on two detectors.

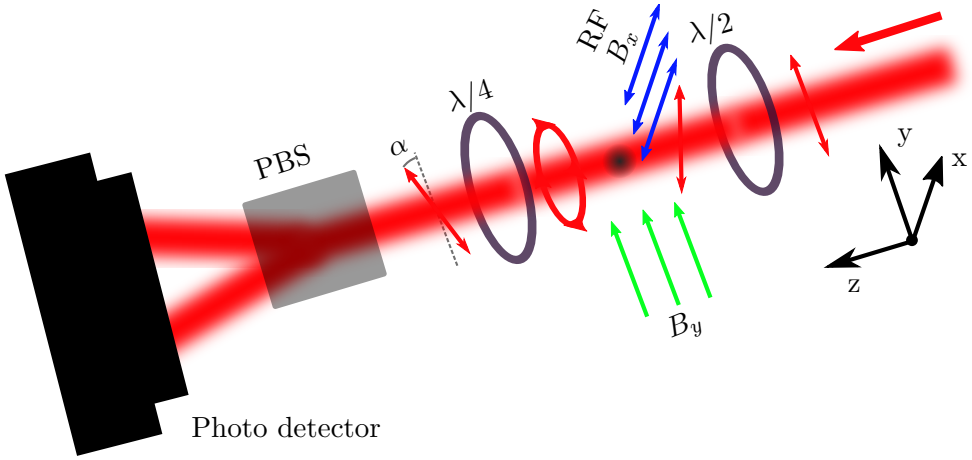

Figure 6.4.: Polarization rotation detection experimental setup. Two probe beams are overlapped and exiting from a single mode fiber (adapted from [48]).

6.2.2. Imaging

The beams after the PBS is directed on spatially distinct parts of a CCD camera. Additional sequence of images are taken to isolate the background light from the actual image of the cloud. A typical processed image is shown below in Figure 6.5. The polarization angle scales with the atom density hence the larger numbers correspond to more atoms. It is noteworthy to mention that the positive and negative values are results of lack or gain of light falling on the sensor. The signal is in sharp contrast with absorption imaging. For the experimental parameter, the number of atoms were about $2.0 \cdot 10^6$. The beam detuning was set beyond $-40\,\mathrm{MHz}$ to minimize any absorptive effects and thus the interferences in the dispersive detection scheme. Another aspect on noise estimation is that the off-resonant dispersion does not have steep dependence

with the laser detuning, hence the frequency noise of the laser has relatively weaker influence on the measured signals.

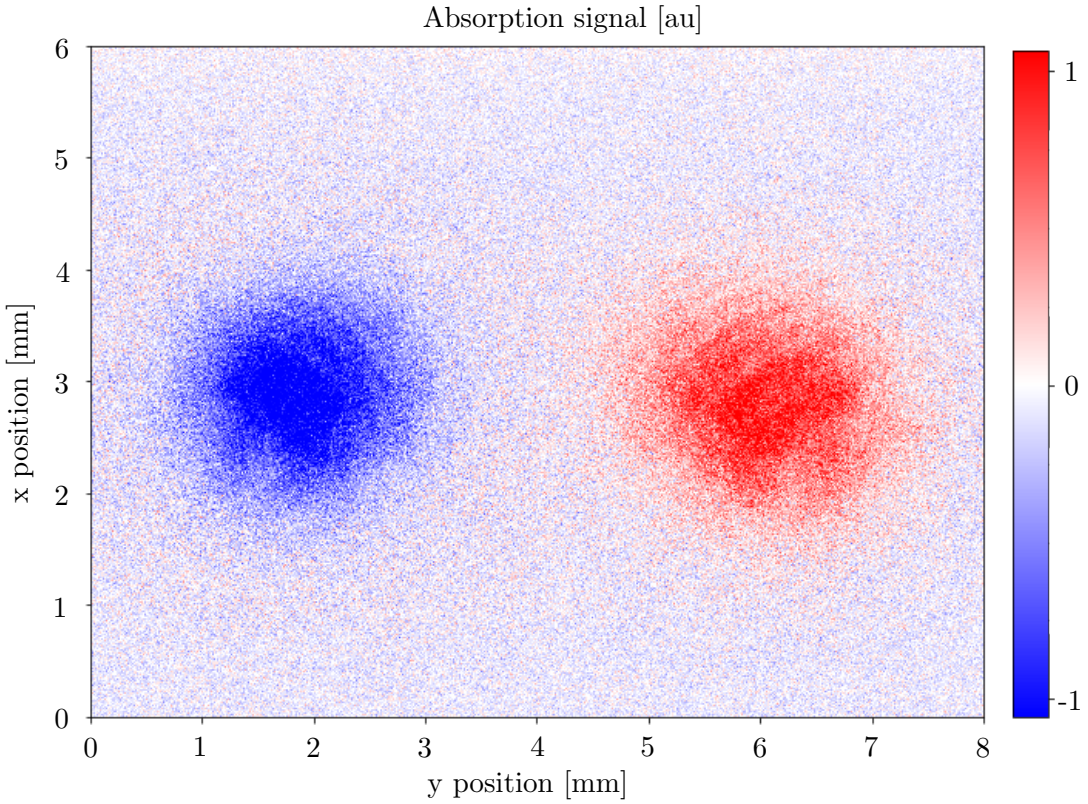

Figure 6.5.: Dispersive imaging. Background removed recorded signal shows reduction in the beam intensity in one arm and the enhancement in the other.

Towards the detection, the atoms are prepared in the $F = 1, m_f = 0$ state, an RF source tuned to the ground state hyperfine transition, 6835 MHz is applied which results in Rabi oscillations in the atomic population. By varying the RF pulse duration, τ_{RF} several population swapping can be observed. A detection scheme as shown in Figure 6.5 is set up for $F = 2$ state. By adjusting RF pulse duration, the images for different relative population are recorded. The population for state, $F = 1$ is measured by repeating the experiment and using a corresponding laser. The combined results are plotted in the Figure 6.7, where the population swapping can clearly be seen. The sum signal has noise subject to the fluctuation in the atom number as the individual state measurements are made at different runs.

6.2.3. Simultaneous detection of two states

The noise due to atom number fluctuation can be circumvented by simultaneous state detection in the same experimental run. As with the dispersive imaging, the condition is fulfilled for the reason that the measurement process does not alter the relative

population in the two states. The time sequence for such detection is shown in the Figure 6.6.

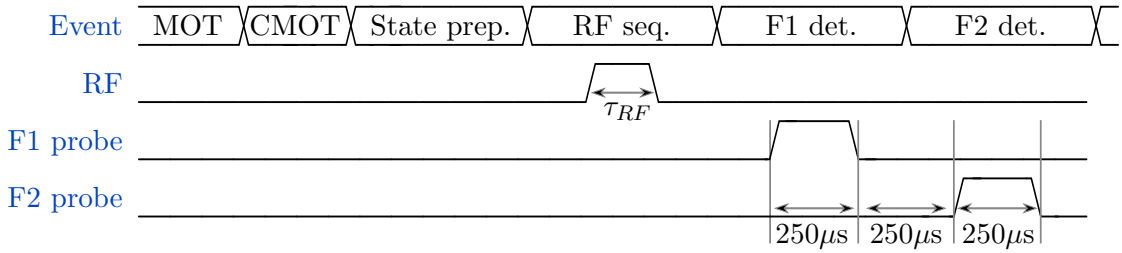

Figure 6.6.: Time diagram of dispersion imaging.

Here, short pulses of both the probe beams are sent sequentially to record the population in the two states. The pulse durations were kept short enough to minimize the atom expansion yet long enough to minimize small measurement noise. Additionally, the probe detunigs corresponding to the two states, namely $|F = 1\rangle$ and $|F = 2\rangle$ are kept $+200\,\text{MHz}$ and $-300\,\text{MHz}$ respectively. Such large detunings minimize the scattering rate which in turn reduces population transfer between the two ground hyperfine states.

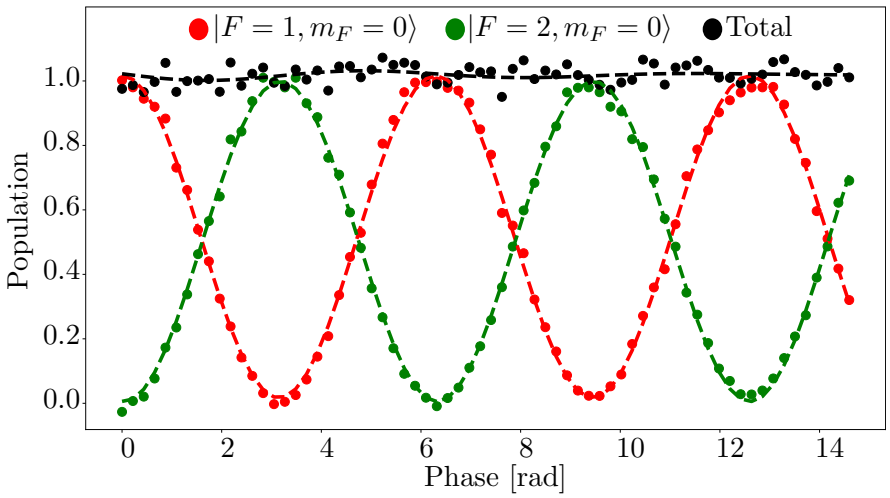

Figure 6.7.: Rabi oscillation between the two hyperfine states.

Using the measurement schemes shown in the diagram in Figure 6.6, the Rabi oscillation of the two clock states are detected for the same atomic cloud. This information is used to normalize the atom fluctuation in each individual run. The corrected Rabi flopping is shown in Figure 6.8 where the population difference is plotted against the phase. The value of the phase is obtained by the following relation,

$$\Phi = \Omega_{RF}\tau_{RF}, \tag{6.5}$$

where, Ω_{RF} is Rabi frequency associated with RF transition which mainly depends on the RF intensity and τ_{RF} is the RF exposure time. As is evident, the shot-to-shot fluctuations due to the atom number is a lot lesser than for the independent measurements. However, there are small deviations still present which can be attributed to the state decoherence, atom expansion during detection or noise coupled to the balanced detector.

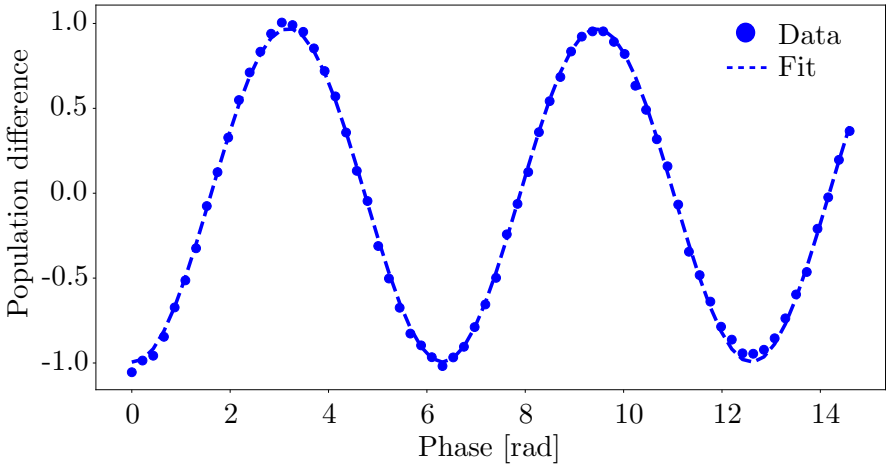

Figure 6.8.: Normalized Rabi oscillation between the population difference.

This section concludes with a demonstration of dispersive effects as polarization rotation, and consequently a tool for non-destructive imaging. The next section concentrates on the spatial properties of a probe beam passing through the atoms in an extended confinement with comparable geometries.

6.3. Beam propagation through extended cloud

As it was evident in the Chapter 5, the exact transmission lineshapes were not explained by the Lorentzian model. The geometrical conditions hint at a requirement for an additional model which should take care of the beam as it passes through the elongated cloud. This is argued from the reason that the atomic medium is no longer homogeneous throughout the beam distribution. Hence, this results in lensing-like effects. In this section, the goal is to develop a model to accurately incorporate the dispersive effects in addition to the absorption.

6.3.1. Split step method

To simplify the model, the atomic cloud is split into small slices as shown in Figure 6.9. As the entering light field passes through each of the slices, it gets modified due to the atomic density distribution. Under the slow-varying-envelope-approximation (SVEA),

the complex amplitude of the electric field is described by the Helmholtz equation

$$\frac{\partial \boldsymbol{A}}{\partial z} = \frac{i}{2k}\nabla_{\perp}^{2}\boldsymbol{A} + \frac{ik}{2n_r^2}\chi\boldsymbol{A}, \tag{6.6}$$

where, $\boldsymbol{A}$ and ∇ are complex field and Laplacian operator.

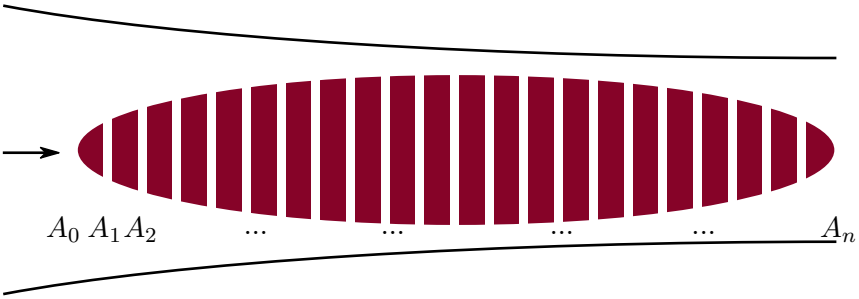

Figure 6.9.: Beam propagation through atomic cloud sections. A_i represents conplex field after i_{th} slice.

The Helmholtz equation is numerically solved by using so-called split-step method. The input field represented by $\boldsymbol{A}_0$ transforms into $\boldsymbol{A}_1$ after passing through the first slice of the cloud as a result of the Equation 6.6. The newly obtained field becomes input for the next atomic slice. The thickness of each of these slices is taken small enough such that the z-dependent higher order terms remain insignificant. The evolving light field after n slices gives an estimate of the complex electric field along the z-axis. The numerically efficient approach of solving the split-step method is described in the Appendix A.1 where the differential equation term is avoided by transforming the equation 6.6 in Fourier domain. With the fields obtained for different axial positions the complete intensity profile is reconstructed.

6.3.2. Propagation of light: Micro-lensing effect

The results are shown in Figure 6.10 for various laser detunings. In here, the beam profile for three different detunings are presented. Much like lensing effects, depending upon the detuning, the beam either focuses or defocuses. The effects are results of dispersive interaction which has a contrasting difference from the absorptive scattering. The dispersive processes are non-dispersive where no photons are scattered randomly whereas the absorption is a result of random scattering of light resulting in loss or heating. A remarkable point to notice is that for the negative detuning, the beam stays confined in the center of the atomic cloud in contrast with the positive detuning case. This adds more complexity in the final beam which comes out of the cloud due to the radial density variation of the atomic cloud. In particular, the negatively detuned beam encounters denser atomic cloud which results in a more absorptive response. On the other hand, the positively detuned beam avoids the cloud. This control has significant effect on the final absorption signal. Moreover, it adds another control knob

to enhance or diminish the light-matter coupling. The probe beam after the fiber has additional layer of complexity due to the mode selectivity properties of the fiber which filters out the Gaussian mode from the transmitting beam after the atomic cloud.

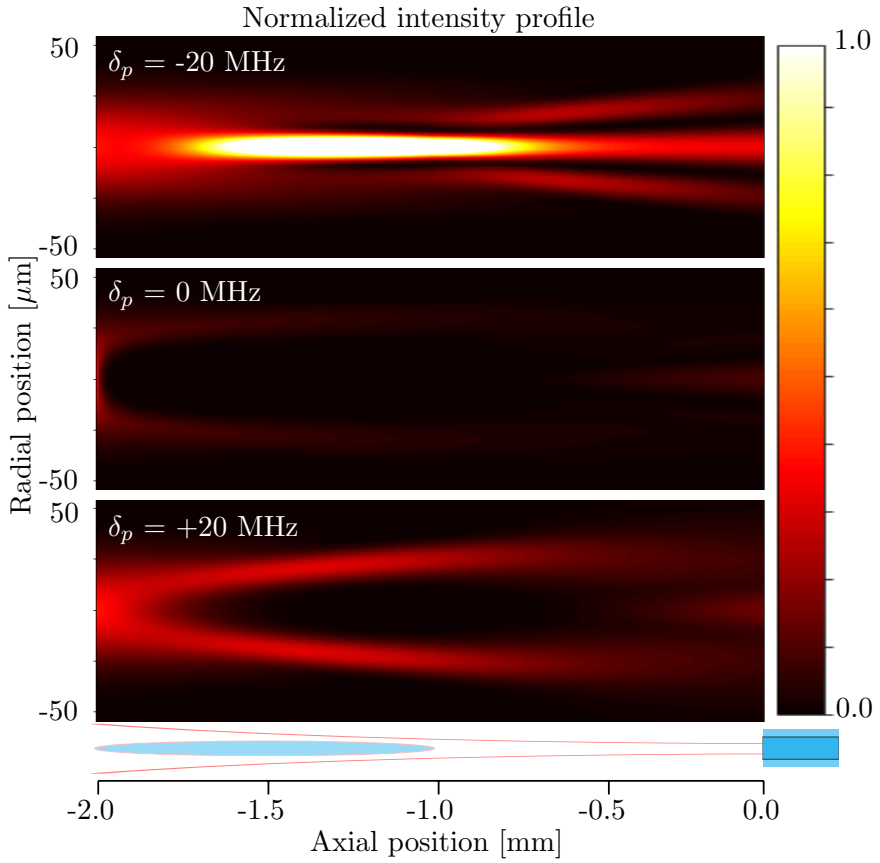

Figure 6.10.: Intensity profile for three different detunings. Probe beam enters from left side into the cloud shown in the lowest part. Different detunings show significantly altered beam profile in the way a lens works.

6.4. Micro-lensing induced lineshapes

Absorption imaging discussed in the Chapter 3 is only limited to detecting atoms when they are outside the fiber. As these atoms are transported inside the fiber, a new technique needs to be developed. For this purpose, the probe beam is overlapped on to the dipole trap beams which as a result passes through the atomic cloud. By scanning the probe detuning the atomic responses can be detected and hence the spectral information about the atoms. Interesting features about such interface, like optical depth can be estimated by this technique.
To obtain the exact transmission detected on the PMT, a complete information of the

beam as it passes through the cloud, is needed. First, a model is constructed for the trapped atoms outside the fiber to make the problem simple. Then the transmitting intensity profile for different detunings show interesting features. The probe beam is coupled into a single mode fiber after passing through the hollow-core (HC) fiber. The coupling efficiency into the HC fiber is above 90% and that for the single mode fiber is $> 70\%$. To include the finally detected beam into the single mode fiber, high coupling into HC fiber helps in simplifying the model.

6.4.1. Detection setup: Mode selection

Absorption causes the drop in the intensity of the propagating beam, while the dispersion is responsible for bending of light. In the case of this work, the cloud is cylindrically symmetric, acting like a thick lens. Hence the beam will not only encounter absorptive losses but will also undergo focusing or defocusing depending upon the detuning. For the typical experimental constraints, SVEA treatment is valid and appropriate.
The complete model for understanding the lineshape requires the inclusion of detection scheme. In this case, the first contribution comes from the propagating beam profile as certain part of it gets terminated due to its size exceeding the HC fiber wall. This is clearly visible in the the beam profile images and the model is included in the calculations discussed in Appendix A.2. In addition, the probe beam is coupled into a single mode fiber for the final detection. This fiber essentially selects the Gaussian mode of interest which is sensed on a PMT. The detected signal is calculated by integrating the field overlap between the fiber mode and the light field profile as:

$$I = \int_s \boldsymbol{A}(x, y)\mathcal{E}(x, y)dxdy, \tag{6.7}$$

where, s represents the area of integration which encompasses the HC fiber boundaries. The results can be perceived as effective change in coupling efficiency as a result of atom-induced-lensing. To estimate the transmission efficiency altered due to the atomic cloud, the overlap integral is normalized with a signals with atoms of homogeneous density as to isolate the shift due to lensing. In the Figure 6.11, the dispersive contribution is plotted along with the absorptive part. The absorptive part mainly remains symmetric about the $\delta_p = 0\,\text{MHz}$ in all three cases, whereas the dispersive contribution has significantly strong asymmetry. The combined signal, which is actually detected on a sensor, shows additional absorption along with an asymmetric shift. The reason for small bump near $-15\,\text{MHz}$ is the suppression in transmission at $-20\,\text{MHz}$ as a result of dispersion.

6.4.2. Transmission profile

The transmission signals for an expanding atomic cloud are shown in Figure 6.12(a). Here, the cloud is released from the trap and monitored continuously using a weak probe beam. Utilizing the thermal expansion governed by the temperature of the

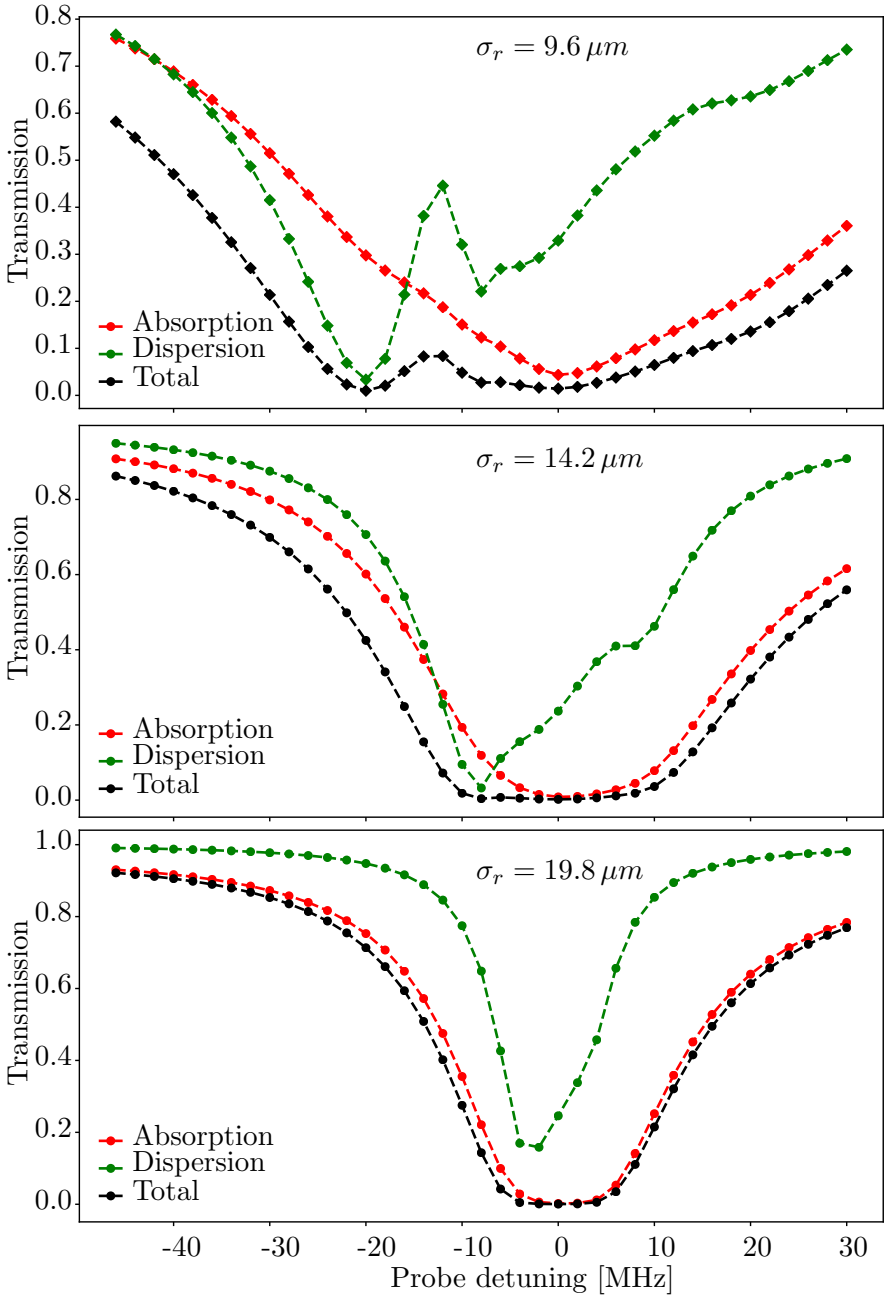

Figure 6.11.: Simulated lineshape for the different cloud sizes, σ_r.

cloud, the radial extend is estimated for different evolution time. The experiment is repeated for a set of varying detunings to obtain a complete spectral features. The overall features can very well be compared with the simulation shown in Figure 6.12(b). Moreover, the lack of non-trivial absorption can be seen near a detuning of $-15\,\mathrm{MHz}$ which is in good agreement with the simulation.

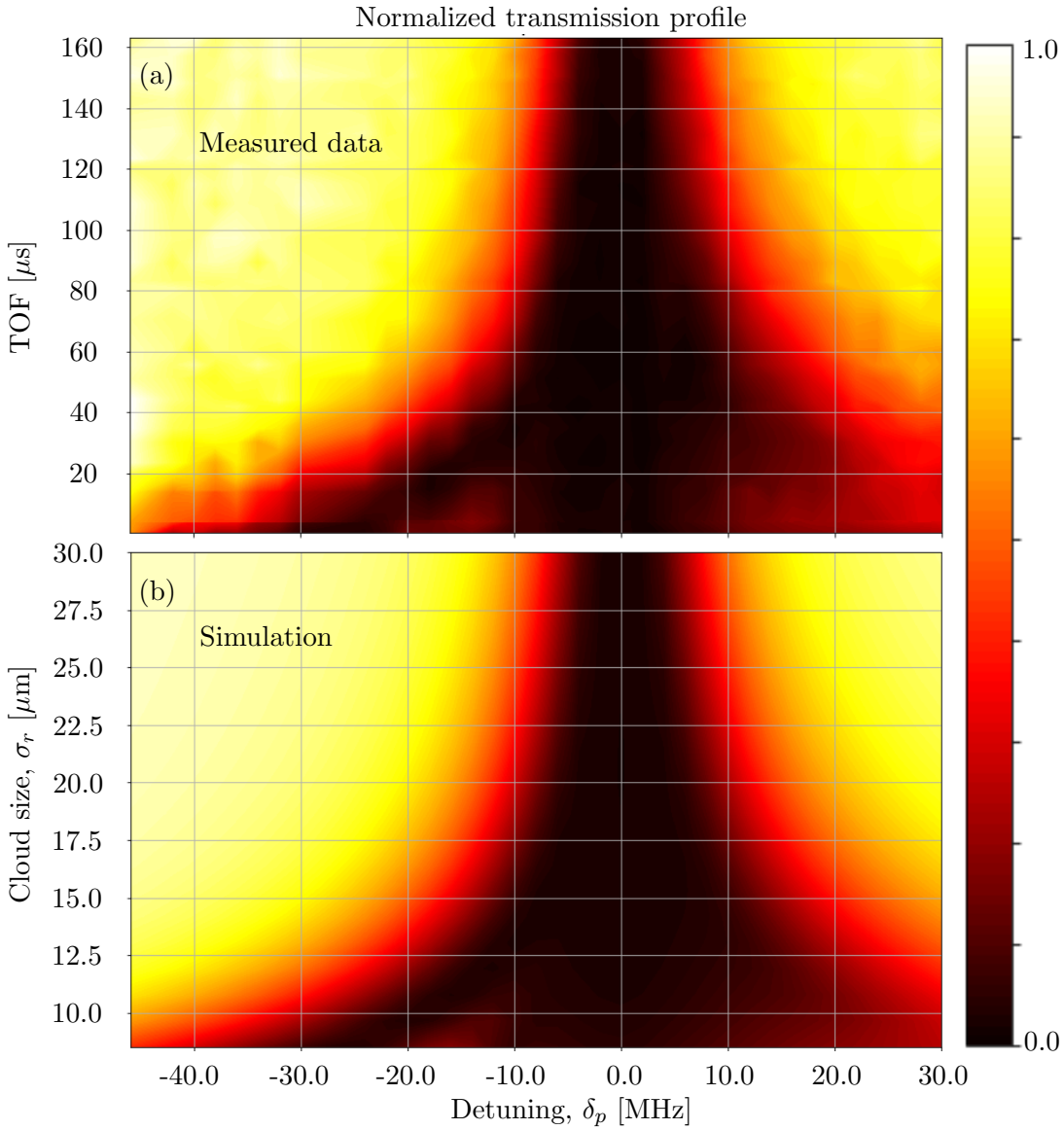

Figure 6.12.: Complete temporal and spectral transmission signal for (a) measured data and (b) simulated result.

Horizontal cuts of the Figure 6.12 are plotted in the Figure 6.13. In the Figure (a), the perfect agreement between the spectral lines are good indication of lensing induced line shapes. As for a large atomic size, the absorption profile resembles that obtained from a Lorentzian model which is symmetric in nature. For smaller cloud sizes the asymmetry increases which can not be explained by a simple Lorentzian model. Main point of focus here lies near detuning -15 MHz where an increase in transmission can be seen. The explanation for this behaviour is due to the lensing effects, which is

inhomogeneous, i.e. for one detuning it focuses the beam, while it defocues for the other. As a result, the beam is completely lost for a detuning near $-25\,\mathrm{MHz}$ leaving an apparent bump near $-15\,\mathrm{MHz}$. This appears because of the coupling into the single mode fiber.
The Figure 6.13(b) shows a simulation and data for OD measurements inside the fiber. The overall features satisfy the data, while the exact lineshapes lack from the goodness of the model as for the case where the atoms are inside the fiber, the complete model needs a term for guiding properties of the hollow-core fiber which is a work of separate research topic.

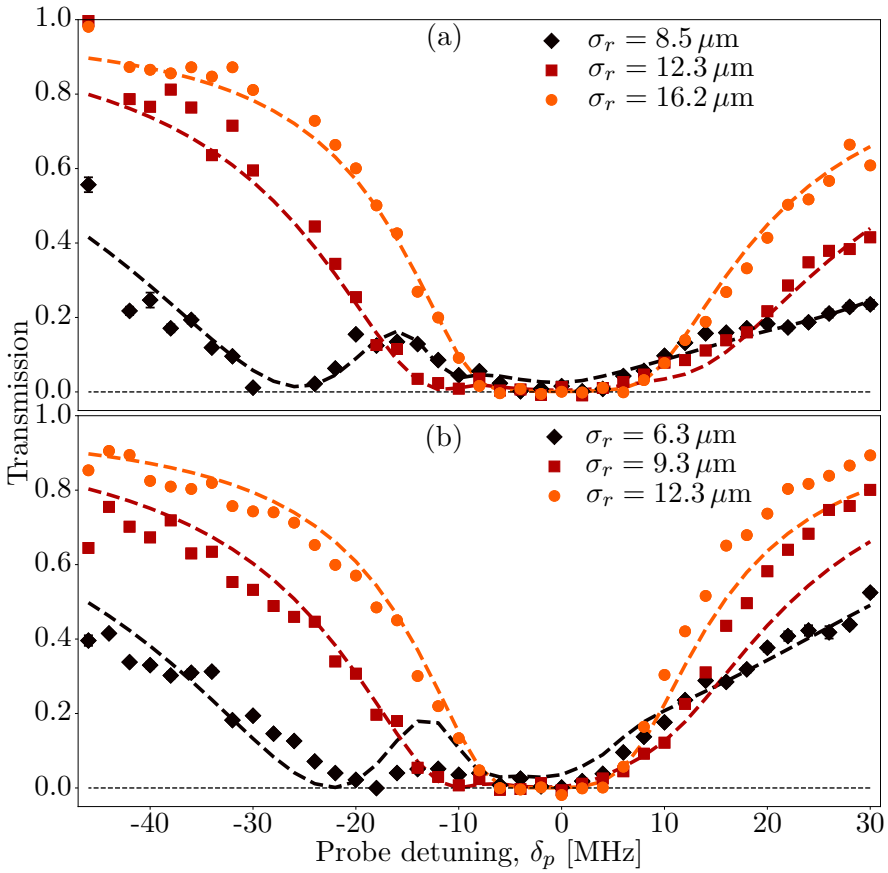

Figure 6.13.: Transmission signal for (a) outside and (b) inside the fiber. The dashed lines are fit model and markers are data taken from the experiment.

To compare the accuracy of the beam propagation model, a simple Lorentzian model, discussed in Chapter 2 is fitted to obtain the OD for the transmission data. As is evident that such model lacks the dispersive effects, hence the lineshapes deviate broadly for the tightly confined clouds. A comparison between the two models is plotted in Figure 6.14. A deviation above 50% in OD values are observed. For cloud sizes, comparable or larger than the probe beam size, the deviation is negligible.

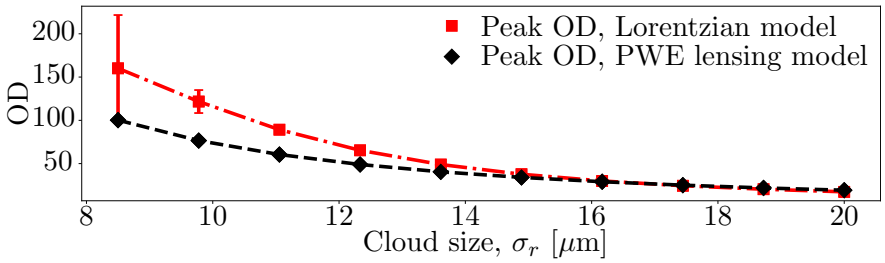

Figure 6.14.: Comparison of OD estimated from the PWE model and Lorentzian model

6.5. Rydberg EIT line shapes

With the results strongly depending upon dispersive nature of the atomic cloud, now the goal was to understand the line shapes for the Rydberg EIT processes, in particular near the two-photon resonances. As known for the EIT processes, the control beam modifies the optical properties of the atomic cloud. The results combined with the tightly confined atoms should again require a beam propagation model over standard EIT model discussed in Chapter 2. The control beam further modifies the susceptibility radially as the control intensity is overlapping with the probe beam

$$\chi_{EIT} = \frac{\sigma_0 \rho(x,y)}{k_0} \frac{i\gamma/2}{\gamma/2 - i\delta_p + \frac{\Omega_c^2(x,y)}{\Gamma/2 - i(\delta_p + \delta_c)}}, \tag{6.8}$$

where, $\rho(x,y)$ and $\Omega_c(x,y)$ are atomic density and control Rabi frequency. In this case, the modification in the optical susceptibility is primarily affected by two experimental constraints. The first case is induced by the geometrical configuration of atoms as present in the previous case with two level system. The second factor is considered due to the radially varying control Rabi frequency since the control beam propagates through the HC fiber. It is evident from the equation 6.8 that the local Rabi frequency, Ω_c has certain influence on the susceptibility, χ_{EIT}. To this end, the control beam profile is approximated to a Gaussian distribution as the influence of the atoms will have marginal effects,

$$I_c(r) = I_{c0} e^{-(\frac{r}{\sigma_r})^2}. \tag{6.9}$$

EIT lineshapes are studied for two distinct control detunings to explore the spectral features. The transmission signals are plotted in the Figure 6.15. Here, the particular interest is in the lineshapes near the EIT resonances. For the given cases, the lineshapes show significantly distinct asymmetry. The model for the EIT system is calculated by introducing the radially varying control Rabi frequency, $\Omega_c(r)$ in the equation 6.6 and followed by the numerical treatment. The numerical calculations confirm the observed EIT line features. This result is of significant importance for the reason that such asymmetries can arise from various factors such as ion production [97] or interactions [96]. While, the work done in this thesis claims that a geometrical reason can also modify the lineshapes.

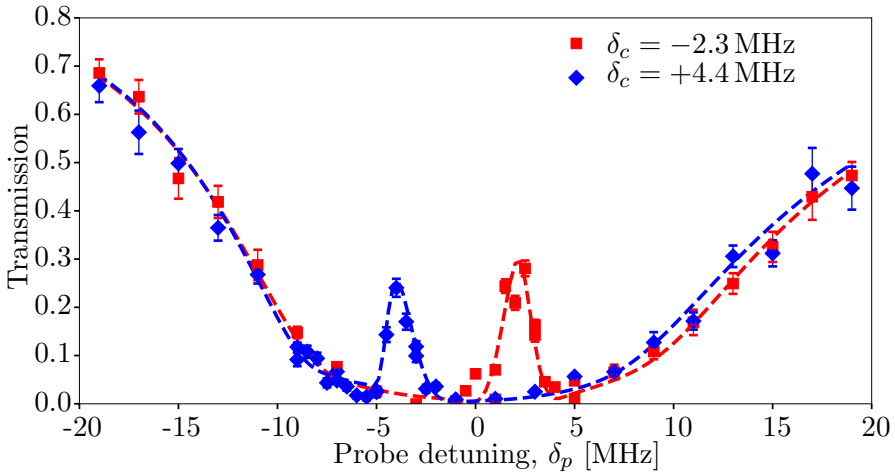

Figure 6.15.: Comparison of EIT line shapes using the PWE model for two different control detunings.

In conclusion, this chapter explores the significance of the dispersive effects as a result of the real part of the susceptibility. On the one hand, the atomic population is preserved as a result of non-destructive nature. On the other hand, the strong alteration in transmission lineshapes are obtained. These are some results of significant importance as the exact lineshape can have a range of underlying mechanism. In this case, the geometrical constraints contribute to similar alterations which is otherwise absent in such simple setup. In addition, the controlled environment can be utilized to manipulate the light propagation. As was apparent from the results that the beam can be made to stay focused in the core of the cloud or can avoid the cloud by just changing the laser detuning. The significance is in the fields of photon storage or spectroscopy. Rydberg EIT lineshapes have shown added feature as a result of control beam overlap which shows in excellent example of controlling the light not only by making it transparent but also by physically altering the path through the medium.

7. Conclusion and outlook

In the framework of the quantum technology and enabling applications, this project aims to develop techniques to create control and manipulation of light-matter interaction. In order to achieve this goal the atom-optics realization comprising of cold atoms is utilized. Finally, combining the features of Rydberg states this project establishes an attractive platform in the realm of quantum technology.
The tasks performed in this thesis can broadly be categorized in three main sections – the development of an extended light-matter overlap for strong interactions, the Rydberg excitation inside a confined geometry and the study of light propagation through a tightly confined atomic medium. As for creating strong light-matter interaction, the spatial overlap of the light and the atomic cloud is maintained for an extended length beyond the limitations imposed by the Rayleigh range in a free space. Such confinement is achieved by using a hollow-core fiber as an optical waveguide. Consequently, optical dipolar forces are exploited to trap and transport cold atoms in the same confining geometry giving an excellent overlap between light and matter. By combining a pair of such counter-propagating laser beams, an optical lattice is realized which can be set into motion to create a conveyor belt for cold atoms. The exact position is extracted by adjusting the time and the speed of the optical transport. By additionally overlapping a weak probe beam a light-matter interface is realized. Not limited to the Rayleigh range, such confinements offer a novel platform for arbitrarily extended interaction length. Observation of an OD above 200 with merely several thousands atoms is a good indicator of the strong light-matter interaction which results from the extended overlap of atomic ensemble with the propagating light field.
Considerable attention has been drawn towards creating a long-range interaction using the enhanced features of Rydberg atoms. The natural interest for this project is to utilize the atom-fiber interface for creating an extended atomic ensemble comprising of Rydberg states. Such quasi-one dimensional chain of Rydberg polaritons – a combined state of light and matter, have potential significance in the creation of the non-classical states of light and many-body photonic states. The inherent high sensitivity of the Rydberg atoms towards external fields is underlying driving force to achieve this goal. However, it is this high sensitivity that poses an experimental barrier to excite the atoms to high Rydberg states due to the stray field present near the fiber surface as confirmed by the shift observed in the EIT peaks limiting the excitation state to about $n = 35$. In attempt to overcome the barrier, a variety of fibers with different core and inner wall coatings have been studied. To conclude the outcomes, a coating of Rb vapour inside the fiber wall has the potentiality to nullify the electric fields which is demonstrated by the excitation of Rydberg states to the principal quantum number above $n = 60$. This can be understood due to the fact that the atoms shield

the fiber from inside in much like a Faraday cage. The results open up a broad scope for creating high Rydberg excitations which is the key requirement for the long range interactions.
With the promising applications, the atom-fiber interface lays a novel experimental platform for the creation of interacting system. However, due to the radial variation of the density of the atomic ensemble the propagation of the light through the medium requires a critical attention. A detailed understanding of light propagation in this configuration is made by a theoretical model by numerically solving the Helmholtz equation. A key point to consider here is that when light propagates through an extended medium, in particular, with the radial variation, the dispersive term can not be ignored. The phase delay caused by the local density of the atoms leads to the bending of light. In this case, due to the atomic density distribution in transverse direction, the light follows a path much like passing through a lens. Furthermore, by adjusting the laser detuning the sign of the lens can be altered. The theoretical model developed in this thesis and backed up by the experimental measurements demonstrate a way to control and manipulate the propagation of the laser beam through the atomic media. On one hand, for the red detuning of the laser, the probe beam travels through the denser part of the cloud. On the other hand, for the blue detuning, the beam avoids the cloud and hence absorptive losses are reduced. This way a precision control over light-matter overlap is achieved. This type of control additionally benefits from dispersive detection where on-resonant losses are reduced. The micro-lensing effect further alters the coupling of a probe beam through a single mode fiber which is generally used for detection and hence explains the asymmetric lineshapes that were observed. In the Rydberg EIT configuration, the control beam with Gaussian intensity distribution additionally modifies the response of the atomic medium and hence the observed lineshapes. The significance of the light propagation model is extremely useful for light-atom interface where, for instance, strong interaction is involved.

The research achievements presented in this thesis establish a platform for creating the strong light-matter interaction which is a key requirement for the development of the quantum applications. One of the major aspects of the atom guiding techniques is to provide a precision control and manipulation of cold-atoms which can be served as a pure quantum system. Beyond the creation of strong interaction, atoms guided in the hollow-core fibers have potential applications in the matter-wave interferometry. By continuous loading and guiding of cold atoms in the optical conveyor belt should allow for extremely long atom cloud confined in one dimension. The path of these atoms can be easily controlled by bending the HC fiber. For instance, by bending such a fiber in a closed loop can have potential applications in building a rotation sensor where the sensitivity scales with the loop area.
Excitation of higher Rydberg states is a key requirement for creating larger blockade radius and hence the light-atom coupling strength. HC fibers filled and coated with Rb atoms has unfolded a way to reach the excitation of higher Rydberg states which otherwise is highly suppressed due to the stray charges. These results inspire for

creating many-body photonic states, for example, by making a metallic coating on the inner wall of an HC fiber. Moreover, a realization of such interacting quantum system at room temperature can be an ideal achievement.
The light propagation model developed in this thesis leaves a remarkable understanding of the observed asymmetric transmission profile. The strong reduction in transmission at an off-resonant laser frequency facilitated by the dispersion of light in the atomic media is of significant importance. This result can prove helpful in non-demolition measurements based on dispersive detection while still maintaining a better signal strength. Furthermore, utilizing the EIT process, in particular involving Rydberg states, the intensity profile of the control laser can render the medium in ways which can alter the micro-lensing effects. Eventually the detected lines reflect the distortion in the lineshapes which has important consequences since such distortion can also arise from other mechanisms. Additionally, the intensity profile of the control laser can be tuned, for example, to counteract the bending of light in the Gaussian atomic medium.
As a final remark, the work done for this thesis has advanced a platform for quantum information, quantum computation and sensing aspects. The implementation of a controllable trap of cold atoms utilizing a hollow core fiber allows for a strong light matter interaction that is otherwise limited in free-space system. The thesis further discusses the way to excite Rydberg states near the confining surfaces which demonstrate a mean to realize strongly interacting many-body photonic system. A detailed study of the light beam propagation through the atoms in the trap enhances our understanding when dealing with such tightly confined media. The micro-lensing effect is further modified by a control light field associated with an EIT process, which not only alters the spectral feature of the weak probe beam, but it also controls the spatial profile.

A. Appendix 1

A.1. Split-step method

The Helmholtz equation is expressed in a general form as

$$\frac{\partial \boldsymbol{A}}{\partial z} = D\boldsymbol{A} + N\boldsymbol{A}, \tag{A.1}$$

where, the linear and non-linear terms are $D = \frac{i}{2k}\nabla_T^2$ and $N = \frac{ik}{2n_0^2}\chi$. Brute-force method faces difficulty due to the double derivative term. Fortunately, in the Fourier domain, the solution becomes much easier by completely avoiding the differentiation. For a small step size δz, the updated value for the complex electric field is

$$\boldsymbol{A}(z+\delta z) = exp^{-i(D+N)\delta z}(A)(z) \tag{A.2}$$

$$\approx exp^{-i(D)\delta z}\big[exp^{-i(N)\delta z}\boldsymbol{A}(z)\big]. \tag{A.3}$$

Now, to transform the equation into Fourier domain following substitutions are made

$$\partial/\partial x = \imath \mathbf{k}_x, \quad \partial/\partial y = \imath \mathbf{k}_y \tag{A.4}$$

$$\nabla_T^2 = \partial^2/\partial x^2 + \partial^2/\partial y^2 = -\mathbf{k}_x^2 - \mathbf{k}_y^2 \tag{A.5}$$

$$\mathbf{k}_x = 2\pi/\mathbf{x}, \quad \mathbf{k}_y = 2\pi/\mathbf{y} \tag{A.6}$$

The Helmholtz equation is represented in Fourier domain as

$$FT[\boldsymbol{A}(z+\delta z)] \approx FT[\exp^{-\imath D\delta z}] \ \ (FT[\exp^{-\imath N\delta z}\,\boldsymbol{A}(z)])$$

$$\boldsymbol{A}(z+\delta z) \approx FT^{-1}[\exp^{\imath \mathbf{k}^2\delta z}(FT[\exp^{-\imath N\delta z}\,\boldsymbol{A}(z)])]$$

with the following constrains

$$\nabla_T^2 = -\mathbf{k}_x^2 - \mathbf{k}_y^2 = -\mathbf{k}^2, \mathbf{k}_x = 2\pi/x, \mathbf{k}_y = 2\pi/y.$$

The key factor that lies here is transformation $FT[exp^{-iD\delta z}] = exp^{i\mathbf{k}^2\delta z}$.

A.2. Probing

The beam as it propagates through the atomic cloud approaches the HF fiber tip. At this stage the power that is detected is altered by two factors. First, depending upon the radial size of the beam, it can be masked on the Fiber front end and the second factor comes from the mode overlap of the beam with an unaltered beam profile.

The Figure‘A.1 depicts the masking effect as the detection is only made to the part of the beam which lies in the central zone. The remaining power after masking is calculated as

$$P = \int_A I(x, y) dx dy, \tag{A.7}$$

where A is the total allowed area for the beam to enter into the fiber.

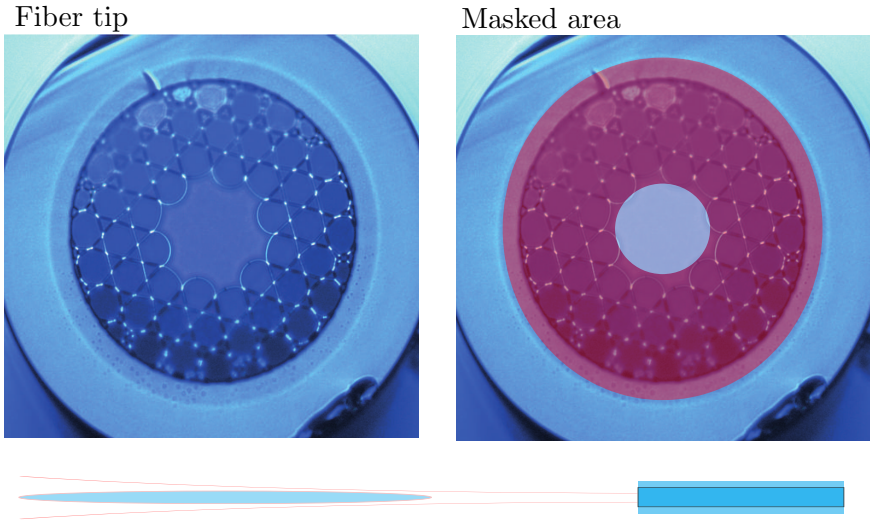

Figure A.1.: Masking model for the probe beam.

The mode overlap is calculated by the integration of the field profiles as follows

$$\eta = \frac{|\int \mathcal{E}_1^* \mathcal{E}_2 dA|^2}{\int |\mathcal{E}_1|^2 dA \int |\mathcal{E}_2|^2 dA}, \tag{A.8}$$

where, $\mathcal{E}_1$ and $\mathcal{E}_2$ are electric field profile for absence and presence of atomic media. It is evident, the term η modifies the coupling efficiency of the beam into the fiber. The total power detected on the PMT is simply calculated by taking a product of the equations A.7 and A.8.

$$P_{tot} = \eta P. \tag{A.9}$$

A.3. Python code for beam propagation

```
import matplotlib.pyplot as plt # Import library for direct plotting
    ↪ functions
import numpy as np # Import Numerical Python
from IPython.core.display import display, HTML #Import HTML for
    ↪ formatting output
```

```
#%% Gaussian beam specification
w0 = 20*1.e-6 # beam waist
x_um = np.linspace(-15*w0*1.e6,15*w0*1.e6,100) # radial distribution
    ↪ in um
x = x_um *1.e-6 # radial distribution in m
y_um = np.linspace(-15*w0*1.e6,15*w0*1.e6,100) # radial distribution
    ↪ in um
y = y_um *1.e-6 # radial distribution in m

E0 = 1
lam= 780*1.e-9
k0 = 2*np.pi/lam
n0 = 1
zr = w0**2*n0*np.pi/lam # rayleigh range
def gaussbeam(x,y,z):
        wz = w0*np.sqrt(1+((z-z0)/zr)**2)
        Rz = (z-z0)*(1+(zr/(z-z0))**2)
        E = E0 * w0/wz * np.exp(-(x**2+y**2)/(1*wz**2) + 1j*k0*(x**2+y
            ↪ **2)/(2*Rz) -1j*np.arctan((z-z0)/zr))# + 1j*k*(z-z0))# +
            ↪ 1j*(k*z-w*t))
        return E
z0 = 0

#%% create beam profile using gaussian approximation
xx1,yy1 = np.meshgrid(x,y)
z1 = np.linspace(-.0015,.0005,200) # position of the beam along the
    ↪ beam propagation axis
efld = []
for i in range(len(z1)):
        zz1 = z1[i]
        efld.append(gaussbeam(xx1,yy1,zz1))
        efld = np.array(efld)
efield = np.abs(efld[150])**2 # beam profile at the gaussian beam
    ↪ waist

#%% atomic cloud information for simulation
n_at = 120000 # number of trapped atoms
l_cl = 1*1.e-3 # length of atomic cloud
sigma_cl = 9*1.e-6 # radial distribution of the cloud
def at_den(sigma,N): # returns atomic density
        c = N/(2*np.pi*l_cl*sigma**2)
        rho = c*np.exp(-(xx1**2+yy1**2)/(2*sigma**2))
        return rho
rho = at_den(sigma_cl,n_at)
```

```
#%% calculate succeptibility, chi using the rho
lam = 780*1.e-9    # wavelength in nm (780 nm is resonant for Rb atoms
    ↪ )
sigma0 = 3*lam**2/(2*np.pi) # scattering cross section
Gamm = 2*np.pi*6.067*1.e6 # Natural linewidht of Rb atoms
k = 2*np.pi/lam   # wavenumber
det = np.linspace(-50,50,50)  # laser detuing in MHz
del_p = det*2*np.pi*1.e6 # detuing in Hz
def lineshape(detuning,rho): # returns succeptibility for two level
    ↪ system
        trm1 = -sigma0*rho/k
        trm2 = 2*detuning/Gamm -1j
        trm3 = 1 + 4*(detuning/Gamm)**2
        chi = trm1*trm2/trm3
        return chi
chi = []
for i in range(len(det)):
        chi.append(lineshape(del_p[i],rho))
chi = np.array(chi) # succeptibility for all detunings
nr = 1 + 1/2* np.real(chi) # real part of refractive index
ni = 1/2* np.imag(chi) # imaginary part of refractive index


#%% Set axes in the frequency basis (FT)
dx = x[1]-x[0]
dy = y[1]-y[0]
kx = np.fft.fftfreq(x.shape[0])*2*np.pi/dx
ky = np.fft.fftfreq(y.shape[0])*2*np.pi/dy
kkx,kky = np.meshgrid(kx,ky)

#%% FFT beam propagation integral
dz = z1[1] - z1[0] # step size along the beam propagation direction
in_fld = efld[0] # initial electric field at the input of the cloud
k0 = 2*np.pi/lam # wavenumber
beta = k0

def fftbpm(in_fld,chi,nr):
fftfld1 = np.fft.fft2(in_fld)
ifftfld = fftfld1*np.exp(-1j*(kkx**2+kky**2)*dz/(2*beta*nr))
out_fld = np.fft.ifft2(ifftfld)*np.exp(1j*k0/(2*nr**2)*chi*dz)
return out_fld

pos_cld = z1[0] # initial position of the cloud
```

```
def fftcal(in_fld,chi,nr):
phi_z = []
for i in range(len(z1)):
if i%(len(z1)/10) ==0:
print('.',end='')
if z1[i] < pos_cld: # before the cloud
out_fld = fftbpm(in_fld,0,1)
phi_z.append(in_fld)
in_fld = out_fld
if (z1[i] < pos_cld + l_cl) * (z1[i] >= pos_cld): # cloud region
out_fld = fftbpm(in_fld,chi,nr)
phi_z.append(in_fld)
in_fld = out_fld
if z1[i] >= pos_cld + l_cl: # after the cloud
out_fld = fftbpm(in_fld,0,1)
phi_z.append(in_fld)
in_fld = out_fld
phi_z = np.array(phi_z)
return phi_z

#%% generate list of x,y,z electric field profile for different
    ↪ detuning
xt = round(len(x)/2) # middle of the beam (along x or y axis)
psi1 = []
for i in range(len(det)):
        in_fld = efld[0]
        phph = fftcal(in_fld,chi[i],nr[i])
        psi1.append(phph.T[xt])
        print(i)
psi1 = np.array(psi1) # complex electric field of the beam
psi0 = fftcal(in_fld,0,1) # reference complex electric field (without
    ↪ atomic presence)
gaus_fld_ref = efld.T[xt] # reference gaussian propagation (somewhat
    ↪ analytical solution)
fft_fld_ref = psi0.T[xt] # reference fft model, numerical solution
fr_ind = 14
fft_fld_sig = psi1[fr_ind] # reference cloud signal, numerical
    ↪ solution
rad1,ax1 = np.meshgrid(x,z1) # meshgrid of radial and axial vectors
gaus_int_ref = np.abs(gaus_fld_ref)**2
fft_int_ref = np.abs(fft_fld_ref)**2
fft_int_sig = np.abs(fft_fld_sig)**2
```

```
#%% gaussian overlap integral to estimate the total transmission
def effcnc(sig1,sig0,x):
ef1 = sig1
ef0 = sig0
X = x
ov1 = (np.abs( np.sum(np.conjugate(ef1)*ef0*np.pi*np.abs(X)) ) )**2
ov2 = (np.sum( (np.abs(ef1))**2*np.pi*np.abs(X) ) )
ov3 = (np.sum( (np.abs(ef0))**2*np.pi*np.abs(X) ) )
efcnc = ov1/(ov2*ov3)
return efcnc

#% mode filtering and final detection
fib_core_rad = 26*1.e-6
msk_ind = np.arange(len(x))
cmpr1 = len(x)-(-fib_core_rad < x) * msk_ind[::-1]-1
cmpr2 = (fib_core_rad > x) * msk_ind
msk1 =np.min(cmpr1)
msk2 =np.max(cmpr2)
fr_ind = 10
fftfld = psi1[fr_ind]
reffld = psi0.T[xt]
def pwrout(fftfld):
        pwr = []
        efc = []
        for i in range(len(z1)):
                pw = np.abs(fftfld.T[i])**2 * np.abs(x)
                ef1 = fftfld.T[i]
                ef0 = reffld.T[i]
                if z1[i] < 0:
                        pwr.append(np.sum(pw))
                        efc.append(effcnc(ef1,ef0,x))
                else:
                        pwr.append(np.sum(pw[msk1:msk2]))
                        efc.append(effcnc(ef1[msk1:msk2],ef0[msk1:msk2],x
                            ↪ [msk1:msk2]))
                        pwr = np.array(pwr)
                        pwr = pwr/pwr[0]
                        efc = np.array(efc)
        return pwr, efc
pout = []
efcc = []
for i in range(len(det)):
        print('.', end='')
        fr_ind = i
```

```
        fftfld = psi1[fr_ind]
        pout.append(pwrout(fftfld)[0])
        efcc.append(pwrout(fftfld)[1])
pout = np.array(pout)
efcc = np.array(efcc)
#%% final transmission plot vs detuning
loc = 160
op = pout.T[loc]
ce = efcc.T[loc]
out_tot = op*ce
```

B. Appendix 2

B.1. Verilog code for FPGA sequence generator

The top level Verilog code for the FPGA pulse generator, Top.v:

```
module top(
        input CLK,
        input rst,
        output TXD,
        input RXD,
        output [7:0]LED);
wire [7:0] rx_data;
wire rcvd;
clk_new clk_new(
        .CLK_IN1(CLK), // IN
        .CLK_OUT1(CLK_OUT), // OUT
        .RESET(RESET), // IN
        .LOCKED(LOCKED)); // OUT
rx_ser serial_rx (
        .c_rx(CLK_OUT),
        .rxd(RXD),
        .flag(rcvd),
        .rx_1(rx_data));
reg reset;
reg we;
reg [11:0] addr;
reg [47:0] din;
wire [47:0] dout;
bram bram (
        .clka(CLK_OUT), // input clka
        .rsta(reset), // input rsta
        .wea(we), // input [0 : 0] wea
        .addra(addr), // input [11 : 0] addra
        .dina(din), // input [47 : 0] dina
        .douta(dout) // output [47 : 0] douta
        );
reg [7:0] data;
reg [39:0] tim;
```

```
reg trig;
reg [30:0] cntr;
reg x;
reg [15:0] seq_len;
reg [15:0] lnum;
reg [7:0] lstr;
reg [7:0] lend;
reg [7:0] llen;
reg [15:0] lcnt;
reg [15:0] lnum2;
reg [7:0] lstr2;
reg [7:0] lend2;
reg [7:0] llen2;
reg [15:0] lcnt2;
reg [7:0] step; // state machine cases
reg [7:0] ind;
always @ (posedge CLK_OUT)begin
if(rcvd == 1)
begin
        case(step)
        8'd0: begin
                if(rx_data == 8'b01110111) // press w button to enable
                    ↪ writing
                        begin
                        step <= 8'd1;  // go to next case step
                        ind <= 8'd47;
                        addr <= 0;
                        trig <= 0;
                        end
                else if(rx_data == 8'b01110010)
                        begin
                        addr <= 0;
                        trig <= 1;
                        step <= 8'd0;
                        end
                else begin
                        step <= 8'd0 ;
                        end
                end
        8'd1: begin
                seq_len[15:8] <= rx_data; // receive length byte2
                step <= 8'd2;
                end
        8'd2: begin
```

```
        seq_len[7:0] <= rx_data; // receive length byte1
        step <= 8'd3;
        end
8'd3: begin
        lstr[7:0] <= rx_data; // start of the loop byte
        step <= 8'd4;
        end
8'd4: begin
        lend[7:0] <= rx_data; // end of the loop byte
        step <= 8'd5;
        end
8'd5: begin
        llen <= lend - lstr; // end - start loop
        lnum[15:8] <= rx_data; // number of reps
        step <= 8'd6;
        end
8'd6: begin
        lnum[7:0] <= rx_data; // number of reps
        step <= 8'd7;
        end
8'd7: begin
        lstr2[7:0] <= rx_data; // start of the loop byte
        step <= 8'd8;
        end
8'd8: begin
        lend2[7:0] <= rx_data; // end of the loop byte
        step <= 8'd9;
        end
8'd9: begin
        llen2 <= lend2 - lstr2; // end - start loop
        lnum2[15:8] <= rx_data; // number of reps
        step <= 8'd10;
        end
8'd10: begin
        lnum2[7:0] <= rx_data; // number of reps
        step <= 8'd11;
        end
8'd11: begin
        if(we ==1)
                begin
                we <= 0;
                addr <= addr + 1;
                end
        din[ind -:8] <= rx_data;
```

```
                data <= din[47:40];
                ind <= ind - 8'd8;
                if(ind == 8'd7)
                        begin
                        we <= 1;
                        ind <= 8'd47;
                end
                if (addr == seq_len)
                        begin
                        step <= 8'd12;
                        we <= 0;
                        ind <= 8'd0;
                end
                end
        8'd12: begin
                step <= 8'd0;
                end
        endcase
end
if(rst == 0 && x == 0) // external trigger
        begin
        addr <= 0;
        trig <= 1;
        x <= 1; // latch
        end
if(rst == 1 ) // enables only single trigger event
        begin
        x <= 0;
        end
if(trig == 1 ) // readout data stored in bram
        begin
        data <= dout[47:40]; // dout stored to output
        cntr <= cntr + 1;
        tim <= dout[39:0];
        if(cntr >= tim)
                begin
                if(addr == lend) // first loop
                begin
                cntr <= 0;
                if(lcnt < lnum)begin
                addr <= addr - llen;
                lcnt <= lcnt + 1;
                end
        else begin
```

```
                addr <= addr + 1; // bram address increases
                cntr <= 0;
                lcnt <= 8'd0;
                end
        end
else if(addr == lend2) // second loop
        begin
        cntr <= 0;
        if(lcnt2 < lnum2)begin
        addr <= addr - llen2;
        lcnt2 <= lcnt2 + 1;
        end
else begin
        addr <= addr + 1; // bram address increases
        cntr <= 0;
        lcnt2 <= 8'd0;
        end
end
else begin
        addr <= addr + 1; // bram address increases
        cntr <= 0;
        end
end
if(addr == seq_len) // sets limit on the bram address
        begin
        trig <= 0;
        end
end
end
assign LED = data;
assign TXD = RXD;
endmodule
```

Verilog code for UART communication, rx.v:

```
module rx_ser
#( parameter clk_per_bit = 200)
(input c_rx,input rxd,output flag,output [7:0]rx_1);

reg r_rx;
reg rx;
reg [11:0]counter = 0;
reg i_flag;

reg [2:0] bit_index; // bit received
```

```
reg [7:0] rx_byte; // recieved serial byte data
reg [2:0] states = 0; // states for serial data bit

always @ (posedge c_rx)begin
       r_rx <= rxd;
       rx <= r_rx;
       end



always @(posedge c_rx) begin
       case(states)
       3'd0: begin // Triggers on rx low
       counter <= 0;
       bit_index <= 0;
       if(rx == 0) begin
              states <= 3'd1;
              end
       else begin
              states <= 3'd0;
              end
       end

       3'd1: begin
              if(counter == (clk_per_bit-1)/2) begin
              if(rx == 0) begin
                     counter <= 0;
                     states <= 3'd2;
                     end
              else begin
                     states <= 3'd0;
                     end
              end
       else
              begin
              counter <= counter + 1;
              states <= 3'd1;
              end
       end

       3'd2: begin // receives all the 8 bits
              if(counter == clk_per_bit-1) begin
                     counter <= 0;
                     rx_byte[bit_index] <= rx;
```

```
                if(bit_index < 7) begin
                        bit_index <= bit_index + 1;
                        states <= 3'd2;
                        end
                else begin
                        states <= 3'd3;
                        end
                end
                else
                        begin
                        counter <= counter +1;
                        states <= 3'd2;
                end
                end
        3'd3: begin // closing the state machine
                if(counter < clk_per_bit-1) begin
                        counter <= counter + 1;
                        states <= 3'd3;
                        end
                else begin
                        counter <= 0;
                        states <= 3'd4;
                        i_flag <= 1; // enalbles flag
                        end
                end
        3'd4: begin // resets the state machine
                states <= 3'd0;
                i_flag <= 0;
                end
        endcase
        end
assign rx_1 = rx_byte;
assign flag = i_flag;
endmodule
```

C. Appendix 3

C.1. HC fiber cleaning for UHV

The HC fiber is required to be UHV grade cleaned in order to maintain good vacuum level inside the chamber for laser cooling and trapping experiments. Although the fiber material is non-porous and has no issues if placed in UHV chamber however, due to the micro structures such as the fine holes inside the fibers can trap unwanted particles which can degas for enormously long times. These narrow capillaries can act as a differential pumping stage which significantly reduced the throughput rate of pumping out the particles from the inner walls. To circumvent the issues, the fiber is cleaned in a separate pumping system where severely stronger measures can be taken without any risk. The cleaning setup is shown in the Figure C.1 where fibers are placed inside the narrow tube. One of the main openings is attached to a valve which can be opened to flush the system with N_2 gas. The idea is to first pump down the system to pressures below 10^{-10} bar of the main chamber. At this pressure, the fibers start to release some particles, however the rate is extremely low due to the reduced pumping rates. To speed up the process the section where fiber is placed is heated to temperatures above 180^0C which increases the pressure inside the fiber hence the throughput speed goes high. Now, at this stage the pumps are turned off and simultaneously, dry N_2 is flushed into the chamber. The N_2 would take the empty space inside the HC fiber. Now, the pumping process with bakeout is repeated. The argument is that the N_2 molecules would eventually replace all the unwanted particles inside the fiber. This has two aspects: first, pumping out N_2 is easier and should not affect the main experimental chamber and the second reasoning is to deal with the challenge in transporting the cleaned fiber into the main UHV chamber. Since the fiber would be filled with N_2 at ambient pressure, the inflow of unwanted particles would be limited.

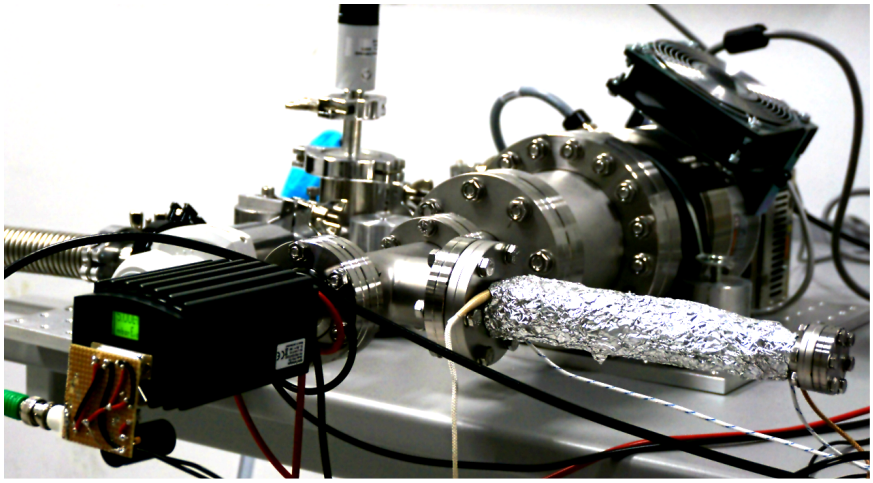

Figure C.1.: Fiber cleaning pumping system.

List of Figures

List of Tables

Bibliography

[1] MOGlabs .
Mog performance.
May 2014.

[2] D. A. Anderson, S. A. Miller, G. Raithel, J. A. Gordon, M. L. Butler, and C. L. Holloway.
Optical measurements of strong microwave fields with rydberg atoms in a vapor cell.
Phys. Rev. Applied, 5:034003, Mar 2016.

[3] M. H. Anderson, J. R. Ensher, M. R. Matthews, C. E. Wieman, and E. A. Cornell.
Observation of bose-einstein condensation in a dilute atomic vapor.
Science, 269(5221):198–201, 1995.

[4] E. Arimondo.
V coherent population trapping in laser spectroscopy.
volume 35 of *Progress in Optics*, pages 257 – 354. Elsevier, 1996.

[5] C. Ates, T. Pohl, T. Pattard, and J. M. Rost.
Many-body theory of excitation dynamics in an ultracold rydberg gas.
Phys. Rev. A, 76:013413, Jul 2007.

[6] S. H. Autler and C. H. Townes.
Stark effect in rapidly varying fields.
Phys. Rev., 100:703–722, Oct 1955.

[7] M. V. Balabas, T. Karaulanov, M. P. Ledbetter, and D. Budker.
Polarized alkali-metal vapor with minute-long transverse spin-relaxation time.
Phys. Rev. Lett., 105:070801, Aug 2010.

[8] J B Balewski, A T Krupp, A Gaj, S Hofferberth, R Löw, and T Pfau.
Rydberg dressing: understanding of collective many-body effects and implications for experiments.
New Journal of Physics, 16(6):063012, jun 2014.

[9] Simon Baur, Daniel Tiarks, Gerhard Rempe, and Stephan Dürr.
Single-photon switch based on rydberg blockade.
Phys. Rev. Lett., 112:073901, Feb 2014.

[10] Charles H. Bennett and Gilles Brassard.
Quantum cryptography: Public key distribution and coin tossing.
Theoretical Computer Science, 560:7 – 11, 2014.

Theoretical Aspects of Quantum Cryptography – celebrating 30 years of BB84.

[11] Eric D. Black.
An introduction to pound–drever–hall laser frequency stabilization.
American Journal of Physics, 69(1):79–87, 2001.

[12] Frank Blatt, Thomas Halfmann, and Thorsten Peters.
One-dimensional ultracold medium of extreme optical depth.
Opt. Lett., 39(3):446–449, Feb 2014.

[13] Immanuel Bloch, Jean Dalibard, and Wilhelm Zwerger.
Many-body physics with ultracold gases.
Rev. Mod. Phys., 80:885–964, Jul 2008.

[14] Niels Bohr.
On the constitution of atoms and molecules, part i.
Philosophical Magazine, 26:1–25, 1913.

[15] T D Bradley, E Ilinova, J J McFerran, J Jouin, B Debord, M Alharbi, P Thomas, F Gérôme, and F Benabid.
Ground-state atomic polarization relaxation-time measurement of rb filled hypocycloidal core-shaped kagome HC-PCF.
Journal of Physics B: Atomic, Molecular and Optical Physics, 49(18):185401, sep 2016.

[16] T. D. Bradley, J. J. McFerran, E. Ilinova, J. Jouin, P. Thomas, and F. Benabid.
Atomic polarization relaxation time measurement of rb filled hypocycloidal core shape kagome hc-pcf.
In *CLEO: 2013*, pages 1–2, June 2013.

[17] S. Braun, J. P. Ronzheimer, M. Schreiber, S. S. Hodgman, T. Rom, I. Bloch, and U. Schneider.
Negative absolute temperature for motional degrees of freedom.
Science, 339(6115):52–55, 2013.

[18] J. Dalibard and C. Cohen-Tannoudji.
Laser cooling below the doppler limit by polarization gradients: simple theoretical models.
J. Opt. Soc. Am. B, 6(11):2023–2045, Nov 1989.

[19] K. B. Davis, M. O. Mewes, M. R. Andrews, N. J. van Druten, D. S. Durfee, D. M. Kurn, and W. Ketterle.
Bose-einstein condensation in a gas of sodium atoms.
Phys. Rev. Lett., 75:3969–3973, Nov 1995.

[20] D. Davtyan, S. Machluf, M. L. Soudijn, J. B. Naber, N. J. van Druten, H. B. van Linden van den Heuvell, and R. J. C. Spreeuw.
Controlling stray electric fields on an atom chip for experiments on rydberg atoms.
Phys. Rev. A, 97:023418, Feb 2018.

[21] B. Debord, A. Amsanpally, M. Chafer, A. Baz, M. Maurel, J. M. Blondy, E. Hugonnot, F. Scol, L. Vincetti, F. Gérôme, and F. Benabid.
Ultralow transmission loss in inhibited-coupling guiding hollow fibers.
Optica, 4(2):209–217, Feb 2017.

[22] Savas Dimopoulos, Peter W. Graham, Jason M. Hogan, Mark A. Kasevich, and Surjeet Rajendran.
Gravitational wave detection with atom interferometry.
Physics Letters B, 678(1):37 – 40, 2009.

[23] Artur K. Ekert.
Quantum cryptography based on bell's theorem.
Phys. Rev. Lett., 67:661–663, Aug 1991.

[24] L. ESSEN and J. V. L. PARRY.
An atomic standard of frequency and time interval: A cæsium resonator.
Nature, 176(4476):280–282, 1955.

[25] Richard P. Feynman, Robert B. Leighton, and Matthew Sands.
The Feynman lectures on physics Vol. 3, Vol. 3,.
Addison-Wesley, Reading, Mass., 1965.

[26] O Firstenberg, C S Adams, and S Hofferberth.
Nonlinear quantum optics mediated by rydberg interactions.
Journal of Physics B: Atomic, Molecular and Optical Physics, 49(15):152003, 2016.

[27] Ofer Firstenberg, Thibault Peyronel, Qi-Yu Liang, Alexey V. Gorshkov, Mikhail D. Lukin, and Vladan Vuletic.
Attractive photons in a quantum nonlinear medium.
Nature, 502:71–75, Sep 2013.

[28] M. Fleischhauer and M. D. Lukin.
Dark-state polaritons in electromagnetically induced transparency.
Phys. Rev. Lett., 84:5094–5097, May 2000.

[29] Michael Fleischhauer, Atac Imamoglu, and Jonathan P. Marangos.
Electromagnetically induced transparency: Optics in coherent media.
Rev. Mod. Phys., 77:633–673, Jul 2005.

[30] P. A. Franken, A. E. Hill, C. W. Peters, and G. Weinreich.
Generation of optical harmonics.
Phys. Rev. Lett., 7:118–119, Aug 1961.

[31] M. T. Frey, X. Ling, B. G. Lindsay, K. A. Smith, and F. B. Dunning.
Use of the stark effect to minimize residual electric fields in an experimental volume.
Review of Scientific Instruments, 64(12):3649–3650, 1993.

[32] Takeshi Fukuhara, Sebastian Hild, Johannes Zeiher, Peter Schauß, Immanuel Bloch, Manuel Endres, and Christian Gross.

Spatially resolved detection of a spin-entanglement wave in a bose-hubbard chain.
Phys. Rev. Lett., 115:035302, Jul 2015.

[33] Thomas F. Gallagher.
Rydberg Atoms.
Cambridge Monographs on Atomic, Molecular and Chemical Physics. Cambridge University Press, 1994.

[34] E. J. Galvez, J. R. Lewis, B. Chaudhuri, J. J. Rasweiler, H. Latvakoski, F. De Zela, E. Massoni, and H. Castillo.
Multistep transitions between rydberg states of na induced by blackbody radiation.
Phys. Rev. A, 51:4010–4017, May 1995.

[35] U. Gaubatz, P. Rudecki, S. Schiemann, and K. Bergmann.
Population transfer between molecular vibrational levels by stimulated raman scattering with partially overlapping laser fields. a new concept and experimental results.
The Journal of Chemical Physics, 92(9):5363–5376, 1990.

[36] H. Gorniaczyk, C. Tresp, J. Schmidt, H. Fedder, and S. Hofferberth.
Single-photon transistor mediated by interstate rydberg interactions.
Phys. Rev. Lett., 113:053601, Jul 2014.

[37] Alexey V. Gorshkov, Johannes Otterbach, Michael Fleischhauer, Thomas Pohl, and Mikhail D. Lukin.
Photon-photon interactions via rydberg blockade.
Phys. Rev. Lett., 107:133602, Sep 2011.

[38] P Grangier, G Roger, and A Aspect.
Experimental evidence for a photon anticorrelation effect on a beam splitter: A new light on single-photon interferences.
Europhysics Letters (EPL), 1(4):173–179, feb 1986.

[39] Markus Greiner, Olaf Mandel, Tilman Esslinger, Theodor W. Hänsch, and Immanuel Bloch.
Quantum phase transition from a superfluid to a mott insulator in a gas of ultracold atoms.
Nature, 415(6867):39–44, 2002.

[40] Rudolf Grimm, Matthias Weidemüller, and Yurii B. Ovchinnikov.
Optical dipole traps for neutral atoms.
volume 42 of *Advances In Atomic, Molecular, and Optical Physics*, pages 95 – 170. Academic Press, 2000.

[41] Lov K. Grover.
A fast quantum mechanical algorithm for database search.
In *ANNUAL ACM SYMPOSIUM ON THEORY OF COMPUTING*, pages 212–219. ACM, 1996.

[42] Vera Guarrera, Dominik Muth, Ralf Labouvie, Andreas Vogler, Giovanni Barontini, Michael Fleischhauer, and Herwig Ott.
Spatiotemporal fermionization of strongly interacting one-dimensional bosons.
Phys. Rev. A, 86:021601, Aug 2012.

[43] Bastian Hacker, Stephan Welte, Gerhard Rempe, and Stephan Ritter.
Quantum coding.
Nature, 536, July 2016.

[44] S Haroche, Michel Brune, and J Raimond.
Experiments with single atoms in a cavity: Entanglement, schrodinger's cats and decoherence.
Proceedings of The Royal Society A: Mathematical, Physical and Engineering Sciences, 355:2367–2380, 01 1997.

[45] Lene Vestergaard Hau, S. E. Harris, Zachary Dutton, and Cyrus H. Behroozi.
Light speed reduction to 17 metres per second in an ultracold atomic gas.
Nature, 397(6720):594–598, 1999.

[46] D. L. Huber.
Resonant scattering of monochromatic light in gases.
Phys. Rev., 178:93–102, Feb 1969.

[47] N. Šibalić, J.D. Pritchard, C.S. Adams, and K.J. Weatherill.
Arc: An open-source library for calculating properties of alkali rydberg atoms.
Computer Physics Communications, 220:319 – 331, 2017.

[48] Sindhu Jammi, Tadas Pyragius, Mark G. Bason, Hans Marin Florez, and Thomas Fernholz.
Dispersive detection of radio-frequency-dressed states.
Phys. Rev. A, 97:043416, Apr 2018.

[49] E. T. Jaynes and F. W. Cummings.
Comparison of quantum and semiclassical radiation theories with application to the beam maser.
Proceedings of the IEEE, 51(1):89–109, Jan 1963.

[50] Mark Kasevich and Steven Chu.
Atomic interferometry using stimulated raman transitions.
Phys. Rev. Lett., 67:181–184, Jul 1991.

[51] H J Kimble.
The quantum internet.
Nature, 453:1023, jun 2008.

[52] H. J. Kimble, M. Dagenais, and L. Mandel.
Photon antibunching in resonance fluorescence.
Phys. Rev. Lett., 39:691–695, Sep 1977.

[53] Daniel Kleppner, H. Mark Goldenberg, and Norman F. Ramsey.
Theory of the hydrogen maser.
Phys. Rev., 126:603–615, Apr 1962.

[54] H. Kogelnik and T. Li.
Laser beams and resonators.
Appl. Opt., 5(10):1550–1567, Oct 1966.

[55] C. Korn.
Stabilitätsuntersuchungen eines zweistrahl-laserinterferometers, Bachelor's thesis, 2016.

[56] Jasper S. Krauser, Jannes Heinze, Nick Fläschner, Sören Götze, Ole Jürgensen, Dirk-Sören Lühmann, Christoph Becker, and Klaus Sengstock.
Coherent multi-flavour spin dynamics in a fermionic quantum gas.
Nature Physics, 8:813–818, Sep 2012.
Article.

[57] H. Kübler, D. Booth, J. Sedlacek, P. Zabawa, and J. P. Shaffer.
Exploiting the coupling between a rydberg atom and a surface phonon polariton for single-photon subtraction.
Phys. Rev. A, 88:043810, Oct 2013.

[58] Santosh Kumar, Harald Kübler, Jiteng Sheng, and James P. Shaffer.
Atom-based sensing of weak radio frequency electric fields using homodyne readout.
Scientific Reports, 7, Feb 2017.

[59] M. Langbecker.
A highly controllable cold rydberg atom hollow-core fiber interface, PhD thesis, 2020.

[60] Maria Langbecker, Mohammad Noaman, Niels Kjærgaard, Fetah Benabid, and Patrick Windpassinger.
Rydberg excitation of cold atoms inside a hollow-core fiber.
Phys. Rev. A, 96:041402, Oct 2017.

[61] Maria Langbecker, Ronja Wirtz, Fabian Knoch, Mohammad Noaman, Thomas Speck, and Patrick Windpassinger.
Highly controlled optical transport of cold atoms into a hollow-core fiber.
arXiv, 1805.06333, 2018.

[62] M. D. Lukin, M. Fleischhauer, R. Cote, L. M. Duan, D. Jaksch, J. I. Cirac, and P. Zoller.
Dipole blockade and quantum information processing in mesoscopic atomic ensembles.
Phys. Rev. Lett., 87:037901, Jun 2001.

[63] Marco Mattioli, Marcello Dalmonte, Wolfgang Lechner, and Guido Pupillo.
Cluster luttinger liquids of rydberg-dressed atoms in optical lattices.
Phys. Rev. Lett., 111:165302, Oct 2013.

[64] D. Maxwell, D. J. Szwer, D. Paredes-Barato, H. Busche, J. D. Pritchard, A. Gauguet, K. J. Weatherill, M. P. A. Jones, and C. S. Adams.
Storage and control of optical photons using rydberg polaritons.

Phys. Rev. Lett., 110:103001, Mar 2013.

[65] Michael Mayle, Bernd Hezel, Igor Lesanovsky, and Peter Schmelcher.
One-dimensional rydberg gas in a magnetoelectric trap.
Phys. Rev. Lett., 99:113004, Sep 2007.

[66] W. F. McGrew, X. Zhang, R. J. Fasano, S. A. Schäffer, K. Beloy, D. Nicolodi, R. C. Brown, N. Hinkley, G. Milani, M. Schioppo, T. H. Yoon, and A. D. Ludlow.
Atomic clock performance enabling geodesy below the centimetre level.
Nature, 564(7734):87–90, 2018.

[67] Harold J. Metcalf and Peter van der Straten.
Magnetic Trapping of Neutral Atoms, pages 137–148.
Springer New York, New York, NY, 1999.

[68] A. K. Mohapatra, T. R. Jackson, and C. S. Adams.
Coherent optical detection of highly excited rydberg states using electromagnetically induced transparency.
Phys. Rev. Lett., 98:113003, Mar 2007.

[69] Mohammad Noaman, Maria Langbecker, and Patrick Windpassinger.
Micro-lensing-induced line shapes in a single-mode cold-atom–hollow-core-fiber interface.
Opt. Lett., 43(16):3925–3928, Aug 2018.

[70] Shoichi Okaba, Tetsushi Takano, Fetah Benabid, Tom Bradley, Luca Vincetti, Zakhar Maizelis, Valery Yampol'Skii, Franco Nori, and Hidetoshi Katori.
Lamb-Dicke spectroscopy of atoms in a hollow-core photonic crystal fibre.
Nature Communications, 5(May):1–9, 2014.

[71] William D. Phillips.
Nobel lecture: Laser cooling and trapping of neutral atoms.
Rev. Mod. Phys., 70:721–741, Jul 1998.

[72] William D. Phillips, John V. Prodan, and Harold J. Metcalf.
Laser cooling and electromagnetic trapping of neutral atoms.
J. Opt. Soc. Am. B, 2(11):1751–1767, Nov 1985.

[73] D.E. Pritchard, A.D. Cronin, S. Gupta, and D.A. Kokorowski.
Atom optics: Old ideas, current technology, and new results.
Annalen der Physik, 10(1-2):35–54, 2001.

[74] J. D. Pritchard, D. Maxwell, A. Gauguet, K. J. Weatherill, M. P. A. Jones, and C. S. Adams.
Cooperative atom-light interaction in a blockaded rydberg ensemble.
Phys. Rev. Lett., 105:193603, Nov 2010.

[75] Xiaodong Qi, Ben Q. Baragiola, Poul S. Jessen, and Ivan H. Deutsch.
Dispersive response of atoms trapped near the surface of an optical nanofiber with applications to quantum nondemolition measurement and spin squeezing.

Phys. Rev. A, 93:023817, Feb 2016.

[76] E. L. Raab, M. Prentiss, Alex Cable, Steven Chu, and D. E. Pritchard.
Trapping of neutral sodium atoms with radiation pressure.
Phys. Rev. Lett., 59:2631–2634, Dec 1987.

[77] J. M. Raimond, M. Brune, and S. Haroche.
Manipulating quantum entanglement with atoms and photons in a cavity.
Rev. Mod. Phys., 73:565–582, Aug 2001.

[78] Sylvain Ravets, Henning Labuhn, Daniel Barredo, Lucas Béguin, Thierry Lahaye, and Antoine Browaeys.
Coherent dipole-dipole coupling between two single rydberg atoms at an electrically-tuned förster resonance.
Nature Physics, 10:914–917, Oct 2014.

[79] Fabian Ripka, Harald Kübler, Robert Löw, and Tilman Pfau.
A room-temperature single-photon source based on strongly interacting rydberg atoms.
Science, 362(6413):446–449, 2018.

[80] M. Saffman and T. G. Walker.
Analysis of a quantum logic device based on dipole-dipole interactions of optically trapped rydberg atoms.
Phys. Rev. A, 72:022347, Aug 2005.

[81] Michael Schreiber, Sean S. Hodgman, Pranjal Bordia, Henrik P. Lüschen, Mark H. Fischer, Ronen Vosk, Ehud Altman, Ulrich Schneider, and Immanuel Bloch.
Observation of many-body localization of interacting fermions in a quasirandom optical lattice.
Science, 349(6250):842–845, 2015.

[82] Benjamin Schumacher.
Quantum coding.
Phys. Rev. A, 51:2738–2747, Apr 1995.

[83] M. Selch.
Rubidium spectroscopy inside hollow core fibers, Bachelor's thesis, 2016.

[84] Peter W. Shor.
Polynomial-time algorithms for prime factorization and discrete logarithms on a quantum computer.
SIAM J. Comput., 26(5):1484–1509, October 1997.

[85] Aaron D. Slepkov, Amar R. Bhagwat, Vivek Venkataraman, Pablo Londero, and Alexander L. Gaeta.
Spectroscopy of rb atoms in hollow-core fibers.
Phys. Rev. A, 81:053825, May 2010.

[86] Parvis Soltan-Panahi, Dirk-Sören Lühmann, Julian Struck, Patrick Windpassinger, and Klaus Sengstock.

Quantum phase transition to unconventional multi-orbital superfluidity in optical lattices.
Nature Physics, 8:71–75, Oct 2011.

[87] J. Struck, C. Ölschläger, R. Le Targat, P. Soltan-Panahi, A. Eckardt, M. Lewenstein, P. Windpassinger, and K. Sengstock.
Quantum simulation of frustrated classical magnetism in triangular optical lattices.
Science, 333(6045):996–999, 2011.

[88] J. Struck, M. Weinberg, C. Ölschläger, P. Windpassinger, J. Simonet, K. Sengstock, R. Höppner, P. Hauke, A. Eckardt, M. Lewenstein, and L. Mathey.
Engineering ising-xy spin-models in a triangular lattice using tunable artificial gauge fields.
Nature Physics, 9:738–743, Sep 2013.
Article.

[89] F. Stuhtmann.
Programmierung und implementierung einer flexiblen aom-ansteuerung, Bachelor's thesis, 2016.

[90] Daniel Tiarks, Steffen Schmidt, Gerhard Rempe, and Stephan Dürr.
Optical π phase shift created with a single-photon pulse.
Science Advances, 2(4), 2016.

[91] Daniel Tiarks, Steffen Schmidt-Eberle, Thomas Stolz, Gerhard Rempe, and Stephan Dürr.
A photon-photon quantum gate based on rydberg interactions.
Nature Physics, 15(2):124–126, 2019.

[92] C. Tresp, C. Zimmer, I. Mirgorodskiy, H. Gorniaczyk, A. Paris-Mandoki, and S. Hofferberth.
Single-photon absorber based on strongly interacting rydberg atoms.
Phys. Rev. Lett., 117:223001, Nov 2016.

[93] Marco Triches, Mattia Michieletto, Jan Hald, Jens K. Lyngsø, Jesper Lægsgaard, and Ole Bang.
Optical frequency standard using acetylene-filled hollow-core photonic crystal fibers.
Opt. Express, 23(9):11227–11241, May 2015.

[94] C. Voss.
Eit-spektroskopie von rydbergzuständen an rubidium, Bachelor's thesis, 2015.

[95] C. Voss.
Rydbergspektroskopie in hohlkernfasern, Master's thesis, 2017.

[96] K J Weatherill, J D Pritchard, R P Abel, M G Bason, A K Mohapatra, and C S Adams.
Electromagnetically induced transparency of an interacting cold rydberg ensemble.

Journal of Physics B: Atomic, Molecular and Optical Physics, 41(20):201002, 2008.

[97] Daniel Weller, Alban Urvoy, Andy Rico, Robert Löw, and Harald Kübler.
Charge-induced optical bistability in thermal rydberg vapor.
Phys. Rev. A, 94:063820, Dec 2016.

[98] R. Wirtz.
Optischer transport von kalten atomen in eine hohlkernfaser, Master's thesis, 2018.

[99] Peter Wolf, Luc Blanchet, Christian J. Bordé, Serge Reynaud, Christophe Salomon, and Claude Cohen-Tannoudji.
Atom gravimeters and gravitational redshift.
Nature, 467:E1, Sep 2010.

[100] W. K. Wootters and W. H. Zurek.
A single quantum cannot be cloned.
Nature, 299, 1982.

[101] Xilinx.
Spartan-6 family overview.
(DS160), October 25, 2011.

[102] Mingjie Xin, Wui Seng Leong, Zilong Chen, and Shau-Yu Lan.
An atom interferometer inside a hollow-core photonic crystal fiber.
Science Advances, 4(1), 2018.

[103] T. Yoon, J. Flannery, and M. Bajcsy.
Strong optical nonlinearities in hollow-core photonic-crystal fibers loaded with ensembles of cold atoms.
In *2017 Conference on Lasers and Electro-Optics Pacific Rim (CLEO-PR)*, pages 1–2, July 2017.